

Aus dem
Institut für Schlaganfall- und Demenzforschung (ISD)
Klinikum der Ludwig-Maximilians-Universität München



Systemic Inflammation Post Stroke Leads to Secondary Organ Dysfunction

Dissertation
zum Erwerb des Doctor of Philosophy (Ph.D.)
an der Medizinischen Fakultät
der Ludwig-Maximilians-Universität München

vorgelegt von
Sijia Zhang

aus
Henan / China

Jahr
2025




Mit Genehmigung der Medizinischen Fakultät der
Ludwig-Maximilians-Universität zu München

Erstes Gutachten:	Prof. Dr. Arthur Liesz
Zweites Gutachten:	Prof. Dr. Christian Schulz
Drittes Gutachten:	Prof. Dr. Lars Kellert
Viertes Gutachten:	Priv. Doz. Dr. Gunther Fesl

Dekan:	Prof. Dr. med. Thomas Gudermann
--------	---------------------------------

Tag der mündlichen Prüfung:	18.11.2025
-----------------------------	------------

Affidavit

	LUDWIG- MAXIMILIANS- UNIVERSITÄT MÜNCHEN	Promotionsbüro Medizinische Fakultät		
Affidavit				

Zhang Sijia

Surname, first name

Street

Zip code, town, country

I hereby declare, that the submitted thesis entitled:

Systemic Inflammation Post Stroke Leads to Secondary Organ Dysfunction

is my own work. I have only used the sources indicated and have not made unauthorized use of services of a third party. Where the work of others has been quoted or reproduced, the source is always given.

I further declare that the submitted thesis or parts thereof have not been presented as part of an examination degree to any other university.

Munich, 09.06.2025

place, date

Sijia Zhang

Signature doctoral candidate

Table of Contents

Affidavit	2
List of Abbreviations.....	4
List of Publications.....	6
1. Introduction	7
1.1 The global burden of stroke and the current challenge for therapy	7
1.2 Atherosclerosis and Stroke: A Bidirectional Relationship	8
1.3 Secondary organ dysfunction post stroke.....	9
1.4 Systemic immunity post stroke	10
1.5 Emergent myelopoiesis and trained immunity	10
1.6 Aim of the thesis.....	13
1.7 Summary of the included publications.....	14
1.8 Concluding summary	16
2. Own contributions to the publications.....	18
3. Publication I.....	19
4. Publication II.....	48
5. References	120
6. Acknowledgements.....	128
7. Confirmation of Congruency.....	130

List of Abbreviations

DALY: Disability-adjusted life-year
IVT: Intravenous Thrombolysis
tPA: Tissue Plasminogen Activator
MT: Mechanical Thrombectomy
LVO: Large Vessel Occlusion
DAPT: dual antiplatelet therapy
LDL: Low-density lipoprotein
MMPs: Matrix metalloproteinases
MCAO: Middle cerebral artery occlusion
DAMPs: Damage-associated molecular patterns
HMGB1: High-mobility group box 1
CNS: Central nervous system
PRRs: Pattern recognition receptors
TLRs: Toll-like receptors
RAGE: Receptor for advanced glycation end products
IL-1 β : Interleukin-1 β
IL-6: Interleukin-6
TNF- α : Tumor necrosis factor-alpha
CRP: C-reactive protein
MCP-1: Chemoattractant protein-1
HSPCs: Hematopoietic stem and progenitor cells
NETs: Neutrophil extracellular traps
ScRNA-seq: Single-cell RNA sequencing
NADPH: nicotinamide adenine dinucleotide phosphate
Reactive oxygen species: ROS
Gasdermin D: GSDMD
FasL: Fas ligand
cfDNA: Cell-free DNA TRIM: Trained immunity
TRIM: Trained immunity
H3K4me3: Trimethylation of Histone H3 at Lysine 4
CCR2: C-C chemokine receptor type 2

PAMPs: Pathogen-associated molecular patterns

LV: Left ventricular

ECM: Extracellular matrix

Matrix metalloproteinase 2: MMP-2

Matrix metalloproteinase 9: MMP-9

ChIP-seq: Chromatin immunoprecipitation sequencing

TF: Transcription factor

BMT: Bone marrow transplantation

CVC: Cenicriviroc

CCA: Common carotid artery

List of Publications

1. Simats A*, **Zhang S***, Messerer D, Chong F, Beşkardeş S, Chivukula AS, Cao J, Besson-Girard S, Montellano FA, Morbach C, Carofiglio O, Ricci A, Roth S, Llovera G, Singh R, Chen Y, Filser S, Plesnila N, Braun C, Spitzer H, Gokce O, Dichgans M, Heuschmann PU, Hatakeyama K, Beltrán E, Clauss S, Bonev B, Schulz C, Liesz A. Innate immune memory after brain injury drives inflammatory cardiac dysfunction. *Cell*. 2024 Aug 22;187(17):4637-4655.e26. doi: 10.1016/j.cell.2024.06.028. Epub 2024 Jul 22.
2. Cao J, Roth S, **Zhang S**, Kopczak A, Mami S, Asare Y, Georgakis MK, Messerer D, Horn A, Shemer R, Jacqmarcq C, Picot A, Green JP, Schlegl C, Li X, Tomas L, Dutsch A, Liman TG, Endres M, Wernsdorf SR, Fürle C, Carofiglio O, Zhu J, Brough D; DEMDAS Study Group; Hornung V, Dichgans M, Vivien D, Schulz C, Dor Y, Tiedt S, Sager HB, Grosse GM, Liesz A. DNA-sensing inflammasomes cause recurrent atherosclerotic stroke. *Nature*. 2024 Sep;633(8029):433-441. doi: 10.1038/s41586-024-07803-4. Epub 2024 Aug 7.

1. Introduction

1.1 The global burden of stroke and the current challenge for therapy

Ischemic stroke has been a major health challenge for centuries, significantly contributing to mortality and long-term disability. According to the up-to-date estimation of global stroke burden, stroke remains the second leading cause of death among non-communicable disorders and the fourth leading cause of disability-adjusted life-year (DALY) counts combined worldwide [1-3]. It occurs due to an obstruction in blood circulation to a specific brain region, resulting in neuronal cell death. This primary injury triggers a cascade of following pathological events, including excitotoxicity, oxidative stress, inflammation, and apoptosis, which collectively exacerbate the ischemic damage and worsen clinical outcomes [4-6].

The management of acute ischemic stroke primarily aims to rapidly restore cerebral perfusion, prevent further neurological damage, and improve patient outcomes [7]. Currently, approved therapies for AIS focus on reperfusion strategies, supportive care, and secondary prevention to reduce the risk of recurrence. Reperfusion therapy is aimed at restoring blood flow to the ischemic brain tissue as quickly as possible, with two primary approaches currently approved: Intravenous Thrombolysis (IVT) with Tissue Plasminogen Activator (tPA) administered within 4.5 hours of symptom onset, and Mechanical Thrombectomy (MT) for Large Vessel Occlusion (LVO) stroke performed within 6 hours of stroke onset or 24 hours in selected patients based on imaging criteria [8]. Beyond reperfusion, intensive supportive care such as blood pressure management, glucose control, and fever management plays a crucial role in improving stroke outcomes [9-11].

Another key aspect of post-stroke management is secondary prevention, aimed at reducing the risk of recurrent ischemic events [12]. Standard strategies include antithrombotic therapy, such as aspirin or dual antiplatelet therapy (DAPT: aspirin + clopidogrel/ticagrelor) in selected cases, lipid-lowering therapy with high-intensity statins to slow the progression of atherosclerosis, and risk factor control, including hypertension, diabetes, and atrial fibrillation management. Lifestyle modifications such as smoking cessation, a healthy diet, and regular physical activity further support stroke prevention. Despite these established strategies, the risk of early recurrent stroke remains high, with over 10% experiencing recurrent ischemic events within 1 year of the initial stroke [13,14]. Among all stroke subtypes, patients with large artery atherosclerosis show the greatest risk of early recurrent stroke [15]. This finding

indicates that the risk of atherosclerotic plaques remains substantial despite current post-stroke medical preventions.

Beyond recurrence, managing stroke survivors in the chronic phase faces significant challenges. Many patients experience long-term functional impairments, including motor, cognitive, and speech deficits, which impact their independence and quality of life [16]. In addition to neurological deficits, long-term non-neurological dysfunction, such as cardiovascular complications, further disturb the recovery by diminishing the capacity for physical activity and thus lead to a worse outcome [17-19]. As global stroke incidence rises due to an aging population and advancements in acute stroke management, the number of chronic stroke patients continues to grow [1]. This expanding patient cohort underscores the need for mechanistic research to better understand the long-term systemic consequences of stroke and improve rehabilitation strategies.

1.2 Atherosclerosis and Stroke: A Bidirectional Relationship

Atherosclerosis is a major contributor to ischemic stroke, characterized by the progressive accumulation of lipid-rich plaques within the arterial walls, leading to vascular narrowing and increased risk of thrombotic occlusions [20,21]. Plaque rupture can trigger thrombus formation, obstructing cerebral arteries and causing ischemic stroke [22]. Chronic inflammation is a key driver of plaque instability. Modified low-density lipoprotein (LDL) species, such as oxidized LDL, act as chemoattractant for monocytes and induce endothelial cells to express adhesion molecules, chemotactic factors, and growth factors, promoting monocyte recruitment to the arterial wall [23,24]. These monocytes differentiate into macrophages, which engulf oxidized LDL to form foam cells. The release of pro-inflammatory cytokines further stimulates smooth muscle cell migration and extracellular matrix deposition, promoting plaque progression [25,26]. Inflammatory mediators also play a crucial role in plaque rupture. Matrix metalloproteinases (MMPs), secreted by immune cells within the plaque, degrade the fibrous cap, making the plaque prone to rupture. This is followed by platelet aggregation and clot formation, increasing the risk of ischemic stroke [27-29]. Importantly, stroke itself can exacerbate systemic inflammation [30], potentially accelerating atherosclerosis progression and increasing the risk of recurrent ischemic events. Epidemiological studies suggest that inflammatory biomarkers correlate with plaque

instability in stroke patients [31], but the precise mechanisms linking stroke-induced inflammation to atheroprogession remain less understood.

1.3 Secondary organ dysfunction post stroke

The prevalence of secondary organ comorbidities following stroke significantly impacts both patient recovery and the long-term quality of life of stroke survivors. Among these complications, cardiovascular dysfunction is particularly common [17,32,33]. Epidemiological studies found that severe adverse cardiac events occur in 10% to 20% of patients within the first few days after stroke, even in those without preexisting cardiac disease [32,34,35]. These severe cardiac events are more prevalent in patients with severe strokes [36]. Beyond the acute phase, cardiovascular complications continue to significantly influence the long-term prognosis of stroke survivors. A recent Canadian population-based study of adults aged ≥ 66 years indicated that risk of major adverse cardiovascular events was increased 25-fold in the first 30 days compared with matched controls, and it remained >2 times higher during the first year after ischemic stroke [37]. Experimental evidence from a mouse model of transient middle cerebral artery occlusion (MCAO) further supports these findings, demonstrating an early cardiac dysfunction, with a 10–15% reduction in left ventricular function, accompanied by myocardial injury, reflected by a 3- to 5-fold increase in high-sensitivity cardiac troponin (hs-cTn), bradycardia, cardiomyocyte atrophy, and cardiac weight loss, persisting for up to 14 days [38].

Beyond cardiovascular complications, stroke survivors frequently experience infections, which pose serious threats to survival. A meta-analysis reported that pneumonia and urinary tract infections occur in approximately 10% of stroke patients, with pneumonia being associated with an increased risk of mortality [39]. Additionally, respiratory system dysfunction is common after stroke, with over 60% of first-time stroke patients experiencing apneas and hypoventilation [40,41]. Similar findings have been demonstrated in experimental stroke models, where respiratory dysfunction was observed in mice following brain ischemia [42]. In sum, given the significant burden of secondary complications in stroke survivors, further research is essential to elucidate the mechanisms contributing to these conditions.

1.4 Systemic immunity post stroke

In addition to neuroinflammation, stroke triggers a significant systemic inflammatory response that significantly impacts patient outcomes. Within hours after stroke onset, the blood-brain barrier integrity is compromised, leading to the release of damage-associated molecular patterns (DAMPs) into the circulation [30]. These DAMPs, which include high-mobility group box 1 (HMGB1) [43,44], heat shock proteins [45], S100 proteins [46], and others [47], are produced by necrotic and stressed cells both within the ischemic brain and outside the central nervous system (CNS). Once accumulated in the bloodstream, DAMPs could further interact with pattern recognition receptors (PRRs) such as Toll-like receptors (TLRs) and the receptor for advanced glycation end products (RAGE) on peripheral immune cells, including monocytes, macrophages, neutrophils, and dendritic cells [48,49]. This interaction leads to the activation of these cells and the subsequent production of pro-inflammatory cytokines and chemokines, such as interleukin-1 β (IL-1 β), interleukin-6 (IL-6), and tumor necrosis factor-alpha (TNF- α), as well as acute-phase reactants like C-reactive protein (CRP) [50-55], further amplifying the systemic inflammatory response. The outcome of the systemic immune activation after stroke has been revealed in previous studies. For instance, stroke-induced HMGB1 release could promote the infiltration of monocyte and endothelial activation of atherosclerotic plaques via the RAGE–signaling cascade and thus, increase plaque load and vulnerability [49].

Beyond acute activation, emerging studies suggest that systemic immune activation may persist long term after stroke. For example, increased plasma levels of HMGB1, monocyte chemoattractant protein-1 (MCP-1), and CRP have been observed in ischemic stroke patients for up to 90 days post-stroke [56-58]. However, the precise sources of these inflammatory mediators and their long-term impact on peripheral organ function remain poorly understood. Given the potential link between persistent systemic inflammation to remote organ dysfunction, including cardiovascular and pulmonary complications, further investigations are needed to understand the precise mechanisms.

1.5 Emergent myelopoiesis and trained immunity

Besides the leukocytes in the blood stream, stroke also triggers substantial adaptation in bone marrow hematopoietic stem and progenitor cells (HSPCs). HSPCs act as central regulators of hematopoiesis, with high responsiveness to extrinsic signals such as hormones, microbiome-

derived metabolites and inflammatory mediators released during tissue damage [59-62]. Under acute insults such as infection or hemorrhage, HSPCs undergo transcriptional, epigenetic, and metabolic remodeling to prioritize rapid myeloid cell production—a process termed emergency myelopoiesis—while suppressing lymphoid lineage generation [63-66]. Stroke has also been shown to trigger this process, resulting in myeloid bias in hematopoiesis, elevated bone marrow output of inflammatory Ly6C^{high} monocytes and neutrophils, and reduced lymphoid progenitor activity [67].

Among the innate immune cells generated during this process, neutrophils, the most abundant immune cells in human peripheral blood, can contribute to excessive inflammation when their production and activation become dysregulated via aberrant phagocytosis, degranulation, and the release of neutrophil extracellular traps (NETs) [68]. Under homeostasis, neutrophils are short-lived, and their generation is a tightly regulated process, taking more than ten days from HSCs to mature neutrophils, which are stored in the bone marrow and released upon stimulation [69]. Recent single-cell RNA sequencing (scRNA-seq) experiments have revealed that neutrophils can bypass full maturation before entering circulation. In healthy mice, these immature neutrophils constitute approximately 5% of peripheral neutrophils [70]. Upon pathological insults such as infection, this homeostasis is disrupted, leading to the excessive release and accumulation of the immature neutrophils in circulation, a phenomenon known as neutrophils left shift [71]. Data from scRNA-seq suggested those immature neutrophils exhibit functional heterogeneity compared with fully mature neutrophils, with reduced phagocytosis capacity and chemotaxis, but higher expression of nicotinamide adenine dinucleotide phosphate (NADPH) oxidase-related genes [70]. This enhanced NADPH oxidase activity reflects greater potential for reactive oxygen species (ROS) production, which is essential for NET formation and release during stimulation [72]. On one hand, emergent myelopoiesis is crucial for controlling infections. However, a recent study found that severe COVID-19 cases, compared to mild or moderate disease, were strongly associated with an increased presence of immature myeloid cells—both neutrophils and monocytes—characterized by reduced expression of the neutrophil marker CD10 and monocyte marker HLA-DR [73]. Another study further demonstrated that heightened expression of the cell cycle marker Ki-67 in monocytes correlated with COVID-19 severity [74], suggesting that excessive emergent myelopoiesis may be detrimental. Notably, immature neutrophils released during acute inflammation exhibit efficient trans-endothelial migration despite incomplete nuclear segmentation [75]. Given these findings, more research

is needed to understand how emergency myelopoiesis exacerbates immune dysregulation and whether it influences secondary complications after stroke.

In addition to neutrophils, monocytes are also rapidly activated and mobilized from the bone marrow and spleen in the acute phase after stroke [67,76]. Once released into the bloodstream, these monocytes infiltrate the ischemic brain tissue through the compromised blood–brain barrier and differentiate into macrophages—a process that has been shown to depend on the C-C chemokine receptor type 2 (CCR2) and its ligand CCL2 [77,78]. Beyond their infiltration into the injured brain, activated monocytes also contribute to systemic inflammation following stroke. One key mechanism by which monocytes and macrophages mediate both neuroinflammation and systemic inflammation is via inflammasome activation [79,80]. Inflammasomes are intracellular protein complexes that respond to DAMPs by activating caspase-1, leading to the release of pro-inflammatory cytokines such as IL-1 β and IL-18. Mature caspase-1 also cleaves gasdermin D (GSDMD), whose N-Terminal leads to pores in the cell membrane and the swelling of cells, finally resulting in the rupture of the membrane, cell swelling, and a form of programmed cell death which is termed pyroptosis, thus amplifies inflammation [81]. Beside caspase-1, myeloid cells can also respond to the pathogen through the non-canonical inflammasome pathway including caspase-4, caspase-5 (in human) and caspase-11 (in mice), which also lead to pyroptosis by cleaving GSDMD. They can also trigger the secondary activation of the NLRP3 inflammasome to promote caspase-1–dependent cytokine maturation [82]. The systemic consequence of monocytes inflammasome activation after stroke has been demonstrated by a previous study showing that AIM2 inflammasome-dependent IL-1 β secretion by myeloid cells in response to cell-free DNA (cfDNA) results in Fas ligand (FasL) upregulation in monocytes and extrinsic T cell apoptosis [47], suggesting critical roles of monocytes and macrophages in the post-stroke systemic inflammation.

Beyond the acute activation of HSPCs, which amplifies the early inflammatory response following stroke, dysregulated myelopoiesis following chronic inflammatory conditions, such as hypercholesterolemia and rheumatoid arthritis, have been strongly associated with accelerated atheroprogession and increased cardiovascular disease risk [83-85]. Recent research has shown that innate immune cells, including monocytes, macrophages, dendritic cells, and HSPCs, can undergo long-term functional reprogramming in response to specific stimuli thus, reshaping the immune microenvironment [86,87]. This phenomenon is termed

trained immunity (TRIM), which is mainly driven by epigenetic modifications and changes in cellular metabolism [88,89]. TRIM has been observed following microbial infections and vaccinations, where it enhances the host's defense against pathogens [89-92]. However, TRIM has also been implicated in sterile inflammatory conditions, such as organ transplantation and metabolic disorders [93,94]. In these contexts, the enhanced immune response triggered by the initial stimuli can exacerbate hyperinflammation. For instance, after organ transplantation, trained macrophages upregulate co-stimulatory molecules and produce pro-inflammatory cytokines, driving potent graft-reactive immune responses and contributing to organ transplant rejection [95].

DAMPs like HMGB1, oxidized LDL, and extracellular heme have been shown to induce long-term reprogramming of innate immune cells [93,96,97]. Growing evidence also highlights the essential role of IL-1 family cytokines, produced by immune cells in response to both pathogen-associated molecular patterns (PAMPs) and DAMPs [98], in enabling innate immune cells to acquire training features upon stimulation [99]. For instance, IL-1 signaling is required for the β -Glucan induced training of bone marrow HSPCs: blockade of IL-1 β signaling prevents the β -glucan-induced myeloid-skewing [100-103]. Consistently, IL-1 β production capacity of human monocytes after BCG vaccination is strongly correlated with lower viremia upon subsequent yellow fever virus challenge [90]. Mechanistically, exogenous IL-1 β stimulation of human monocytes is capable of establishing epigenetic marks, shown as enhanced trimethylation of histone H3 at lysine 4 (H3K4me3) at the promoter regions of IL-1 β , IL6, and TNF [90], and IL-1 β signaling is required for the glycolytic shift during TRIM: IL-1 receptor antagonist prevents β -glucan-induced enhancement of glycolysis [100]. Given the widespread release of DAMPs and IL-1 cytokines following stroke, it is plausible that TRIM occurs post-stroke and may even contribute to the chronic systemic immune activation and the secondary organ dysfunction after stroke, which remains an open question that needs further exploration.

1.6 Aim of the thesis

The primary aim of this thesis is to investigate the systemic immune activation following stroke and its potential impact on secondary events and remote organ dysfunction. To achieve this, the study is structured around four main goals:

1. To detect acute inflammasome activation after stroke, identify its triggers, and assess its impact on atherosclerotic plaque destabilization and early recurrent stroke.
2. To characterize chronic systemic immune responses post-stroke, including changes in the peripheral organs, bone marrow HSPCs, and circulating immune cells.
3. To examine pathological changes in the heart during the chronic phase following stroke.
4. To evaluate potential immunomodulatory interventions that could regulate systemic immune activation and alleviate peripheral organ complications.

By addressing these questions, this thesis aims to provide new insights into the interplay between systemic immune responses and multi-organ dysfunction after stroke and help develop targeted therapeutic approaches to improve long-term outcomes for stroke survivors.

1.7 Summary of the included publications

In our first study [104], we investigated the role of DNA-sensing inflammasomes, particularly the AIM2 inflammasome, in post-stroke atherosclerotic plaque destabilization. We utilized a newly developed mouse model that mimics high-risk carotid artery plaques, which are prone to rupture. We performed stroke in these mice and observed increased inflammation, plaque destabilization, and stroke recurrence. Using this experimental model, we demonstrated that stroke increases circulating cfDNA, which activates AIM2 in atherosclerotic plaques. AIM2 activation triggered caspase-1 cleavage and IL-1 β release, promoting local inflammation. This leads to enhanced expression of matrix metalloproteinases 2 (MMP2) and MMP9, degradation of the fibrous cap, plaque rupture, and recurrent stroke. Inhibition of AIM2 inflammasome activation with a caspase-1 inhibitor prevented post-stroke activation of plaque MMPs and subsequent rupture. We further identified neutrophil NETosis as the primary source of circulating cfDNA. Both depleting neutrophils with neutralizing antibody and inhibiting NETosis reversed the CCA inflammasome activation. DNase administration following stroke significantly reduced inflammasome activation, MMP expression, plaque rupture, and the rate of recurrent strokes, suggesting its potential as a therapeutic strategy. Finally, we validated our findings in human stroke patients with a significant increase in circulating plasma cfDNA and elevated MMP9 activity in plaques from patients in the acute phase of stroke compared to asymptomatic patients. These results confirmed the presence of DNA-mediated inflammasome activation, vascular inflammation, and MMP induction in human stroke, consistent with our animal model.

In our second study [105], we investigated how stroke triggers chronic innate immune dysregulation and the following cardiac dysfunction. We utilized transient MCAO model in mice to induce stroke and analyzed myeloid cells in peripheral organs up to three months. Single-cell sequencing revealed that acute brain ischemia induces long-lasting pro-inflammatory changes in myeloid cells across multiple organs, particularly in the heart. Doppler echocardiography revealed that stroke mice developed chronic diastolic dysfunction, characterized by reduced left ventricular (LV) compliance. Histological analysis showed significant cardiac fibrosis, which persisted for up to three months post-stroke. We identified higher expression of matrix metalloproteinase 9 (MMP-9) enzyme, which plays a key role in the tissue remodeling, by cardiac monocytes/macrophages at 1 month after stroke. These findings were validated in human patients. Autopsy samples from stroke patients revealed increased fibrotic tissue deposition and elevated numbers of MMP-9 transcripts in monocytes/macrophages compared to non-stroke controls.

To explore the potential mechanisms of post-stroke cardiac dysfunction, we performed scRNA-seq and flow cytometry analysis of heart tissue, and identified an expansion of cardiac Ly6C^{high} monocytes, which differentiated into tissue resident macrophages and contributed to tissue remodeling. Similarly, using an inducible myeloid progenitor reporter mouse strain (Ms4a3^{creERT2}xAi14), we observed increased recruitment of circulating monocytes/macrophages into the heart, which persist as a long-term consequence of stroke. We further studied the contribution of peripheral monocytes to heart fibrosis using an inducible reporter mouse strain under control of the Ccr2 promoter to label infiltrating monocytes (Ccr2^{creERT2}xAi14). Through scRNA-seq, we identify a persistent inflammatory signature in the infiltrated Ccr2⁺ monocytes and macrophages, characterized by upregulated pathways related to cytokine signaling, chemotaxis, and extracellular matrix (ECM) remodeling. To track the source of those pro-inflammatory monocytes, we analyzed the bone marrow HSPCs and monocytes and observed increased myelopoiesis at the chronic phase after stroke, with abundant pro-inflammatory transcriptional changes. We also analyzed the epigenetic landscape of bone marrow HSPCs and monocytes after stroke using chromatin immunoprecipitation sequencing (ChIP-seq). Specifically, we identified histone H3K4me3 modifications in HSPCs to be tightly related with the differential enrichment of several transcription factor (TF) motifs including CTCF, STAT1/2, GABPA, CEBPD, GFI and KLF14, which are known to regulate the survival and proliferation of HSPC, their differentiation towards the myeloid lineage and their inflammatory phenotype. Similarly, we

also found histone H3K4me3 modifications in mature monocytes which were tightly related to TF motifs associated with pro-inflammatory signaling pathways. To further investigate the impact of these epigenetic modifications, we conducted a bone marrow transplantation (BMT) experiment: bone marrow from stroke mice was transplanted into naive mice, which subsequently developed cardiac inflammation and fibrosis, despite never experiencing a stroke, indicating that the changes in the bone marrow after stroke are sufficient to drive secondary cardiac fibrosis. We further identified IL-1 β as a key driver of this process and demonstrated that it promotes epigenetic reprogramming in bone marrow HSPCs, leading to sustained production of inflammatory monocytes. Neutralizing IL-1 β early after stroke prevented most of the stroke-induced changes in chromatin accessibility in both HSPC and mature monocytes, and the following cardiac pathology. Considering the translational use of anti-IL-1 β in stroke patients is limited by an increased risk of infections, as reported in a previous clinical trial [106], we utilized an alternative intervention by the dual C-C chemokine receptors type 2 and 5 antagonist Cenicriviroc (CVC) to block the migration of mature monocytes into the heart after stroke. We found that CVC treatment significantly reduced Mmp9 expression by cardiac monocytes/macrophages and reduced cardiac fibrosis, demonstrating the therapeutic potential of blocking the recruitment of pro-inflammatory monocytes into the heart for the secondary cardiac dysfunction post-stroke.

1.8 Concluding summary

This Ph.D. thesis provides fundamental insights into the systemic immune activation following stroke and its impact on secondary organ dysfunction and recurrent stroke. It systematically investigates immune activation in both the acute and chronic phases post-stroke, identifying key inflammatory pathways that contribute to disease progression. A major finding of this work is the role of circulating cfDNA in triggering inflammasome activation, which initiates a pro-inflammatory cascade leading to atherosclerotic plaque destabilization and thrombosis—a mechanism that significantly increases the risk of early recurrent stroke. Notably, this study identifies neutrophil NETosis as the primary and unexpected source of post-stroke cfDNA, underscoring a novel link between neutrophil activation and recurrent vascular events. Targeting this pathway through NETosis inhibition, cfDNA neutralization, or inflammasome blockade emerges as a promising therapeutic approach for recurrent stroke prevention.

Beyond vascular inflammation, this thesis explores the long-term immune alterations in peripheral organs, with a particular focus on the heart. Persistent immune activation post-stroke is associated with significant cardiac dysfunction, characterized by compromised left ventricular compliance and interstitial fibrosis at the chronic phase. These findings establish a causal link between chronic innate immune dysregulation and post-stroke cardiac pathology. A key mechanistic discovery is the persistent alteration of bone marrow myelopoiesis following stroke. This study identifies both transcriptional and epigenetic changes in HSPCs and mature monocytes, suggesting the emergence of trained immunity in the bone marrow. This results in the sustained production of pro-inflammatory monocytes, which subsequently drive chronic inflammatory cardiac dysfunction. Based on these mechanistic insights, this thesis evaluates potential immunomodulatory interventions. Therapeutic strategies, including the CCR2/CCR5 antagonist CVC and IL-1 β neutralization, effectively prevent post-stroke cardiac dysfunction, demonstrating their potential for clinical translation.

In conclusion, this thesis elucidates a novel immunological framework linking acute stroke-induced systemic inflammation, chronic immune reprogramming, and secondary organ dysfunction, providing a foundation for targeted therapeutic interventions aimed at improving long-term outcomes in stroke survivors.

2. Own contributions to the publications

For the first study, in which I was a co-author, I conducted the experiment in which we evaluated the collagen deposition and orientation in fibrous caps from the common carotid artery (CCA), including the staining with picrosirius red and the imaging with microscopy and its analysis using imageJ software. Moreover, I contributed to parts of the figure creation and manuscript writing and revised the manuscript draft.

For the second study, in which I was the co-first author, I conducted the in vivo cardiac function measurement of mice, histochemistry, immunofluorescence, and fluorescence in-situ hybridization staining of the heart sections, and the flow cytometry analysis of the heart and blood in mice after stroke. I established the second harmonic generation microscopy imaging of the heart sections and its analysis. I performed the cell sorting of the heart and blood monocytes/macrophages and the qPCR analysis. I conducted the heart gelatin zymography experiment. I performed the in vivo treatment with CVC and recombinant IL-1 β and the flow cytometry analysis and the histology analysis of blood and heart in the anti- IL-1 β treatment experiments. I conducted the bone marrow derived monocyte tracking experiment using Ms4a3CreAi14 and the CCR2CreAi14 mouse lines, including the stroke induction, Tamoxifen treatment, and flow cytometry analysis. I participated in the bone marrow transplantation experiment and performed the flow cytometry and histology analysis of the heart. I contributed to the paper writing, figures creation and conducted most of the experiments during the manuscript revision.

3. Publication I

DNA-sensing inflammasomes cause recurrent atherosclerotic stroke

<https://doi.org/10.1038/s41586-024-07803-4>

Received: 28 January 2023

Accepted: 9 July 2024

Published online: 7 August 2024

Open access

 Check for updates

Jiayu Cao^{1,22}, Stefan Roth^{1,22}✉, Sijia Zhang¹, Anna Kopczak^{1,2}, Samira Mami¹, Yaw Asare¹, Marios K. Georgakis^{1,2,3}, Denise Messerer⁴, Amit Horn⁵, Ruth Shemer⁵, Charlene Jacqmarcq⁶, Audrey Picot⁶, Jack P. Green⁷, Christina Schlegl¹, Xinghai Li⁸, Lukas Tomas⁴, Alexander Dutsch⁸, Thomas G. Liman⁹, Matthias Endres^{9,10,11}, Saskia R. Wernsdorf¹, Christina Fürle¹, Olga Carofiglio¹, Jie Zhu¹, David Brough⁷, DEMDAS Study Group*, Veit Hornung¹², Martin Dichgans^{1,2,13,14}, Denis Vivien^{6,15}, Christian Schulz^{4,13,16}, Yuval Dor⁵, Steffen Tiedt¹, Hendrik B. Sager^{8,13}, Gerrit M. Grosse¹⁷ & Arthur Liesz^{1,2}✉

The risk of early recurrent events after stroke remains high despite currently established secondary prevention strategies¹. Risk is particularly high in patients with atherosclerosis, with more than 10% of patients experiencing early recurrent events^{1,2}. However, despite the enormous medical burden of this clinical phenomenon, the underlying mechanisms leading to increased vascular risk and recurrent stroke are largely unknown. Here, using a novel mouse model of stroke-induced recurrent ischaemia, we show that stroke leads to activation of the AIM2 inflammasome in vulnerable atherosclerotic plaques via an increase of circulating cell-free DNA. Enhanced plaque inflammation post-stroke results in plaque destabilization and atherothrombosis, finally leading to arterioarterial embolism and recurrent stroke within days after the index stroke. We confirm key steps of plaque destabilization also after experimental myocardial infarction and in carotid artery plaque samples from patients with acute stroke. Rapid neutrophil NETosis was identified as the main source of cell-free DNA after stroke and NET-DNA as the causative agent leading to AIM2 inflammasome activation. Neutralization of cell-free DNA by DNase treatment or inhibition of inflammasome activation reduced the rate of stroke recurrence after experimental stroke. Our findings present an explanation for the high recurrence rate after incident ischaemic events in patients with atherosclerosis. The detailed mechanisms uncovered here provide clinically uncharted therapeutic targets for which we show high efficacy to prevent recurrent events. Targeting DNA-mediated inflammasome activation after remote tissue injury represents a promising avenue for further clinical development in the prevention of early recurrent events.

Stroke is the second-leading cause of death worldwide³ and a leading cause of long-term disability, with incidence rates rising due to demographic ageing⁴. An important factor contributing to this sociomedical burden is the high risk of recurrent vascular events such as stroke and myocardial infarction. A systematic review and meta-analysis reported a pooled recurrent stroke risk of 11.1% at 1 year^{1,2}. The risk of myocardial infarction is likewise substantially increased in survivors of stroke⁵. The precise mechanisms underlying this increased vascular risk after an

ischaemic event are unclear. It is equally unexplained why the hazards for recurrence are dependent on time and particularly pronounced in the early phase after the event. Previous epidemiological studies have indicated that vascular risk is particularly increased in patients with large-artery atherosclerosis and to a lesser degree in patients with other stroke aetiologies⁶. This suggests an abundant residual vascular risk in patients with atherosclerosis, which is not effectively prevented by current secondary prevention measures.

¹Institute for Stroke and Dementia Research (ISD), LMU University Hospital, LMU Munich, Munich, Germany. ²Munich Cluster for Systems Neurology (SyNergy), Munich, Germany. ³Programme in Medical and Population Genetics, Broad Institute of MIT and Harvard, Cambridge, MA, USA. ⁴Medizinische Klinik und Poliklinik I, LMU University Hospital, LMU Munich, Munich, Germany. ⁵Department of Developmental Biology and Cancer Research, Hebrew University of Jerusalem, Faculty of Medicine, Jerusalem, Israel. ⁶Normandie University, UNICAEN, INSERM UMR-S U1237, Physiopathology and Imaging of Neurological Disorders (PhIND), GIP CyCeron, Institute Blood and Brain @ Caen-Normandie (BB@C), Caen, France. ⁷Geoffrey Jefferson Brain Research Centre, The Manchester Academic Health Science Centre, Northern Care Alliance NHS Group, University of Manchester, Manchester, UK. ⁸Department of Cardiology, German Heart Centre Munich, Technical University of Munich, Munich, Germany. ⁹Center for Stroke Research Berlin (CSB), Charité-Universitätsmedizin Berlin, Berlin, Germany. ¹⁰Department of Neurology, Charité-Universitätsmedizin Berlin, Berlin, Germany. ¹¹German Center for Cardiovascular Research (DZHK), Partner Site Berlin, Berlin, Germany. ¹²Gene Center and Department of Biochemistry, LMU Munich, Munich, Germany. ¹³German Center for Cardiovascular Research (DZHK), Partner Site Munich Heart Alliance, Munich, Germany. ¹⁴German Center for Neurodegenerative Diseases (DZNE), Munich, Germany. ¹⁵Research Clinical Department, Caen Normandie University Hospital, Caen, France. ¹⁶Department of Immunopharmacology, Mannheim Institute for Innate Immunoscience (MI3), Medical Faculty Mannheim, Heidelberg University, Mannheim, Germany. ¹⁷Department of Neurology, Hannover Medical School, Hannover, Germany. ²²These authors contributed equally: Jiayu Cao, Stefan Roth. *A list of authors and their affiliations appears at the end of the paper. ✉e-mail: stefan.roth@med.uni-muenchen.de; arthur.liesz@med.uni-muenchen.de

Atherosclerosis is a chronic inflammatory disease, in which immune cells in atherosclerotic plaques contribute to the progression and evolving vulnerability⁷. We and others have previously shown that stroke leads to a systemic inflammatory response, which can contribute to progression of vascular inflammation and plaque load in established atherosclerosis^{8–10}. Epidemiological data on inflammatory biomarkers and atheroprotection in patients with stroke have suggested that inflammation can be associated with progression of atherosclerosis and even with recurrent ischaemic events^{11,12}.

On the basis of these findings, we formulated the hypothesis that stroke might facilitate the occurrence of subsequent vascular events by inflammatory mechanisms. However, the detailed mechanisms along this supposed brain–immune–vascular axis are currently unknown and therefore specific immunological targets to potentially reduce the rate of early recurrence after stroke are missing. A potential reason for this lack of information on such a pressing biomedical question might be the lack of suitable animal models to study recurrent ischaemic events. Commonly used models for atherosclerosis in rodents differ from the situation in high-risk patients with cardiovascular disease in that the atherosclerotic plaques are less complex, not prone to rupture and barely affect the cerebrovascular circulation.

Here we developed an adapted mouse model of rupture-prone high-risk plaques of the carotid artery in combination with contralateral experimental stroke or with myocardial infarction. We found that both stroke and myocardial infarction induced a destabilization of atherosclerotic plaques, leading to recurrent ischaemic events. We identified activation of the AIM2 inflammasome by cell-free DNA (cfDNA) derived from neutrophil extracellular traps (NETs) as the immunological mechanism leading to plaque destabilization via matrix metalloproteinase (MMP) activation, finally leading to atherothrombosis and arterial embolism. The same pathophysiological processes were confirmed in human atherosclerotic plaques obtained from patients within the first days after an acute ischaemic stroke. Targeting this immunological pathway efficiently prevented recurrent ischaemic events after experimental stroke.

Stroke recurrence in atherosclerosis

As previous epidemiological data on stroke recurrence by stroke aetiology are more than 20 years old⁶ and clinical practice has substantially changed in this time period, we assessed the recurrence rate of cerebrovascular events (stroke and transient ischaemic attack) using pooled data ($n = 1,798$ patients with stroke) from two ongoing clinical cohorts with information on aetiology of the first stroke according to TOAST criteria^{13,14}. Focusing on the early phase after stroke (days 0–30 after the index event), recurrence rates were markedly higher in patients with large-artery atherosclerotic (LAA) stroke than in other stroke aetiologies and nearly as high as for the entire period from days 31–360 combined (Fig. 1a and Extended Data Fig. 1a). This indicates that current strategies for secondary stroke prevention fail to efficiently reduce early recurrent events in patients with LAA stroke. This clinical notion was further confirmed by treating atherosclerotic mice undergoing experimental stroke with high-dose rosuvastatin and aspirin—the current standard scheme for secondary stroke prevention in patients. This high-dose treatment had no effect on mortality, vascular inflammation and plaque load within the first week after experimental stroke (Extended Data Fig. 1b–f), confirming the inefficiency of current secondary prevention therapy on early atherosclerotic plaque progression within the first week after stroke. To study the mechanisms underlying the increased risk of recurrent events in patients with atherosclerosis, we established an animal model of unilateral highly stenotic and haemodynamically relevant atherosclerotic plaques of the common carotid artery (CCA). This involved the induction of turbulent flow by a stenotic tandem ligation (Extended Data Fig. 2a–f). We used this model to test the effects of experimentally induced acute ischaemic

stroke in the hemisphere contralateral to the CCA tandem stenosis on atherosclerotic plaque morphology and destabilization (Fig. 1b). We screened for the occurrence of secondary ischaemic events in the brain hemisphere supplied by the stenotic atherosclerotic CCA (that is, contralateral to the experimentally induced stroke) by magnetic resonance imaging (MRI) and histological analysis of cell loss (Fluoro Jade C and TUNEL staining) and microgliosis (Fig. 1c). We found that experimental stroke resulted in secondary brain ischaemia in 30% of the animals with secondary lesions mainly located in the middle cerebral artery (MCA) territory (Extended Data Fig. 2g–i). By contrast, this was not observed in any of the animals with CCA tandem stenosis and sham surgery or atherosclerotic animals without CCA tandem stenosis (Fig. 1c and Extended Data Fig. 2j–l). This observation suggested stroke-induced rupture of remote CCA plaques leading to secondary stroke events. This hypothesis was further supported by the identification of plaque rupture and intravascular thrombus formation at the site of the CCA stenosis, which was significantly associated with the occurrence of secondary brain lesions after stroke (Fig. 1d). Correspondingly, the plaque vulnerability index for the stenotic CCA (a previously established score of several morphological markers indicating plaque risk to rupture¹⁵; Extended Data Fig. 3a–f) was significantly increased in mice after experimental stroke and was even further exacerbated in mice with secondary events after the primary stroke (Fig. 1e). Fibrotic cap thickness, which contributes to plaque stability, was significantly decreased after stroke (Extended Data Fig. 3d), and histological indication of plaque rupture was observed in 40% of mice after stroke compared with 10% of mice undergoing sham surgery (Extended Data Fig. 3g). We further validated the concept of secondary remote plaque rupture in a model of myocardial infarction. Similar to stroke, myocardial infarction increased vulnerability of the remote CCA plaque (Fig. 1f and Extended Data Fig. 4a–e). Flow cytometry analysis of CCA plaques revealed increased cellular plaque inflammation after stroke compared with sham surgery (Extended Data Fig. 4f,g). We further analysed the mechanism of enhanced immune cellularity either by invasion or proliferation using antibody labelling of circulating immune cells or histological assessment of the proliferation marker Ki67, respectively. We found that both the de novo recruitment and local proliferation of leukocytes were increased after stroke (Fig. 1g–i) and that the local proliferation rate was associated with the occurrence of recurrent events (Fig. 1i).

Post-stroke DNA activates AIM2 in plaques

Further analyses of the inflammatory milieu in atherosclerotic CCA plaques revealed a substantial increase in local IL-1 β production after stroke, suggesting stroke-induced inflammasome activation within atherosclerotic plaques (Fig. 2a). Local inflammasome activation was confirmed by western blot analysis of cleaved caspase-1—the effector enzyme of the inflammasome—in the atherosclerotic plaque and flow cytometric analysis using FAM, a fluorescent molecule that selectively binds to activated caspase-1, for cell-based analysis of inflammasome activation in plaque macrophages (Fig. 2b) and independently verified by histological analysis with increased caspase-1 expression in CCA plaques after stroke (Extended Data Fig. 5a–d). Blocking inflammasome activity by a caspase-1 inhibitor (VX765) prevented the proliferation of immune cells within CCA plaques after stroke and attenuated the invasion of pro-inflammatory circulating monocytes (Fig. 2c,d). Consequently, inflammasome inhibition significantly reduced plaque vulnerability after experimental stroke to levels comparable with sham-operated mice (Fig. 2e and Extended Data Fig. 5e–g). We next investigated which specific inflammasome mediates this effect of stroke on CCA plaque exacerbation by applying specific pharmacological inhibitors of the NLRP3 (MCC950) or a novel AIM2 inflammasome inhibitor¹⁶ (4-sulfonic calixarene), which we found to dose-dependently displace DNA, which is the ligand of

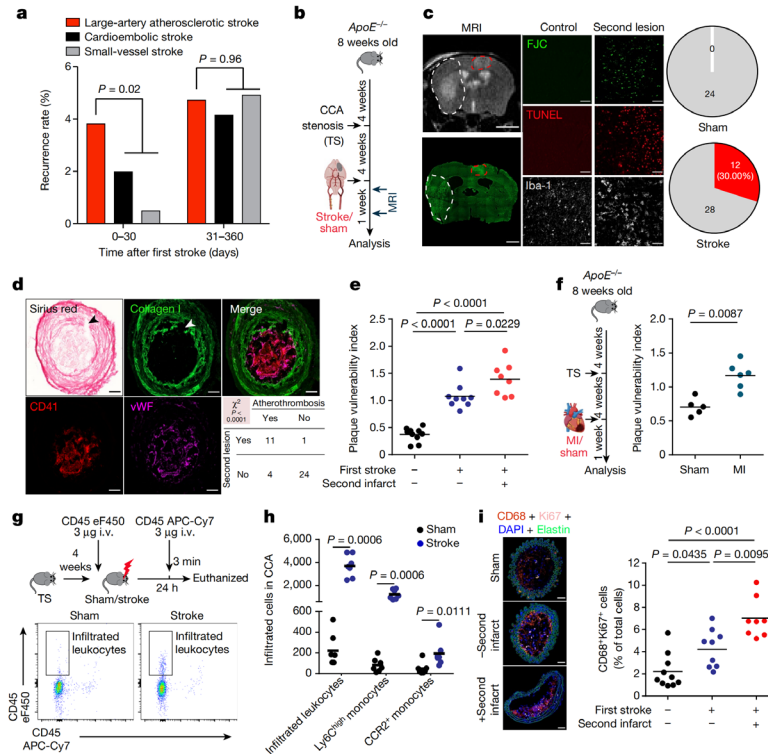


Fig. 1 | Ischaemic events induce recurrent stroke and exacerbate plaque vulnerability. **a**, Recurrence rates by incident stroke aetiology in the first month (days 0–30) and months 2–12 (days 31–360) in a population of 1,798 patients with stroke (log-rank test in Kaplan–Meier curves; Extended Data Fig. 1a). **b**, Experimental design. Eight-week-old high-cholesterol diet (HCD)-fed ApoE^{-/-} mice underwent tandem stenosis (TS) surgery, and stroke or sham surgery 4 weeks later. The recurrence of secondary ischaemia in the contralateral hemisphere was examined by MRI and histological analysis. **c**, Representative MRI image (the white dashed line denotes the primary stroke area; the red dashed line indicates recurrent contralateral stroke). FluoroJade C (FJC; lower left panel) staining corresponding to MRI. Scale bars, 3 mm. Representative images of histological stainings (FJC, TUNEL and Iba-1) from control mice or mice with a secondary lesion (middle panels). Scale bars, 50 μ m. Pie charts for stroke recurrence 7 days after sham or stroke surgery ($n = 24$ (sham) and $n = 40$ (stroke); red denotes with secondary lesion, and grey indicates without

secondary lesion) are also shown (right panels). **d**, Representative images of a plaque rupture (the arrowheads in the Sirius red and collagen I stainings) with contiguous CCA thrombus stained for von Willebrand factor (vWF) and platelets (CD41). Chi-squared test ($P < 0.0001$) for occurrence of CCA thrombi and secondary brain lesions ($n = 12$ per group). Scale bars, 50 μ m. **e**, Quantification of plaque vulnerability in CCA sections 7 days after sham or stroke surgery (analysis of variance (ANOVA); $n = 9-10$ per group). **f**, Experimental design as shown in panel b, but with induction of myocardial infarction (MI) instead of stroke (left), and quantification of plaque vulnerability (right; U-test; $n = 5-6$ per group). **g**, **h**, Experimental design and representative FACS plots (g) for quantification (h) of infiltrated leukocytes and Ly6C^{high} and CCR2⁺ monocyte subpopulations in CCA 24 h after sham or stroke surgery (U-test; $n = 6$ per group). i.v., intravenous. **i**, Representative images (left) and quantification (right) of proliferating macrophages (ANOVA; $n = 8-10$ per group). Scale bars, 50 μ m. **e**, **f**, **h**, **i**, Bars indicate the mean.

the AIM2 inflammasome (Extended Data Fig. 6a,b). We focused on these two abundant inflammasome subtypes, because the NLRP3 inflammasome has previously been implicated in the development of atherosclerosis, whereas stroke leads to systemic AIM2 inflammasome activation^{17,18}. Both the inhibition of AIM2 and NLRP3 prevented inflammasome activation in the CCA plaque after stroke, with greater efficacy of the AIM2 inhibitor, whereas only the AIM2 inhibitor significantly prevented the post-stroke increase in IL-1 β levels in the CCA plaque (Fig. 2f,g and Extended Data Fig. 6c).

Moreover, we observed a transient increase in the serum concentration of cfDNA in the acute phase after stroke and myocardial infarction, suggesting that release of cfDNA after stroke and myocardial infarction could be the mediator linking remote organ ischaemia to the exacerbation of plaque inflammation (Fig. 2h and Extended Data Fig. 6d,e). The increased cfDNA after stroke was mainly DNA of less than 400 bp in length and confirmed to be primarily extracellularly located (Extended Data Fig. 6f–h). To test the causative

function of cfDNA, we injected DNA into mice with a CCA stenosis without stroke or sham surgery and observed increased plaque inflammasome activation similar to the condition after stroke (Fig. 2i,j and Extended Data Fig. 7a,b). Correspondingly, stimulation of wild-type (WT) bone marrow-derived macrophages (BMDMs), but not of AIM2-deficient BMDM, with DNA led to oligomerization of the inflammasome adaptor protein ASC as an indicator of physical inflammasome formation (Fig. 2k). Moreover, caspase-1 activation was completely blunted in ASC-deficient or AIM2-deficient, but not in cGAS-deficient, NLRP1-deficient or NLRP3-deficient, BMDMs in response to stimulation with serum from stroke mice or stimulation with DNA (Extended Data Fig. 7c,d). To further analyse in vivo, the role of the AIM2 inflammasome in myeloid cells, we performed bone marrow transfer using a genetic bone marrow depletion model (poly(I:C) administration to *Mx1^{cre};c-myb^{fl/fl}* mice) on the genetic background of atherogenic LDL-receptor-deficient mice to avoid confounding effects by irradiation or chemotherapy (Fig. 2l). *Aim2^{wt}* or *Aim2^{-/-}* bone

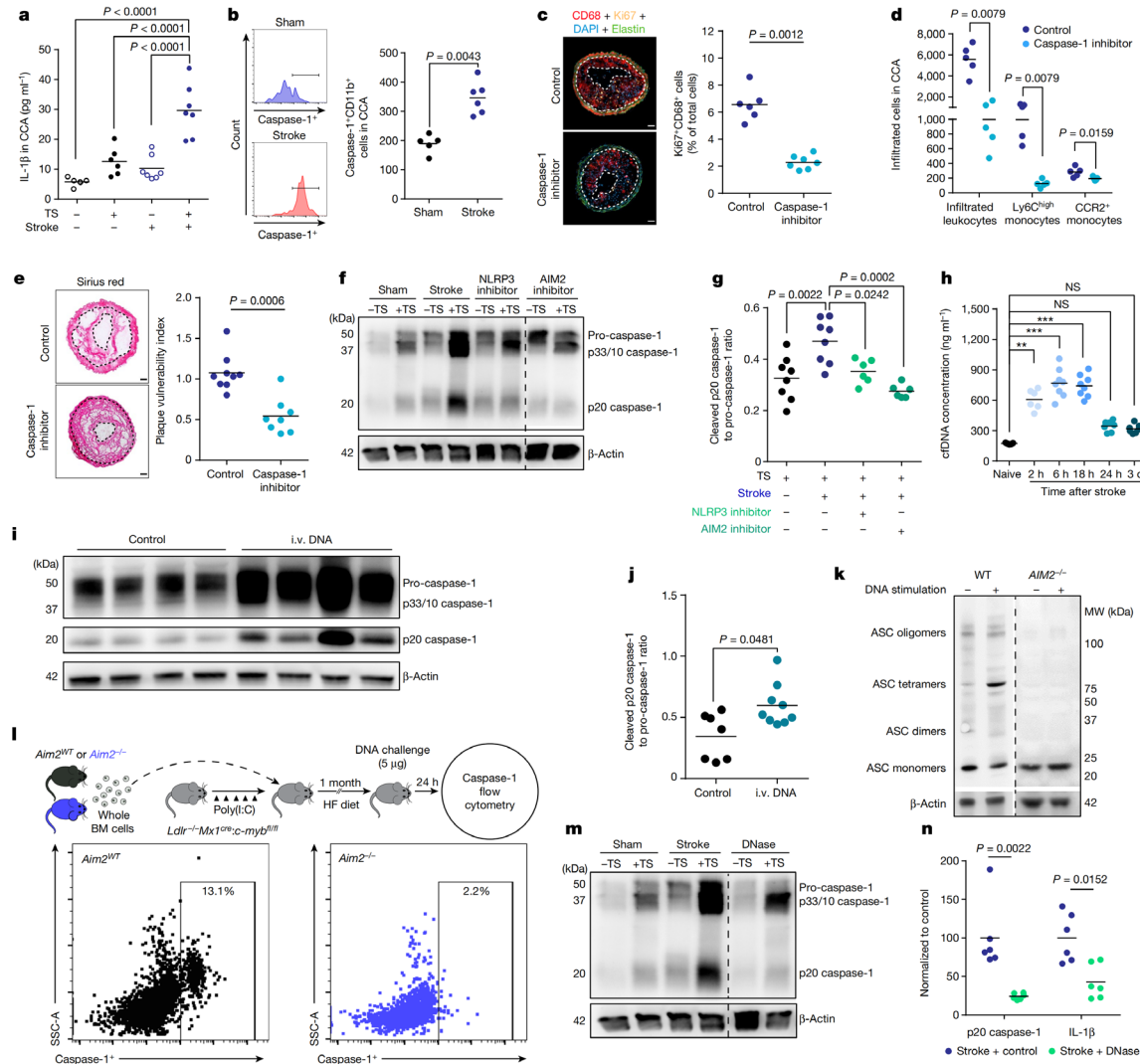


Fig. 2 | Stroke induces double-stranded DNA-dependent inflammasome activation in atherosclerotic plaques. **a, b**, IL-1 β concentrations (*K*-test, $n = 5-7$ per group; **a**) and caspase-1 activity (FAM660 flow cytometry; **b**) in CCA 24 h after sham or stroke surgery (*U*-test, $n = 5-6$ per group). **c, d**, Analysis of macrophage proliferation normalized to total cell counts (right; *U*-test, $n = 6-7$ per group; **c**) and analysis of infiltrated leukocytes (**d**) in CCA sections of control-treated or caspase-1 inhibitor (VX765)-treated mice 7 days after stroke (*K*-test; $n = 5$ per group). Scale bars in **c**, 50 μ m. **e**, Picro Sirius red stainings for stroke (left) and quantification of plaque vulnerability (right; *U*-test; $n = 8-9$ per group). Scale bars, 50 μ m. **f, g**, Immunoblot for caspase-1 cleavage in CCA lysates 24 h after sham, stroke, stroke + NLRP3 inhibitor (MCC950) or AIM2 inhibitor (4-sulfonic calix[6]arene) administration (**f**) and corresponding immunoblot quantification (ANOVA; $n = 8$ per group; **g**). **h**, Total cfDNA serum concentrations at indicated timepoints after stroke and naive mice (*K*-test;

$n = 5-8$ per group). NS, not significant. **i, j**, Immunoblot (**i**) and quantification (**j**) of cleaved p20 caspase-1 in CCA lysates from HCD-fed *ApoE*^{-/-} mice with tandem stenosis surgery alone (control) or 24 h after i.v. DNA injection (*U*-test; $n = 7-9$ per group). **k**, Immunoblot for ASC oligomerization of WT or *Aim2*^{-/-} macrophages after stimulation with DNA. MW, molecular weight. **l**, Experimental design of *Aim2*^{WT} or *Aim2*^{-/-} bone marrow (BM) transplantation to *Ldlr*^{-/-}:*Mx1*^{cre}:*c-myc*^{fl/fl} mice receiving i.v. DNA (top) and flow cytometry histograms (bottom) of caspase-1 activity in bone marrow recipients 24 h after i.v. DNA. HF, high fat; SSC-A, side scatter area. **m, n**, Immunoblot (**m**) and quantification (**n**) of cleaved p20 caspase-1 in CCA lysates of HCD-fed *ApoE*^{-/-} with tandem stenosis surgery receiving 1,000 U i.v. DNase immediately before stroke (*U*-test; $n = 6$ per group, shown as a ratio to the mean of the control group). Raw membrane images of all immunoblots are in Supplementary Fig. 1. **a-e, g, h, j, n**. Bars indicate the mean.

marrow-reconstituted mice received a high-fat diet (HFD) for 4 weeks and were then stimulated by intravenous DNA injection to test the in vivo relevance of the specific DNA-AIM2 interaction, confirming an abrogated caspase-1 activation in AIM2-deficient monocytes/macrophages. By contrast, neutralization of cfDNA after stroke by therapeutic administration of recombinant DNase following stroke

induction again significantly reduced the plaque inflammasome activation, as measured by caspase-1 cleavage and IL-1 β secretion (Fig. 2m, n and Extended Data Fig. 7e). In summary, we identified the activation of the AIM2 inflammasome in vulnerable atherosclerotic plaques by stroke-induced DNA release and subsequent plaque rupture as the cause of recurrent ischaemic events.

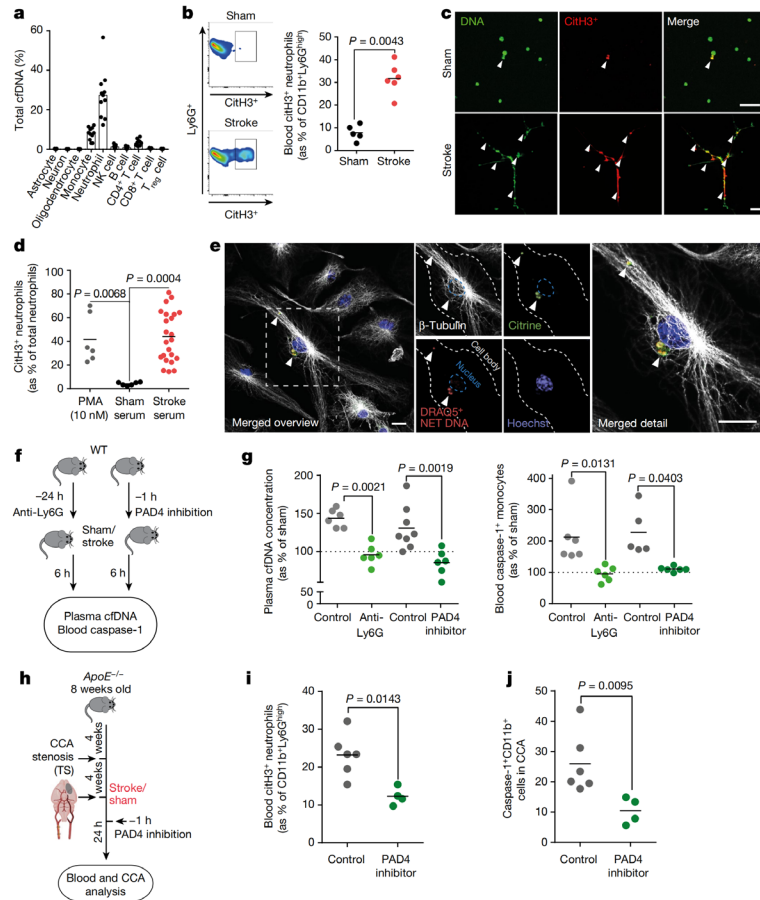


Fig. 3 | Neutrophil NETosis is the main source of post-stroke cfDNA. **a**, Tissue-of-origin analysis using cell-type-specific methylation markers for cfDNA isolated from $n = 10$ patients with stroke within 24 h after symptom onset. NK, natural killer; T_{reg} cell, regulatory T cell. **b**, Flow cytometry histograms (left) and quantification (right) of citrullinated histone 3 (citH3⁺) Ly6G⁺ neutrophils 4 h after sham or stroke (U -test; $n = 5-6$ per group). **c**, Microphotographs of mouse neutrophils stimulated with 25% sham or stroke serum for 4 h. The arrowheads indicate DNA⁺ citH3⁺ NET formations. Scale bars, 50 μ m. **d**, Quantification of phorbol 12-myristate 13-acetate (PMA)-stimulated, sham serum-stimulated or stroke serum-stimulated neutrophils, shown as citH3⁺ neutrophils of total cultured neutrophils (K -test; $n = 6-23$ replicates per group from 3 independent experiments). **e**, BMDMs from ASC-citrine reporter mice were incubated with 250 ng exogenous DRAQ5-labelled NET-DNA. Immunohistochemistry was used

to visualize cytoplasmic citrine⁺DRAQ5⁺ ASC-DNA specks. The cytoplasm and nucleus of the BMDMs were visualized using β -tubulin and Hoechst. Arrowheads indicate colocalization of ASC specks and DRAQ5⁺ NET DNA. Scale bars, 5 μ m. **f**, Experimental design for anti-Ly6G neutrophil depletion and PAD4 inhibition before stroke. **g**, cfDNA concentration (shown as percentage normalized to sham) of mice with control, anti-Ly6G or PAD4 inhibitor treatment (left; K -test; $n = 6-8$ per group) and caspase-1 activity in blood monocytes (percentage of sham, indicated by dotted line) by flow cytometry (right; K -test; $n = 5-8$ per group). **h**, NETosis was inhibited using a PAD4 inhibitor before stroke in HCD-fed $ApoE^{-/-}$ with tandem stenosis. **i**, Quantification of citH3⁺ Ly6G⁺ neutrophils 24 h after stroke surgery in blood (U -test; $n = 4-6$ per group). **j**, Flow cytometry analysis of caspase-1 activity in CD11b⁺ CCA monocytes 24 h after stroke (U -test; $n = 4-6$ per group). **b, d, g, i, j**, Bars indicate the mean.

NETosis, the main source of post-stroke DNA

To identify the cellular DNA source, we performed a methylation pattern analysis of isolated blood cfDNA from patients with stroke within the first 24 h after stroke onset, based on a previously established DNA methylation atlas of human cell types¹⁹. The main cerebral cell populations—astrocytes, neurons and oligodendrocytes—did not contribute to the increased blood cfDNA levels after stroke, which was mainly attributed to a neutrophil-specific methylome pattern and to a lesser extent to other immune cells (Fig. 3a and Extended Data Fig. 7f). To further validate this observation, we performed flow cytometric analysis of NET formation after experimental stroke in mice and identified a substantial increase in neutrophil NETosis indicated by citrullinated histone

H3-positive neutrophils (Fig. 3b); correspondingly, serum from mice after experimental stroke was sufficient to induce neutrophil NETosis of naive primary neutrophils ex vivo (Fig. 3c,d). By administration of fluorescently labelled NET-DNA to primed BMDMs from ASC-citrine reporter mice²⁰, we confirmed the effective uptake of NET-DNA and colocalization of exogenous NET-DNA with ASC specks resembling perinuclear inflammasomes (Fig. 3e). To test the contribution of neutrophil NETosis to post-stroke cfDNA in WT animals, we either depleted neutrophils by Ly6G-specific antibodies or inhibited NETosis by blocking the PAD4 molecule, which is required for NETosis (Fig. 3f and Extended Data Fig. 7g,h). Both depletion of the neutrophil population and inhibition of PAD4 efficiently prevented the post-stroke increase in blood cfDNA levels and reduced caspase-1 activation to levels in Sham-operated

control mice (Fig. 3g). Finally, we tested the efficacy of PAD4 inhibition in our animal model of rupture prone CCA plaques in APOE-deficient animals with CCA tandem stenosis and observed a similar reduction in post-stroke NETosis as in WT animals, and PAD4 inhibition efficiently reduced inflammasome activation in CCA plaques (Fig. 3h–j). Here we identified an unexpected prominent role of NETosis after stroke to the rapid increase in cfDNA levels, which represents a druggable process to reduce post-stroke systemic inflammation.

MMPs lead to plaque erosion

Conceivably, enhanced plaque inflammation—as observed here after stroke induction—could contribute to plaque rupture and secondary arterioarterial embolism resulting in secondary infarctions. However, the exact mechanisms linking plaque inflammation to plaque destabilization and atherothrombosis are poorly studied. A more detailed study of the plaque fibrous cap composition by analysing its collagen fibre orientation indicated collagen fibre disorganization after stroke, suggesting extracellular matrix (ECM) remodelling (Fig. 4a). Indeed, we found that stroke resulted in increased activity of MMPs—the main enzymes involved in ECM remodelling—which was detected by *in situ* zymography of CCA plaque sections and validated by gel zymography for MMP2 and MMP9 (Fig. 4b and Extended Data Fig. 8a,b). To test whether soluble blood mediators mediate this effect on MMP activity after stroke, we treated BMDM with serum obtained from mice 4 h after stroke or sham surgery. Conditioning of BMDMs with serum from stroke mice resulted in massively increased active MMP2 and MMP9 secretion compared with sham serum treatment, both in total protein content (western blot) and enzymatic activity (zymography), suggesting a causative role of circulating factors after stroke on MMP expression and activation in the CCA plaque (Fig. 4c and quantification in Extended Data Fig. 8c–e). Given our finding of a critical role of AIM2 inflammasome activation, we tested the influence of IL-1 β derived from inflammasome activation on MMP activity by treating BMDMs with increasing doses of recombinant IL-1 β . Indeed, we detected a dose-dependent effect of IL-1 β on MMP expression (Extended Data Fig. 8f,g). Moreover, the supernatant of NET–DNA-stimulated WT but not *Aim2*^{−/−} BMDMs was sufficient to induce MMP2 expression in naive BMDMs (Extended Data Fig. 8h–j). Next, we tested the function of IL-1 β *in vivo* by its neutralization using IL-1 β -specific antibodies in a dose that we previously established to efficiently block IL-1 β -mediated systemic effects^{18,21}. Neutralization of IL-1 β after experimental stroke significantly reduced MMP2/9 activity in CCA plaques 7 days after stroke and increased fibrous cap thickness compared with control (isotype IgG) treatment, indicating a causative role of IL-1 β in mediating inflammatory plaque degradation (Fig. 4d,e). Although MMP-mediated degradation of the extracellular matrix causes plaque destabilization²², formation of the actual thrombus on ruptured plaques depends on activation of the coagulation cascade, particularly by the contact activation pathway initiated by factor XII exposition to damaged tissue surfaces²³. We therefore performed *en face* staining of the whole CCA and compared activated factor XII deposition on the luminal surface at the area of the CCA plaque between stroke-operated or sham-operated mice. We found a significant increase in factor XIIa deposition on the plaque surface after stroke (Fig. 4f), which was confirmed by western blot analysis of whole CCA plaques (Fig. 4g and Extended Data Fig. 9a). An intravenous NET–DNA challenge without stroke mimicked the effect of stroke with increased factor XIIa deposition at the CCA plaque (Fig. 4h and Extended Data Fig. 9b). These findings suggest that the AIM2 inflammasome activation and resulting IL-1 β release after stroke could lead to plaque destabilization and atherothrombosis via activation of plaque-degrading MMPs and subsequent factor XIIa deposition. To further test this hypothesis, we performed *in vivo* MRI using time of flight (TOF)-MR angiography in combination with intravascular thrombus

imaging using a recently established magnetic matrix particle-based imaging modality²⁴. Here we were able to identify CCA occlusion 6 h after stroke induction, which coincided with intravascular thrombi formation in the affected distal MCA segments (Fig. 4i). Correspondingly, *in vivo* inflammasome inhibition using the caspase-1 inhibitor VX765 significantly reduced plaque MMP activity and luminal factor XIIa deposition (Fig. 4j,k and Extended Data Fig. 9c). Similarly, intravenous DNase treatment significantly reduced MMP activity and factor XIIa deposition (Fig. 4l and Extended Data Fig. 9d).

DNase reduces stroke recurrence

Finally, we analysed whether blocking DNA-mediated inflammasome activation after stroke could be used therapeutically to prevent recurrent ischaemic events. For this, mice with CCA tandem stenosis were treated with the caspase-1 inhibitor VX765 or recombinant DNase. The occurrence of secondary ischaemic lesions was analysed 7 days after induction of the primary stroke and in the hemisphere contralateral to the primary stroke, that is, within the territory supplied by the stenotic CCA. Indeed, both caspase-1 inhibition and DNase treatment greatly and significantly reduced the recurrence rate (Fig. 4m). Of note, this therapeutic effect was achieved in a large sample size of animals (total sample size of 117 mice) and translates to a relative risk reduction of 82% and 75% for VX765 and DNase, respectively.

Validation in patients with stroke

To further validate the translational relevance of the identified mechanisms, we obtained carotid endarterectomy samples from highly stenotic carotid artery plaques of asymptomatic patients and patients during the acute phase of ischaemic stroke (Fig. 5a). Flow cytometry analysis of the plaque material revealed a significant increase in monocyte counts in plaques from symptomatic compared with asymptomatic patients (Fig. 5b), whereas blood monocyte and lymphocyte counts did not differ (Extended Data Fig. 10a–c). Correspondingly, we found a significant increase in circulating cfDNA in plasma of patients with stroke, as well as a substantial increase in markers of inflammasome priming (pro-caspase-1 expression) and inflammasome activation (cleaved p20 isoform of caspase-1) in plaque material (Fig. 5c–f). We observed a similar increase in cfDNA in patients after myocardial infarction, emphasizing again the generalizability of our findings across ischaemic organ damage (Fig. 5g). Of note, we also detected a more than tenfold increase in MMP9 activity by gel zymography of plaques from symptomatic compared with asymptomatic patients (Fig. 5h and Extended Data Fig. 10d,e). Finally, the amount of plaque-associated factor XIIa was significantly increased in atherosclerotic plaques after stroke (Fig. 5i). Hence, the analyses of human endarterectomy samples confirmed all key steps of DNA-mediated inflammasome activation, vascular inflammation, MMP activation and initiation of thrombus formation in patients with stroke as identified in our animal model.

Discussion

Early recurrent events after ischaemic stroke present a pressing socio-medical problem with an unmet need. Current secondary prevention therapies target mainly blood lipid levels (statins) and platelet aggregation (aspirin), which are effective for long-term prevention of vascular events. However, these therapies have overall an only minor effect recurrence after large-artery stroke², most likely because this is driven by so far largely unknown immunological mechanisms¹¹. Here we identified inflammasome activation by cfDNA as an initiator of an inflammatory cascade leading to atherosclerotic plaque degradation and thrombosis (Extended Data Fig. 10f). Furthermore, we detected neutrophil NETosis as the unexpected major source of post-stroke cfDNA. Our results propose the inhibition of NETosis, the

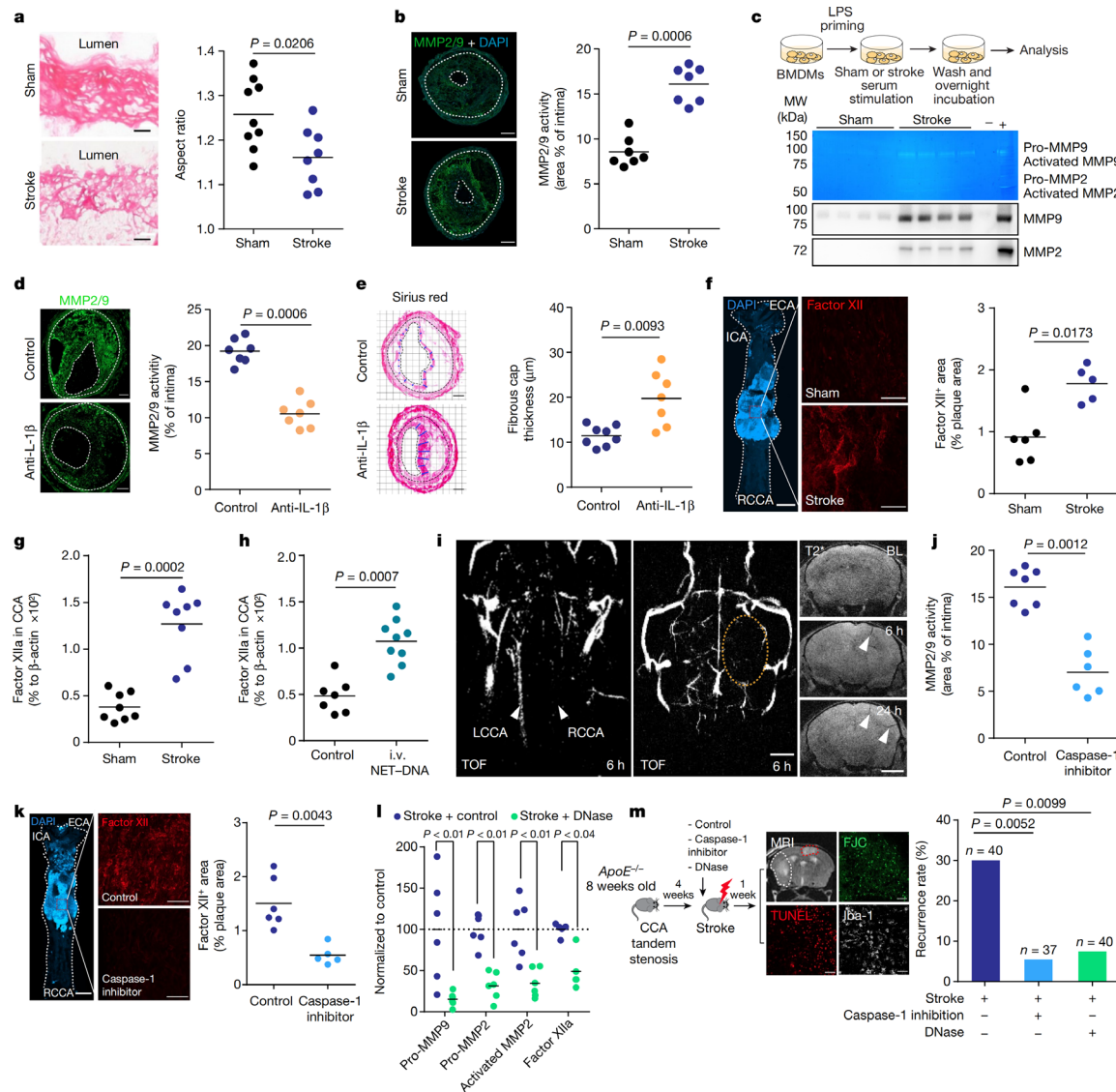


Fig. 4 | Inhibition of post-stroke inflammasome activation prevents plaque destabilization and recurrent stroke events. **a**, Collagen I orientation in fibrous caps using aspect ratio (AR > 1 is predominant orientation and AR < 1 is random orientation; *U*-test; *n* = 8–9). Scale bars, 50 μ m. **b**, Quantification of MMP2/9 activity by in situ zymography on CCA sections 7 days after sham or stroke (*U*-test; *n* = 7). Scale bars, 50 μ m. **c**, Experimental design (top), representative images (middle) for gelatin zymography and immunoblot (bottom) of MMP2/9 in culture medium (quantification in Extended Data Fig. 8c,d). **d**, In situ zymography of CCA sections 7 days after stroke, receiving control or IL-1 β -specific antibodies (*U*-test; *n* = 7). Scale bars, 50 μ m. **e**, Analysis of fibrous cap thickness between treatment groups (*U*-test; *n* = 7–8). Scale bars, 50 μ m. **f**, Whole CCA en face immunohistology for factor XII 24 h after sham or stroke (*U*-test; *n* = 5–6). ECA, external carotid artery; ICA, internal carotid artery; RCCA, right CCA. Scale bars, 500 μ m. **g**, Activated factor XII in CCA lysates 7 days after sham or stroke (*U*-test; *n* = 8). **h**, Factor XIIa in CCA lysates 24 h after

i.v. DNA injection (*U*-test; *n* = 7–9). **i**, HCD-fed *ApoE*^{-/-} with tandem stenosis surgery received i.v. DNA. Cerebral vascularization (TOF-MR angiography) and intravascular thrombus formation by in vivo MRI in HCD-fed *ApoE*^{-/-}. Left CCA (LCCA) and (patent) right CCA (RCCA) are indicated by arrowheads (left); the orange dotted circle (middle panel) denotes the hypoperfused right middle cerebral artery territory. The arrowheads (right) indicate intravascular thrombi. Scale bars, 2 mm. BL, baseline. **j**, In situ zymography for MMP2/9 activity in CCA sections 7 days after stroke (*U*-test; *n* = 6–7). **k**, Factor XII⁺ area on CCA en face images between treatment groups (*U*-test; *n* = 5–6). Scale bars, 500 μ m. **l**, Pro-MMP9, pro-MMP2, activated MMP2 and factor XIIa quantification in mice receiving 1,000 U DNase after stroke (*U*-test; *n* = 6, normalized to control, indicated by horizontal dotted line). **m**, Experimental design (left) and quantification of the 7-day recurrence rate between treatment groups (right; chi-squared test). Scale bars, 50 μ m. **a**, **b**, **d**–**h**, **j**–**l**, Bars indicate the mean.

neutralization of cfDNA or inhibition of downstream inflammasome activation as efficient therapeutic approaches to prevent recurrent vascular events.

The CANTOS trial—testing the use of IL-1 β -specific antibody treatment in patients with previous myocardial infarction—has clearly highlighted the relevance of residual inflammatory risk and demonstrated

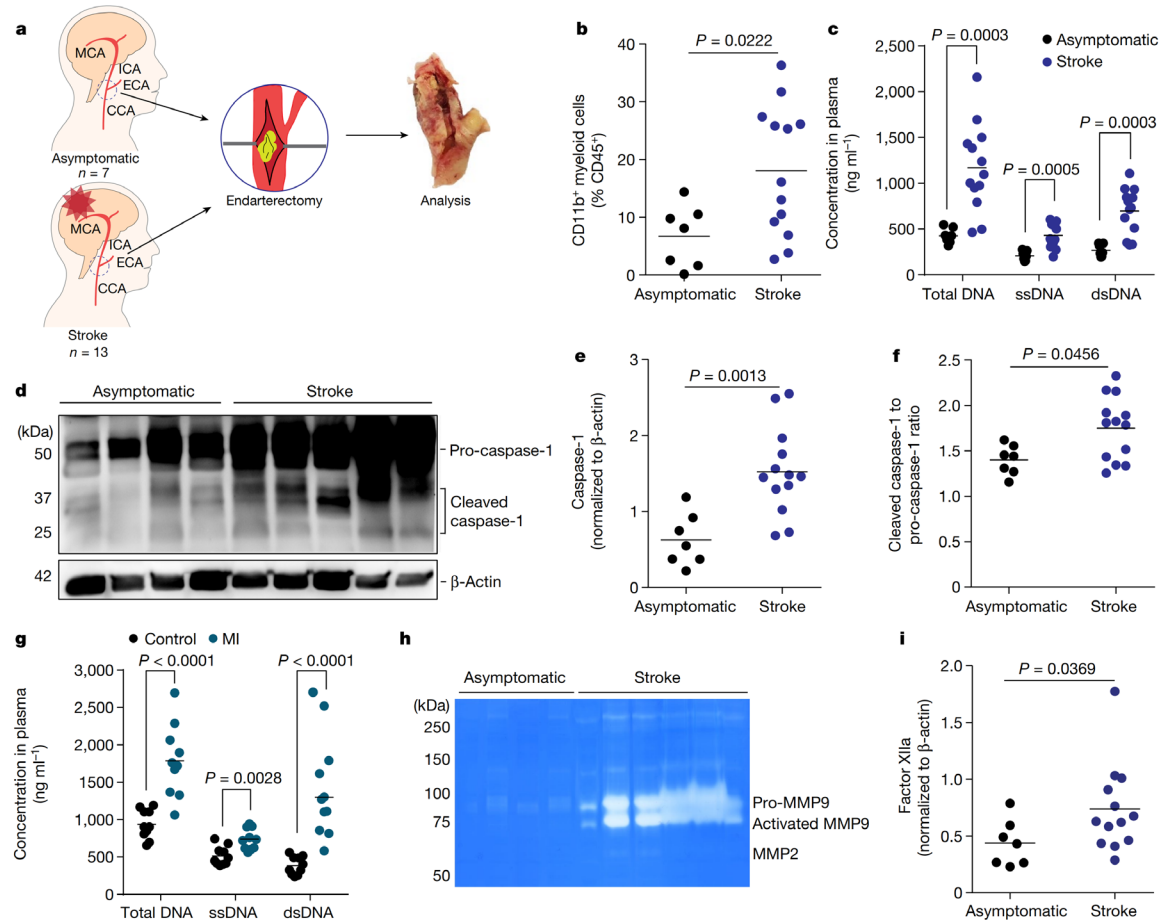


Fig. 5 | Stroke increases atherosclerotic plaque inflammation and MMP activity in patients. **a**, Study layout illustrating the collection of endarterectomy samples from 7 asymptomatic patients with ICA stenosis and 13 patients with stroke undergoing endarterectomy of the symptomatic carotid artery in the acute phase after stroke. **b**, Flow cytometry analysis of plaques showing the percentage of CD11b⁺ myeloid cells out of total leukocytes (CD45⁺; U -test; $n = 7$ –13 per group). **c**, Quantification of total cfDNA (total DNA), single-stranded DNA (ssDNA) and double-stranded DNA (dsDNA) in plasma (U -test; $n = 7$ –13 per group). **d**–**f**, Immunoblot for caspase-1 cleavage in atherosclerotic plaque

lysates of asymptomatic or symptomatic patients (**d**) and corresponding quantification of total caspase-1 (**e**, normalized to β -actin) and cleaved p20 caspase-1 (**f**, normalized to caspase-1; U -test; $n = 7$ –13 per group). **g**, Plasma cfDNA concentrations in patients with myocardial infarction (U -test; $n = 10$ per group). **h**, Gelatin zymography of plaque lysates from asymptomatic or symptomatic patients (quantification in Extended Data Fig. 10e). **i**, Factor XIIa in plaque lysates from asymptomatic or symptomatic patients (U -test; $n = 7$ –13 per group). **b**, **c**, **e**–**g**, **i**, Bars indicate the mean.

the potential of anti-inflammatory therapies to prevent recurrent ischaemic events²⁵. However, targeting this central cytokine of innate immune defence also significantly increased the risk of fatal infections, which might preclude further clinical development of such unspecific anti-inflammatory strategies²⁶. A critical limitation of previous clinical trials targeting inflammatory mechanisms in high-risk patients with atherosclerosis was the insufficient mechanistic knowledge on the exact immunological events that resulted in recurrent vascular events. This knowledge gap has so far prevented the development of more specific, and thereby safer, therapeutic strategies targeting molecular mechanisms of stroke recurrence.

Here we identified increased circulating NET–DNA concentrations and activation of the AIM2 inflammasome as the key mechanisms leading to exacerbated plaque inflammasome activation, whereas other inflammasomes or redundant inflammatory mechanisms could additionally contribute to this phenomenon. We demonstrated that the

increase in circulating cfDNA was sufficient and causally involved in plaque destabilization using an *in vivo* cfDNA-challenge experiment and validated in human patient samples. In addition, cfDNA was sufficient to induce CCA occlusion and intravascular thrombi in downstream vascular territories as observed by *in vivo* MRI and histological analysis. Correspondingly, use of recombinant DNase efficiently prevented plaque inflammation, destabilization and recurrent ischaemic events. No direct immunosuppressive function is known for the experimental or clinical use of DNase in various disease conditions including cystic fibrosis and pleural infections^{27–29}. By contrast, we have previously demonstrated that prevention of AIM2 inflammasome activation by DNase treatment might even paradoxically improve immunocompetence during secondary bacterial infections, because reduction of early inflammasome activation in response to tissue injury prevents subacute immunosuppression^{18,30}. Of note, lower endogenous DNase activity has recently been described as an independent risk factor

for stroke-associated infections following severe ischaemic stroke³¹. Therefore, the use of DNase is a promising candidate for further clinical development as a therapeutic approach in early secondary prevention that is highly efficient but also safe due to its specific and non-immunosuppressive function. Hence, we have initiated a clinical proof-of-concept trial that will test the efficacy of DNase treatment for the prevention of systemic inflammation in patients with stroke (ReScinD trial; ClinicalTrials.gov ID: NCT05880524). Of note, although DNase I proved to be highly efficient to prevent cfDNA-mediated vascular inflammation, we cannot exclude (synergistic) efficacy of other nucleases to prevent AIM2 inflammasome activation.

Not only the immunogenic mediators leading to inflammatory plaque rupture but also the exact pathways contributing to local plaque destabilization and recurrent atherothrombosis after stroke were so far elusive. Here we focused on the role of MMP-mediated plaque degradation and subsequent initiation of the contact-dependent coagulation cascade. In correspondence with our observations, increased plaque MMP activity has been previously associated with markers of increased plaque vulnerability²². In addition, increased blood MMP9 activity has been previously associated with worse stroke outcome³². We observed that inflammasome activation and specifically the release of local IL-1 β can dose-dependently increase MMP activity. Moreover, we demonstrated that neutralization of systemic IL-1 β prevents MMP activation and plaque degradation after stroke. It is likely that MMP-mediated degradation of the plaque ECM leads to destabilization and exposition of ECM components to the blood circulation³³. Correspondingly, we found inflammasome-dependent luminal accumulation of factor XIIa at the CCA plaque—a process that we found to be associated with the occurrence of secondary infarctions. Factor XII activation at the site of vascular damage has been previously proposed as an initiator mechanism of thrombus formation on ruptured plaques, and its pharmacological targeting has recently been demonstrated to stabilize atherosclerotic plaques³⁴. Therefore, on the basis of our findings, factor XIIa might represent another potential therapeutic target to prevent recurrent ischaemic events and warrants further exploration.

In summary, in this study, we present a mechanistic explanation for the high rate of early recurrent events after stroke and myocardial infarction in patients with atherosclerosis. Using a novel animal model of post-stroke plaque rupture and secondary infarctions, we identified the immunological mechanisms and validated these in human carotid artery plaque samples. We confirmed the efficient therapeutic targeting of this signalling cascade with DNase administration as a promising therapeutic candidate for further clinical translation.

Online content

Any methods, additional references, Nature Portfolio reporting summaries, source data, extended data, supplementary information, acknowledgements, peer review information; details of author contributions and competing interests; and statements of data and code availability are available at <https://doi.org/10.1038/s41586-024-07803-4>.

- Mohan, K. M. et al. Risk and cumulative risk of stroke recurrence: a systematic review and meta-analysis. *Stroke* **42**, 1489–1494 (2011).
- Touze, E. et al. Risk of myocardial infarction and vascular death after transient ischaemic attack and ischemic stroke: a systematic review and meta-analysis. *Stroke* **36**, 2748–2755 (2005).
- World Health Organization. The top 10 causes of death. *WHO* <https://www.who.int/news-room/fact-sheets/detail/the-top-10-causes-of-death> (2020).
- Katan, M. & Luft, A. Global burden of stroke. *Semin. Neurol.* **38**, 208–211 (2018).
- Boulanger, M., Bejot, Y., Rothwell, P. M. & Touze, E. Long-term risk of myocardial infarction compared to recurrent stroke after transient ischaemic attack and ischemic stroke: systematic review and meta-analysis. *J. Am. Heart Assoc.* **7**, e007267 (2018).
- Lovett, J. K., Coull, A. J. & Rothwell, P. M. Early risk of recurrence by subtype of ischemic stroke in population-based incidence studies. *Neurology* **62**, 569–573 (2004).
- Libby, P. The changing landscape of atherosclerosis. *Nature* **592**, 524–533 (2021).
- Roth, S. et al. Brain-released alarmins and stress response synergize in accelerating atherosclerosis progression after stroke. *Sci. Transl. Med.* **10**, eaa01313 (2018).
- Dutta, P. et al. Myocardial infarction accelerates atherosclerosis. *Nature* **487**, 325–329 (2012).

- Liesz, A. et al. DAMP signaling is a key pathway inducing immune modulation after brain injury. *J. Neurosci.* **35**, 583–598 (2015).
- Kelly, P. J. et al. Anti-inflammatory approaches to ischaemic stroke prevention. *J. Neurol. Neurosurg. Psychiatry* **89**, 211–218 (2018).
- Schlager, O. et al. C-reactive protein predicts future cardiovascular events in patients with carotid stenosis. *Stroke* **38**, 1263–1268 (2007).
- Georgakis, M. K. et al. Cerebral small vessel disease burden and cognitive and functional outcomes after stroke: a multicenter prospective cohort study. *Alzheimers Dement.* <https://doi.org/10.1002/alz.12744> (2022).
- Liman, T. G. et al. Prediction of vascular risk after stroke — protocol and pilot data of the Prospective Cohort with Incident Stroke (PROSCIS). *Int. J. Stroke* **8**, 484–490 (2013).
- Silvestre-Roig, C. et al. Externalized histone H4 orchestrates chronic inflammation by inducing lytic cell death. *Nature* **569**, 236–240 (2019).
- Green, J. P. et al. Discovery of an inhibitor of DNA-driven inflammation that preferentially targets the AIM2 inflammasome. *iScience* **26**, 106758 (2023).
- Paulin, N. et al. Double-strand DNA sensing Aim2 inflammasome regulates atherosclerotic plaque vulnerability. *Circulation* **138**, 321–323 (2018).
- Roth, S. et al. Post-injury immunosuppression and secondary infections are caused by an AIM2 inflammasome-driven signaling cascade. *Immunity* **54**, 648–659.e8 (2021).
- Loyfer, N. et al. A DNA methylation atlas of normal human cell types. *Nature* **613**, 355–364 (2023).
- Tzeng, T. C. et al. A fluorescent reporter mouse for inflammasome assembly demonstrates an important role for cell-bound and free ASC specks during in vivo infection. *Cell Rep.* **16**, 571–582 (2016).
- Roth, S., Yang, J., Cramer, J. V., Malik, R. & Liesz, A. Detection of cytokine-induced sickness behavior after ischemic stroke by an optimized behavioral assessment battery. *Brain Behav. Immun.* **91**, 668–672 (2021).
- Johnson, J. L. et al. Suppression of atherosclerotic plaque progression and instability by tissue inhibitor of metalloproteinase-2: involvement of macrophage migration and apoptosis. *Circulation* **113**, 2435–2444 (2006).
- Renne, T., Schmaier, A. H., Nickel, K. F., Blomback, M. & Maas, C. In vivo roles of factor XII. *Blood* **120**, 4296–4303 (2012).
- Martinez de Lizarondo, S. et al. Tracking the immune response by MRI using biodegradable and ultrasensitive microprobes. *Sci. Adv.* **8**, eabm3596 (2022).
- Ridker, P. M. et al. Antiinflammatory therapy with canakinumab for atherosclerotic disease. *N. Engl. J. Med.* **377**, 1119–1131 (2017).
- Liberale, L., Montecucco, F., Schwarz, L., Luscher, T. F. & Camici, G. G. Inflammation and cardiovascular diseases: lessons from seminal clinical trials. *Cardiovasc. Res.* **117**, 411–422 (2021).
- Yang, C. & Montgomery, M. Dornase alfa for cystic fibrosis. *Cochrane Database Syst. Rev.* **3**, CD001127 (2021).
- Davis, J. C. Jr. et al. Recombinant human DNase I (rhDNase) in patients with lupus nephritis. *Lupus* **8**, 68–76 (1999).
- Rahman, N. M. et al. Intraleural use of tissue plasminogen activator and DNase in pleural infection. *N. Engl. J. Med.* **365**, 518–526 (2011).
- Simats, A. & Liesz, A. Systemic inflammation after stroke: implications for post-stroke comorbidities. *EMBO Mol. Med.* **14**, e16269 (2022).
- Grosse, G. M. et al. Endogenous deoxyribonuclease activity and cell-free deoxyribonucleic acid in acute ischemic stroke: a cohort study. *Stroke* **53**, 1235–1244 (2022).
- Zhong, C. et al. Serum matrix metalloproteinase-9 levels and prognosis of acute ischemic stroke. *Neurology* **89**, 805–812 (2017).
- Rekhter, M. D. et al. Hypercholesterolemia causes mechanical weakening of rabbit atheroma: local collagen loss as a prerequisite of plaque rupture. *Circ. Res.* **86**, 101–108 (2000).
- Searle, A. K. et al. Pharmacological inhibition of factor XIIa attenuates abdominal aortic aneurysm, reduces atherosclerosis, and stabilizes atherosclerotic plaques. *Thromb. Haemost.* **122**, 196–207 (2022).

Publisher's note Springer Nature remains neutral with regard to jurisdictional claims in published maps and institutional affiliations.



Open Access This article is licensed under a Creative Commons Attribution-NonCommercial-NoDerivatives 4.0 International License, which permits any non-commercial use, sharing, distribution and reproduction in any medium or format, as long as you give appropriate credit to the original author(s) and the source, provide a link to the Creative Commons licence, and indicate if you modified the licensed material. You do not have permission under this licence to share adapted material derived from this article or parts of it. The images or other third party material in this article are included in the article's Creative Commons licence, unless indicated otherwise in a credit line to the material. If material is not included in the article's Creative Commons licence and your intended use is not permitted by statutory regulation or exceeds the permitted use, you will need to obtain permission directly from the copyright holder. To view a copy of this licence, visit <http://creativecommons.org/licenses/by-nc-nd/4.0/>.

© The Author(s) 2024

DEMDAS Study Group

Martin Dichgans¹⁹, Matthias Endres¹⁹, Marios K. Georgakis¹, Thomas G. Liman¹⁹, Gabor Petzold¹⁹, Annika Spottke¹⁹, Silke Wunderlich²⁰ & Inga Zerr²¹

¹⁹German Center for Neurodegenerative Diseases (DZNE), Berlin, Germany. ²⁰German Center for Neurodegenerative Diseases (DZNE), Bonn, Germany. ²¹Department of Neurology, Klinikum rechts der Isar, School of Medicine, Technical University of Munich, Munich, Germany.

²¹German Center for Neurodegenerative Diseases (DZNE), Göttingen, Germany.

Methods

All consumables, such as antibodies, chemicals and so on can, be found in the resource list in Supplementary Table 6.

Animal experiments

All animal experiments were performed in accordance with the guidelines for the use of experimental animals and were approved by the government committee of Upper Bavaria (Regierungspraesidium Oberbayern; #02-2018-12). All mice used in this study were between 6 and 16 weeks of age independent of genotype and experimental setup. *ApoE*^{-/-} (B6.129P2-Apoe^{tm1Unz}/J; JAX strain: 002052), WT (C57BL/6J; JAX strain: 000664), *Aim2*^{-/-} (B6.129P2-Aim2^{Gt(CSG445)Byg}/J; JAX strain: 013144), *Pycard*^{-/-} (*Asc*^{-/-}; B6.129S5-Pycard^{tm1Vmd}) and R26-CAG-ASC-citrine (B6.Cg-Gt(ROSA)26or^{tm1.1(CAG-Pycard/mCitrine⁺,CD2⁺)}; JAX strain: 030744) mice were bred and housed at the animal core facility of the Centre for Stroke and Dementia Research (Munich, Germany). *Ldlr*^{-/-}:*Mx1*^{cre}:*c-Myb*^{fl/fl} mice were bred and housed at the animal facility of Walter Brendel Centre (Munich, Germany). *ApoE*^{-/-} mice were fed an HFD (#88137, ssniff) from 8 weeks onwards. *cGas*^{-/-} (B6(C)-*cGas*^{tm1d(EUCOMM)Himgu}/J), *Nlrp1*^{-/-} (Del(*11Nlrp1a-Nlrp1c-ps*)^{ISmas}) and *Nlrp3*^{-/-} (C57BL/6J-*NLRP3*^{tm1Tsc}) mice were bred and housed at the Gene Centre of the LMU University Munich (Germany).

For this exploratory study, animal numbers were estimated based on previous results from the transient ischaemia–reperfusion stroke model on extent and variability of atheroprotection after stroke. Data were excluded from all mice that died during surgery. Detailed exclusion criteria are described below. Animals were randomly assigned to treatment groups, and all analyses were performed by investigators blinded to group allocation. All animal experiments were performed and reported in accordance with the Animal Research: Reporting of In Vivo Experiments (ARRIVE) guidelines³⁵.

Drug administrations

Oral gavage with aspirin and rosuvastatin. Mice received a daily bolus of aspirin (20 mg kg⁻¹, Sigma Aldrich) and rosuvastatin (5 mg kg⁻¹, Sigma-Aldrich) via oral gavage. Aspirin and rosuvastatin were solved in water (sterile ddH₂O) and mixed with a powdered chow diet (ssniff). A single daily bolus was 500 µl.

Recombinant human DNase I. *ApoE*^{-/-} mice received DNase injections as we previously described¹⁸. In brief, 1,000 U recombinant DNase I (Roche) dissolved in incubation 1× buffer (40 mM Tris-HCl, 10 mM NaCl, 6 mM MgCl₂ and 1 mM CaCl₂, pH 7.9, diluted in PBS; Roche) was injected intravenously via tail vein right before surgery in a final volume of 100 µl. The control group was administered saline injections at the same volume, routine and timing as the experimental group.

Caspase-1 inhibitor (VX765). The caspase-1 inhibitor VX765 (stock in DMSO) was dissolved in PBS (Belnacasan, Invivogen) and injected intraperitoneally 1 h before surgery at a dose of 100 mg kg⁻¹ body weight at a final volume of 300 µl (ref. 18). The control group was administered saline injections at the same volume, routine and timing as the experimental group.

NLRP3 inflammasome inhibitor (MCC950). Mice received two injections (1 h before and 1 h after surgery) of the NLRP3 inflammasome inhibitor MCC950 dissolved in sterile saline at a dose of 50 mg kg⁻¹ body weight (Invivogen). MCC950 or the control (sterile saline) was injected intraperitoneally in a final volume of 200 µl.

AIM2 inhibitor (4-sulfonic calixarene). The AIM2 inhibitor 4-sulfonic calixarene has recently been characterized by Green et al.³⁶. The stock solutions (in DMSO) were dissolved in PBS and injected intraperitoneally 1 h before surgery at a dose of 5 mg kg⁻¹ body weight at a final

volume of 200 µl. The control group was administered control injections (sterile saline) at the same volume, routine and timing as for the intervention group.

DNA challenge. DNA derived from stimulated neutrophils (see below for neutrophil stimulation and isolation of NET–DNA) was injected intravenously at a dose of 5 µg at a final volume of 200 µl (sterile saline). The control group was administered control injections (sterile saline) at the same volume, routine and timing as for the intervention group.

Neutrophil depletion. Neutrophils were depleted using a specific antibody to Ly6G (clone: 1A8, BioXCell). Mice were administered at a concentration of 14 mg kg⁻¹ body weight at a final volume of 250 µl intraperitoneally. The control group was administered control IgG injections at the same volume, routine and timing as the experimental group.

PAD4 inhibitor (GSK484). The PAD4 inhibitor GSK484 (stock in 100% EtOH) was diluted in PBS to a final concentration of 4 mg kg⁻¹ body weight at a final volume of 100 µl. GSK484 was administered 1 h before surgery. For more than 6 h of survival time, a second bolus (4 mg kg⁻¹ body weight) was injected intraperitoneally 4 h post-surgery. The control group was administered control injections (sterile saline) at the same volume, routine and timing.

IL-1β neutralization. Mice received two injections of antagonizing anti-IL-1β in sterile saline (clone: B122, BioXCell), 1 h before and 1 h after surgery. Anti-IL-1β or the corresponding IgG control was injected intraperitoneally at a dose of 4 mg kg⁻¹ body weight in a final volume of 200 µl.

Patient cohorts for epidemiological analysis

The analysis presented in Fig. 1a was performed using patient data from two multicentre prospective observational hospital-based cohort studies of patients with acute ischaemic stroke in Germany (PROSCIS and DEMDAS/DEDEMAs). All patients provided written informed consent. Patient characteristics are provided in Supplementary Table 1. The study protocols and the detailed baseline patient characteristics have been previously described^{13,14}. Basic demographic and stroke-related characteristics are summarized below. In brief, for both the PROSCIS and the DEMDAS/DEDEMAs cohorts, patients 18 years of age or older with an acute ischaemic stroke confirmed with neuroimaging and with symptom onset in the past 7 and 5 days, respectively, were recruited through the local stroke units of seven tertiary stroke centres in Germany. Patients in PROSCIS underwent follow-up telephone interviews at 3 and 12 months after stroke, whereas patients in DEMDAS/DEDEMAs underwent a telephone interview at 3 months after stroke as well as face-to-face interviews and inspection of their medical records by a physician at 6 and 12 months after stroke. The outcome of interest for the current analysis included the occurrence of a recurrent ischaemic stroke or transient ischaemic attack within the first 12 months after stroke, as self-reported by the patient and documented in their medical records.

Patient cohort for carotid endarterectomy sample analysis

Patients scheduled for carotid endarterectomy due to symptomatic or asymptomatic carotid stenosis were prospectively recruited at the Department of Neurology and Cardiothoracic Transplantation and Vascular Surgery at Hannover Medical School between June 2018 and December 2020. Patients characteristics are provided in Supplementary Table 2. Carotid stenosis was defined as symptomatic if cerebral ischaemia occurred in the territory of the affected artery, and concurrent stroke aetiologies were excluded following standardized stroke diagnostics including cranial computed tomography

and/or MRI, computed tomography or MR-angiography, transthoracic or transoesophageal echocardiography, cardiac rhythm monitoring and Doppler/duplex ultrasound. Peripheral venous blood was drawn immediately before surgery, and EDTA whole-blood samples were used for flow cytometry analysis. Carotid plaque samples were obtained during carotid endarterectomy and immediately preserved in PBS. Both blood and tissue samples were sent for further analysis on the same day of collection. All patients provided written informed consent and the ethics committee at Hannover Medical School approved the study.

Thirteen patients with symptomatic and seven patients with asymptomatic, high-grade carotid stenosis were recruited. The median age was 73 years (25th–75th percentile: 62–80 years of age). See Supplementary Table 2 for clinical and demographic patient details.

Patient cohort for myocardial infarction sample analysis

Patients with ST-elevation myocardial infarction (STEMI) were prospectively recruited between September 2016 and February 2018 at the German Heart Centre Munich and the Klinikum rechts der Isar (both at the Technical University of Munich). Patients characteristics are provided in Supplementary Table 3.

The diagnosis of STEMI was based on chest pain within the past 12 h, persistent ST-segment elevation of 1 mm or more in at least two extremities or 2 mm or more in at least two chest leads and diagnosis of type 1 myocardial infarction according to cardiac catheterization. Exclusion criteria were: cardiogenic shock, left ventricle ejection fraction of 35 or less, coexisting chronic or inflammatory diseases, anti-inflammatory drug therapy (for example, cortisol) and myocardial infarction type 2–5. Blood samples for plasma analysis were collected in EDTA tubes immediately after admission to the hospital or latest 6 h after coronary intervention.

Age-matched and sex-matched patients with known stable coronary artery disease served as controls. They were prospectively recruited between February 2017 and February 2018 during consultation in the outpatient department of the German Heart Centre Munich for routine examination. Exclusion criteria were: history of myocardial infarction, reduced left ventricle ejection fraction, chronic or inflammatory diseases, and anti-inflammatory drug therapy. Blood samples for plasma analysis were collected in EDTA tubes on the day of consultation in the outpatient department. All patients provided written informed consent and the institutional ethics committee at Technical University Munich approved the study (235/16S). EDTA tubes of both STEMI and control patients were centrifuged at 4 °C and 1,600g for 30 min directly after collection. Plasma aliquots were stored at –80 °C for further analysis.

Carotid tandem stenosis model

Tandem stenosis surgery was performed as previously described³⁷. In brief, at 12 weeks of age, 4 weeks after commencement of an HFD, *ApoE*^{–/–} mice (C57BL/6J background) were anaesthetized with 2% isoflurane delivered in a mixture of 30% and 70% N₂O. An incision was made in the neck, and the right common carotid artery was dissected from circumferential connective tissues. To control the stenosis diameter, a 150-µm or 450-µm dummy was placed on top of the exposed right common carotid artery, with the distal point 1 mm away from the bifurcation and proximal point 3 mm from the distal stenosis; subsequently, a 6-0-braided polyester fibre suture was tied around both the artery and the needle, and then the pin was carefully removed. Animals were fed with an HFD for an additional 4 weeks after tandem stenosis surgery.

Bone marrow transplantation

Donor animals (B6.129P2-*Aim2*^{Gt(CSG445)Byg/J} or C57BL/6J) were euthanized and the femur, tibia and humerus were collected in cold PBS. Bone marrows were isolated from bones and filtered through 40-µm

cell strainers to obtain single-cell suspensions. After washing, cell number and viability were assessed using an automated cell counter (Countess 3, Thermo Fisher Scientific) and Trypan Blue solution (Merck). Cells were injected intravenously into *Mx1*^{Cre}:*c-Myb*^{fl/fl} recipient mice (*Ldlr*^{–/–} background; 8–15 × 10⁶ cells per mouse) in a total volume of 100 µl saline. At the time of transplantation, recipient mice had previously been treated with poly(I:C) solution at a dose of 10 µg g^{–1} body weight every other day five times to induce bone marrow depletion³⁸. Mice were fed with a HFD and maintained for 4 weeks after transplantation to establish efficient bone marrow repopulation.

Ischaemia–reperfusion stroke model

Four weeks after tandem stenosis surgery, *ApoE*^{–/–} mice were anaesthetized with 2% isoflurane delivered in a mixture of 30% O₂ and 70% N₂O. An incision was made between the ear and the eye to expose the temporal bone. Mice were placed in supine position, and a laser Doppler probe was attached to the skull above the middle cerebral artery (MCA) territory. The common carotid artery and left external carotid artery were exposed via middle incision and further isolated and ligated. A 2-mm silicon-coated filament (Doccol) was inserted into the internal carotid artery, advanced gently to the MCA until resistance was felt, and occlusion was confirmed by a corresponding decrease in blood flow (that is, a decrease in the laser Doppler flow signal by 80% or more). After 60 min of occlusion, the animals were re-anaesthetized and the filament was removed. After recovery, the mice were kept in their home cage with ad libitum access to water and food. Sham-operated mice received the same surgical procedure, but the filament was removed in lieu of being advanced to the MCA. Body temperature was maintained at 37 °C throughout surgery in all mice via feedback-controlled heating pad. Exclusion criteria included: (1) insufficient MCA occlusion (a reduction in blood flow to more than 20% of the baseline value), (2) death during the surgery, and (3) lack of brain ischaemia as quantified post-mortem by histological analysis.

Myocardial infarction

Myocardial infarction surgery was performed as previously described³⁹. In brief, mice were intubated under MMF anaesthesia (midazolam 5.0 mg kg^{–1} body weight, medetomidine hydrochloride 1.0 mg kg^{–1} body weight and fentanyl citrate 0.05 mg kg^{–1} body weight; intraperitoneally) and thoracotomy was performed in the left intercostal space. The left anterior descending coronary artery was identified and myocardial infarction was induced by permanent ligation with an 8-0 prolene suture. Atipamezole hydrochloride (5 mg kg^{–1} body weight) and flumazenil (0.1 mg kg^{–1} body weight) injected subcutaneously were used to antagonize MMF anaesthesia. Mice received subcutaneous buprenorphine (0.3 mg kg^{–1} body weight) as an analgesic every 8 h for 3 days starting at the end of the surgical procedure.

Ultrasound imaging (mouse carotid artery Doppler analysis)

Carotid artery blood flow in *ApoE*^{–/–} mice was measured with a high-frequency ultrasound imaging system (Vevo 3100LT, Visual Sonics) with a 40-MHz linear array transducer (MX550D, Visual Sonics) before and right after tandem stenosis surgery, and weekly for 4 weeks afterwards. Mice were anaesthetized with isoflurane delivered in a mixture of 30% O₂ and 70% N₂O. B-mode, colour-Doppler mode and pulsed Doppler velocity spectrum were recorded from both sides of the CCA. For the right CCA (RCCA), five locations were examined: before proximal ligation, near proximal ligation, between two ligations, near distal ligation and above the distal ligations. For the left CCA (LCCA), as it was not ligated, only three locations were measured: proximal, middle and distal part of the LCCA. Pulsed Doppler velocity was determined with the sample volume calibrated to cover the entire vascular lumen and the smallest possible angle of interception (less than 60°) between the flow direction and the ultrasound beam. The peak systolic velocity (PSV) and end diastolic velocity (EDV) were recorded from CCAs of both sides.

VevoLab v3.2.0 software was used for ultrasound imaging analysis. The mean velocity was calculated as: mean velocity = (PSV + 2 × EDV)/3.

MRI for secondary lesion detection

MRI was performed in a small-animal scanner (3T nanoScan PET/MR, Mediso, with 25-mm internal diameter quadrature mouse head coil) at 2 and 7 days after sham or stroke surgery. For scanning, mice were anaesthetized with 1.2% isoflurane in 30% O₂//70% N₂O applied via face mask. Respiratory rate and body temperature (37 ± 0.5 °C) were continuously monitored via an abdominal pressure-sensitive pad and rectal probe, and anaesthesia was adjusted to keep them in a physiological range. The following sequences were obtained: coronal T2-weighted imaging (2D fast-spin echo (FSE), repetition time/echo time (TR/TE) = 3,000/57.1 ms, averages 14, resolution 167 × 100 × 500 μm³), coronal T1-weighted imaging (2D FSE, TR/TE = 610/28.6 ms, averages 14, resolution 167 × 100 × 500 μm³) and diffusion-weighted imaging (2D spin echo, TR/TE = 1,439/50 ms, averages 4, resolution 167 × 100 × 700 μm³). MRI images were then post-processed using ImageJ.

Microparticle of iron oxide MRI for thrombus detection

MRI was performed as previously described²⁴. In brief, mice were anaesthetized using isoflurane in a mixture of O₂/N₂O (30/70) and kept under anaesthesia during all the procedure, while maintaining a body temperature of 37 °C. Before MRI, mice were subjected to caudal vein catheterization for DNA and micro-sized matrix-based magnetic particle (M3P) administration. MRI was performed with a BioSpec 7T TEP-MRI system and a surface coil (Bruker). Imaging data were obtained using a TOF sequence to visualize vascular structures, a T2*-weighted sequence for iron-sensitive imaging and a T2-weighted sequence for tissue contrast. The MRI parameters were set at TR/TE = 12/4.2 ms for the TOF sequence, TR/TE = 50/8.6 ms for the T2*-weighted sequence and TR/TE = 3,500/40 ms for the T2-weighted sequence. T2*-weighted images are presented as a stack of four slices (minimum intensity) after bias fields correction using ImageJ software.

Organ and tissue processing

Mice were deeply anaesthetized with ketamine (120 mg kg⁻¹) and xylazine (16 mg kg⁻¹) and venous blood was drawn via cardiac puncture of the right ventricle in 50 mM EDTA (Sigma-Aldrich); the plasma was isolated by centrifugation at 3,000g for 15 min and stored at -80 °C until further use. Immediately following cardiac puncture, mice were transcardially perfused with ice-cold saline. Subsequently, the CCAs from both sides as well as the aortic arches and hearts were carefully isolated and embedded in compound (OCT, Tissue-tek), frozen over dry ice and stored at -80 °C until sectioning.

Heads were cut just above the shoulders. Skin was removed from the head and the muscle was stripped from the bone. After removal of the mandibles and the skull rostral to maxillae, the whole brain with skull was post-fixed by 4% paraformaldehyde (PFA) overnight at 4 °C. Subsequently, samples were transferred to a decalcification solution of 0.3 M EDTA (C. Roth, 292.94 g mol⁻¹) at pH 7.4 and stored at 4 °C. EDTA solution was changed after 3 days. Samples were immersed with 30% sucrose in PBS and then frozen down in -20 °C isopentane (Sigma-Aldrich). Coronal sections (15 μm thick) were obtained at the level of the anterior commissure for immunohistochemical analysis. Sections were mounted on SuperfrostPlus Slides (Thermo Scientific) and stored in -80 °C.

Preparation of plasma samples for free nucleotide quantification

Mouse venous blood from cardiac puncture was drawn in 50 mM EDTA tubes. Afterwards samples were centrifuged at 1,500g for 10 min at room temperature. Plasma was isolated, transferred to a new tube and spun again at 3,000g for 10 min. Plasma was then carefully collected and immediately frozen down at -80 °C until further processing.

Histology and immunofluorescence

Carotid (5 μm) cryosections were histologically stained with haematoxylin and eosin (H&E) in 100-μm intervals. Total collagen content was assessed by Picro Sirius red staining (Abcam) in consecutive sections. For immunofluorescence staining, cryosections were fixed with 4% PFA followed by antigen blockade using 2% goat serum-blocking buffer containing 1% BSA (Sigma), 0.1% cold fish skin gelatin (Sigma-Aldrich), 0.1% Triton X-100 (Sigma) and 0.05% Tween-20 (Sigma). Next, sections were incubated overnight at 4 °C with the following primary antibodies: rat anti-mouse CD68 (1:200; ab53444, Abcam), mouse anti-mouse smooth muscle actin (1:200; ab7817, Abcam), rabbit anti-mouse Ki67 (1:200; 9129S, Cell Signaling), mouse anti-mouse caspase-1 (1:200; AG-20B-0042-C100, Adipogen), sheep anti-von Willebrand factor (1:100; ab11713, Abcam), rat anti-CD31 (1:200; BM4086, OriGene) and anti-collagen I (1:250; ab279711, Abcam). After washing, sections were incubated with secondary antibodies as following: AF647 goat anti-rat (1:200; Invitrogen), Cy3 goat anti-mouse IgG H&L (1:200; Abcam), AF594 goat anti-rabbit (1:200; Invitrogen), AF488 goat anti-mouse (1:200; Invitrogen) and AF594 donkey anti-sheep (1:200; Invitrogen). Counterstain to visualize nuclei was performed by incubating with DAPI (1:5,000; Invitrogen). Finally, sections were mounted with fluoromount medium (Sigma-Aldrich). Microphotographs of immunofluorescent samples were taken with a confocal microscope (LSM 880 and LSM 980; Carl Zeiss) using ZEN2 software (blue edition). Histological sections were imaged with an epifluorescent microscope (Axio Imager M2, Carl Zeiss) and quantified by using ImageJ software (US National Institutes of Health).

For the visualization of suspected secondary infarct lesions in the contralateral hemisphere, brain sections (15 μm) were first stained for Fluoro-Jade C (FJC) to identify degenerating neurons. FJC staining was performed using the Fluoro-Jade C Ready-to-Dilute staining kit (TR-100-FJ, Biosensis) according to the manufacturer's instructions. To confirm the secondary lesion, double staining of the microglia marker Iba-1 (1:200; FUJIFILM Wako Pure Chemical Corporation) and terminal deoxynucleotidyl transferase dUTP nick end labelling (TUNEL) staining was performed using the Click-iT Plus TUNEL Assay for In Situ Apoptosis Detection (Alexa Fluor 647 dye, C10619, Thermo Scientific) according to the manufacturer's instructions. Brain samples were photographed on an epifluorescence microscope (Zeiss Axiovert 200M, Carl Zeiss) and a confocal microscope (LSM880, Carl Zeiss).

Mouse CCA plaque analysis

Plaque vulnerability was assessed as previously described¹⁵. In brief, intima, media and necrotic core area were analysed in H&E-stained sections. The necrotic core was defined as the area devoid of nuclei underneath a formed fibrous cap. Collagen content was quantified on Picro Sirius red-stained sections. The vulnerability plaque index (VPI) was calculated as VPI = (% necrotic core area + % CD68 area)/(% smooth muscle actin area + % collagen area).

Flow cytometry analysis

Isolated CCA samples were mixed with digestion buffer, consisting of collagenase type XI (125 U ml⁻¹, C7657), hyaluronidase type 1-s (60 U ml⁻¹, H3506), DNase I (60 U ml⁻¹, D5319), collagenase type I (450 U ml⁻¹, C0130; all enzymes from Sigma-Aldrich) in 1× PBS⁴⁰, and were digested at 750 rpm for 30 min at 37 °C. After digestion, CCA materials were homogenized through a 40-μm cell strainer, washed at 500g for 7 min at 4 °C and resuspended in flow cytometry staining buffer (00-4222-26, Thermo Scientific) to generate single-cell suspensions. Cell suspensions were incubated with flow cytometry antibodies and analysed using a spectral flow cytometer (Northern Light, Cytek). Alternatively, cell suspension was incubated with the fluorescent inhibitor probe 660-YVAD-FMK (#9122, Immunochemistry Technology) to label active caspase-1 in living cells. A detailed

antibody list for flow cytometry analysis is available in the resource table in Supplementary Table 6.

For neutrophil flow cytometry, CCA single-cell suspensions (see above) or full EDTA blood was incubated with CD45-specific, CD11b-specific, Ly6C-specific, Ly6G-specific and citrullinated histone3 (citH3)-specific antibodies and analysed using spectral flow cytometry. Neutrophils were defined as CD45⁺CD11b⁺Ly6G^{high} cells; neutrophil activation was defined via citH3 detection.

Representative gating strategies for individual flow cytometry experiments are provided in Supplementary Fig. 2.

Analysis of plaque-infiltrating leukocytes

Circulating leukocytes were discriminated by intravenous administration of an anti-CD45 antibody⁴¹ (eFluor450, clone: 30-F11, eBioscience) immediately before stroke surgery. Twenty-four hours after stroke, to exclude the blood contamination in the CCA, an anti-CD45 antibody (APC-Cy7, clone: 30-F11, BioLegend) was injected intravenously 3 min before euthanasia. Then, CD45 eFluor450-positive but APC-Cy7-negative population were considered as the 'infiltrating leukocytes' population.

Immunoblot analysis

Ipsilateral and contralateral CCA materials were carefully isolated and snap frozen on dry ice. Whole frozen CCA was lysed with RIPA lysis/extraction buffer with added protease/phosphatase inhibitor (Thermo Fisher Scientific). Total protein was quantified using the Pierce BCA protein assay kit (Thermo Fisher Scientific). Whole-tissue lysates were fractionated by SDS-PAGE and transferred onto a polyvinylidene difluoride membrane (Bio-Rad). After blocking for 1 h in TBS-T (TBS with 0.1% Tween-20, pH 8.0) containing 4% skin milk powder (Sigma), the membrane was washed with TBS-T and incubated with the primary antibodies to the following antibodies: mouse anti-caspase-1 (1:1,000; Adipogen), rabbit anti-actin (1:1,000; Sigma) and rabbit anti-factor XII (1:1,000, Invitrogen). Membranes were washed three times with TBS-T and incubated for 1 h with horseradish peroxidase-conjugated anti-rabbit or anti-mouse secondary antibodies (1:5,000, Dako) at room temperature. Membranes were washed three times with TBS-T, developed using ECL substrate (Millipore) and acquired via the Vilber Fusion Fx7 imaging system.

ASC oligomerization assay

ASC oligomerization was performed as previously published⁴². In detail, bone marrow was isolated from mice and cultured for 7 days with L929 cell-conditioned medium. After differentiation, cells were washed in PBS and primed with 100 ng ml⁻¹ of lipopolysaccharide (LPS) for 4 h. Cells were either left primed or additionally activated by stimulation with 250 µg ml⁻¹ NET-DNA for 2 h. Cells were washed in PBS and detached by scraping in PBS containing 2 mM EDTA. After centrifugation, cell pellets were resuspended in 0.5 ml of ice-cold buffer A and lysed through sonification. After centrifugation to remove bulk nuclei, 20 µl of lysate was stored as input before oligomerization. Buffer A was added to the remaining lysate; following centrifugation, supernatants were diluted with CHAPS buffer and pelleted through further centrifugation. Proteins were crosslinked for 30 min at room temperature with 50 µl of CHAPS buffer containing 4 mM disuccinimidyl suberate. After centrifugation pellets were resuspended in Laemmli buffer and boiled at 70 °C for 10 min. Samples were loaded onto SDS-PAGE and separated at 150 V. Transfer was performed at 4 °C and 100 V for 1 h and membranes were blocked with 4% BSA in TBS-T. Membranes were incubated overnight at 4 °C with anti-ASC antibody (AL177, Adipogen), washed three times in TBS-T and incubated at room temperature for 1 h with goat anti-Rb horseradish peroxidase antibody. After washing and detecting the images, membranes were re-incubated with actin-antibody for 1 h at room temperature, proceeded by washing, secondary antibody and imaging.

ELISA

CCA tissue samples were carefully isolated and snap-frozen on dry ice. Whole frozen CCA was lysed with cell lysis buffer (#895347, R&D System). Then, the concentration of IL-1β in total CCA lysates was measured by ELISA according to the manufacturer's instructions (MLB00C, R&D system). Absorbance at 450 nm was measured by an iMark Microplate reader (Bio-Rad).

Gelatin zymography of mouse CCA extracts, BMDMs culture medium and patient plaque lysates

CCA tissue extracts were analysed using gelatin zymography (Novex TM 10% zymography plus protein; ZY00100BOX, Thermo Scientific) according to the manufacturer's instructions. CCA tissue was lysed with cell lysis buffer (#895347, R&D System). Total protein was quantified using a Pierce BCA protein assay kit (Thermo Fisher Scientific). Aliquots of appropriately diluted tissue extracts were loaded on gels at a total volume of 20 µl. After electrophoresis, gels were incubated in 1× Zymogram renaturing buffer (LC2670, Invitrogen) for 30 min at room temperature with gentle agitation. Afterwards, Zymogram renaturing buffer was decanted and 1× Zymogram developing buffer (LC2671, Invitrogen) was added to the gel. The gel was then equilibrated for 30 min at room temperature with gentle agitation. After an additional wash with 1× Zymogram developing buffer, the gels were incubated at 37 °C overnight. Gels were stained with a colloidal blue staining kit (LC6025, Invitrogen) and acquired on a gel scanner. BMDM culture medium was collected and loaded on gelatin zymography gels at a total volume of 25 µl. MMP activity in BMDM culture medium was analysed using the same protocol as for the tissue samples.

MMP2 and MMP9 in situ zymography

MMP2 and MMP9 in situ zymography on CCA sections was performed as previously described with slight modifications⁸. DQ-gelatin (D12054, Invitrogen) was dissolved in reaction buffer (50 mM Tris-HCl, 150 mM NaCl, 5 mM CaCl₂ and 200 mM sodium azide, pH 7.6). Cryosections (5 µm) were incubated for 2 h at 37 °C with the gelatin-containing reaction buffer. Negative control sections were pre-incubated for 1 h with the MMP inhibitor 1,10-phenanthroline (Sigma). Nuclei were stained with DAPI. MMP activity was detected with an Axio Observer Z1 microscope with ×20 magnification (Carl Zeiss). Data are shown as normalized MMP intensity (normalized MMP area = MMP⁺ area/intima area).

Neutrophil isolation and stimulation

Neutrophils were generated from the tibia and femur of transcardially perfused WT mice. After isolation and dissection of the tibia and femur, bone marrow was flushed out of the bones through a 40-µm strainer using a plunger and 1-ml syringe filled with sterile 1× PBS. Strained bone marrows cells were washed with PBS and resuspended in 1× sterile PBS with 5% BSA. Afterwards, neutrophils were isolated by using a neutrophil isolation kit (130-097-658, Miltenyi) according to the manufacturer's instructions. Of cells, 1 × 10⁷ were plated onto 150-mm culture dishes in RIPA 1640 (Gibco), supplemented with 10% FBS and 1% penicillin-streptomycin.

For the generation of NET-DNA, 2 × 10⁷ cells (for isolation, see above) were cultured in a 150-mm tissue culture-treated dish. Cells were then stimulated with 100 nM phorbol 12-myristate 13-acetate (PMA) overnight. The next day, supernatant was removed from the culture dish and processed in a centrifugation protocol for isolating NET-DNA. Cell culture supernatants were centrifuged at 500g for 10 min, then the supernatant was kept and centrifuged again at 15,000g for 10 min. Supernatant was decanted and the pellet (NET-DNA) was resolved in 50 µl of nuclease-free water. NET-DNA was then labelled with the fluorescent DNA probe DRAQ5 (Alexa 647; Thermo Fisher) following the manufacturer's instructions.

For ex vivo serum stimulation of neutrophils, 3×10^5 cells were cultured in 12-well plates. Cells were then treated with either 25% serum from stroke-operated or sham-operated mice for 4 h. As a positive control, 10 nM PMA was used. Cells were then washed and immediately fixed with 3.7% PFA/sucrose. Fixed neutrophils were then stained with cith3-specific antibody and NET-DNA was counterstained with 1 μ M SYTOX green.

cfDNA isolation from human and mouse plasma

Mouse venous blood from cardiac puncture was drawn in 50 mM EDTA 2-ml collection tubes. Samples rested at a maximum of 15 min at room temperature on the bench. Afterwards, samples were centrifuged at 3,000g for 10 min at 4 °C. Plasma was isolated, transferred to a new tube and spun again at 3,000g for 10 min. Plasma was then carefully collected and immediately frozen down at -80 °C until further processing. We used 500 μ l plasma to isolate cfDNA with a column-based kit (Plasma/Serum Cell-Free Circulating DNA Purification Kit; 55100; Norgen Biotek). In the last step, DNA was eluted with 30 μ l buffer from the column. Afterwards, total circulating DNA and single-stranded DNA were measured with a Nanodrop Spectrophotometer (1000ND, Peqlab). Double-stranded DNA (dsDNA) concentrations were acquired with a Qubit 2.0 fluorophotometer (Invitrogen) using a specific fluorescent dye-binding dsDNA (HS dsDNA Assay kit, Thermo Fisher Scientific). Dilutions and standards were generated following the manufacturer's instructions.

Length distribution of circulating cfDNA fragments after DNA isolation was acquired using the automated gel electrophoresis platform Bioanalyzer (Agilent) and the High Sensitivity DNA kit (Agilent). Data were analysed using the Bioanalyzer 2100 Expert software (Bioanalyzer, Agilent). Data in Fig. 2h (mouse, 2–72 h after stroke), Fig. 3g (mouse, 6 h after stroke), Extended Data Fig. 7d (mouse, 24 h after stroke), Extended Data Fig. 7e (mouse, 12 or 24 h after myocardial infarction) and Extended Data Fig. 8a (intravenous DNA measured 24 h after injection) were generated following the above protocol.

Human samples from patients with asymptomatic/symptomatic CCA (stroke (human; CCA sample)) were acquired at Hannover Medical School (see 'Patient cohort for carotid endarterectomy sample analysis'). Full-blood samples (blood withdrawal in EDTA collection tubes) were transported to Munich (180 min or longer transportation time on 4 °C). Once arrived, 3 ml of each sample was then centrifuged at 3,000g for 15 min, and plasma was collected and stored at -80 °C. We used 500 μ l plasma to isolate cfDNA with a column-based kit (Plasma/Serum Cell-Free Circulating DNA Purification Kit; 55100; Norgen Biotek). In the last step, DNA was eluted with 30 μ l buffer from the column. Details of the cfDNA isolation protocols are in Supplementary Table 4.

Human samples acquired at the medical centre of LMU (Munich, Germany; 'stroke (human; cfDNA methylation)') and at the medical centre of Technical university (Munich, Germany; 'MI (human)') were collected in EDTA containing tubes and centrifuged after 15–30 min at room temperature. Human myocardial infarction samples were centrifuged at 1,600g for 30 min, and plasma was collected and stored at -80 °C until cfDNA was isolated. Human stroke samples were centrifuged at 1,500g for 10 min, and plasma was collected and stored at -80 °C until further processing.

Extracellular vesicle spin down

Mouse plasma samples were diluted 1:1 with nuclease-free water. Dilution was centrifuged at 16,500g for 20 min, and then supernatant was filtered through 0.22- μ m filter. The filtered supernatant was then transferred to an ultracentrifuge and spun at 110,000g for 60 min. Supernatant was kept as 'extravesicular' DNA. The pellet was resuspended and 'vesicular' DNA concentration was measured.

Human cfDNA methylation pattern analysis

We collected platelet-poor plasma from 17 patients with ischaemic stroke (median of 73.9 years of age, interquartile range of 65.8–87.2 years of age; 10 women (58.8%)) upon hospital admission in the emergency department before any acute treatment or intervention (time from symptom onset to sampling: median of 6.5 h, interquartile range of 2.2–8.3 h). Patients had a median infarct volume of 57.4 ml (interquartile range of 40.5–124.0 ml).

cfDNA extracted from plasma was treated with bisulfite to convert unmethylated cytosines to uracils, and amplified using a two-step PCR protocol as previously described⁴³, followed by next-generation sequencing. Sequencing results were analysed to determine the proportion of molecules from each locus that carries the methylation pattern of the cell type of interest (typically complete demethylation). We used a cocktail of brain markers (methylation markers of neurons, oligodendrocytes and astrocytes) as previously described⁴⁴ and another cocktail that amplifies the markers of immune and inflammatory cells: neutrophils, monocytes, eosinophils, and T cells and B cells⁴⁵. The raw values (GE ml⁻¹ and percentage) of DNA methylation analysis are in Supplementary Table 5.

BMDM isolation and cell culture

BMDMs were isolated and cultured as previously described⁴⁸. In brief, BMDMs were generated from the tibia and femur of transcardially perfused WT mice. After careful isolation and dissection of the tibia and femur, bone marrow was flushed out of the bones through a 40- μ m strainer using a plunger and 1-ml syringe filled with sterile 1 \times PBS. Strained bone marrow cells were washed with PBS and resuspended in DMEM + GlutaMAX-1 (Gibco), supplemented with 10% FBS and 1% gentamycin (Thermo Scientific) and counted. Of cells, 5×10^7 were plated onto 150-mm culture dishes. Cells were differentiated into BMDMs over the course of 8–10 days. For the first days after isolation, cells were supplemented with 20% L929 cell-conditioned medium, as a source of M-CSF. Cultures were then maintained at 37 °C with 5% CO₂ until they reached 90% or more confluence.

BMDM stimulation with sham or stroke serum

BMDMs were cultured for 8–10 days for full differentiation. Cells were then harvested, washed, counted and seeded in flat-bottom tissue culture-treated 24-well plates at a density of 2×10^5 cells per well in a total volume of 500 μ l, and then cultured overnight for at least 16 h. BMDMs were then stimulated with LPS (100 ng ml⁻¹) for 4 h. Afterwards, the cells were incubated with serum from either stroke-operated or sham-operated WT mice (4 h post-surgery) at a concentration of 25% total volume for 1 h. Control-treated BMDMs received only FBS-containing culture medium. Afterwards, cell lysates were collected in RIPA buffer and stored at -80 °C until further processing.

For MMP secretion, the supernatant was discarded after stimulation and the cells were washed with sterile PBS to ensure no leftover serum on the cells. Afterwards, 500 μ l serum-free DMEM was added to the BMDMs, which were then incubated overnight for 16 h at 37 °C and 5% CO₂. The culture medium was then collected for further analysis.

BMDMs stimulation with NET-DNA

ASC-citrine (B6.Cg-Gt(ROSA)26Sor^{tm1.1(CAG-Pycard/mCitrine⁺,CD2*)Dtg/J}) BMDMs were cultured as described above. Cells were then harvested and seeded in a 12-well flat-bottom well plates equipped with 15-mm coverslips. A total of 3×10^5 cells were seeded per well in a total volume of 1 ml and then cultured overnight for at least 16 h (37 °C and 5% CO₂). BMDMs were then primed with LPS (100 ng ml⁻¹) for 4 h. Afterwards, BMDMs were stimulated with 250 ng of DRAQ5-labelled NET-DNA (see the section 'Neutrophil isolation and stimulation') for 1 h. BMDMs were then washed with PBS and fixed with 3.7% PFA/sucrose. Coverslips containing BMDMs were then removed from the well plates, cytoskeleton was

stained for β -tubulin (Thermo Fisher) and nuclei were counterstained with Hoechst 33342 (Immunohistochemistry.com).

En face immunofluorescence staining

Both ipsilateral and contralateral CCAs were carefully dissected, and adventitial fat and ligation nodes were thoroughly trimmed away. CCAs were then cut open, unfolded and pinned out on a silicon-elastomer for fixation in 4% PFA at room temperature for 2 h. The CCAs were then washed for 1 h at room temperature in 5% BSA with 0.3% Triton X-100 (Sigma-Aldrich). Afterwards, CCAs were incubated with rabbit anti-factor XII (1:100; PA5-116703, Invitrogen) at 4 °C overnight. After washing in 5% BSA with 0.3% Triton X-100 for 1 h at room temperature, CCAs were incubated with AF647 goat anti-rabbit (1:100; Invitrogen) and DAPI for 2 h at room temperature. Finally, CCAs were mounted with fluoromount medium (Sigma-Aldrich). Microphotographs were taken with a confocal microscope (LSM 980, Carl Zeiss).

Aspect ratio of collagen I

For assessment of the collagen structural organization at the fibrous cap, 20X PSR images from 3 to 4 sequential segments were taken. Quantitative analysis using ImageJ software was done as previously described^{46,47}. In brief, fast Fourier transformation was performed on the approximately 40- μ m subendothelial fibrous cap area. Thresholded fast Fourier transformation images then underwent an elliptic fit and the aspect ratio value was calculated, as a measure of collagen fibre distribution anisotropy at the fibrous cap region.

Statistical analysis and reproducibility

Data were analysed using GraphPad Prism version 6.0. All summary data were expressed as the mean \pm standard deviation unless indicated otherwise. All datasets were tested for normality using the Shapiro–Wilk normality test. The groups containing normally distributed independent data were analysed using a two-way Student's *t*-test (for two groups) or ANOVA (for more than two groups). Normally distributed dependent data were analysed using a two-way ANOVA. The remaining data were analysed using the Mann–Whitney *U*-test (for two groups) or Kruskal–Wallis test (*H*-test; for more than two groups). *P* values were adjusted for comparison of multiple comparisons using Bonferroni correction or Dunn's multiple comparison tests. *P* < 0.05 was considered to be statistically significant.

t-Distributed stochastic neighbour embedding for anti-Ly6G-depleted bone marrow (Extended Data Fig. 8f) was performed using the integrated tSNE platform of FlowJo (Treestar). One thousand CD45⁺ cells were used per sample. The plugin was set to 250 iterations and a perplexity value of 30.

Principal component analysis (Extended Data Fig. 3f) was performed using Rstudio version 1.1.477. Absolute values from the necrotic core, smooth muscle actin, collagen, fibrous cap thickness and CD68⁺ macrophage area were Z-scored and then principal components were calculated using the 'prcomp()' command (built-in R stats package). The arrows represent the variable correlation showing the relationship between all variables. Principal components were picked by their percentage of explained variance (62.73% (PC1) and 21.05% (PC2)) and visualized using the 'ggplot2' package (version 3.4.3; <https://ggplot2.tidyverse.org>). Relative contribution and quality of representation were calculated and visualized using the 'corrplot' package (version 0.92; <https://github.com/taiyun/corrplot>).

All in vivo experiments were performed in 3–5 independent experiments. Within one independent experiment, all groups were represented. All in vitro experiments were performed in 2–4 independent experiments. All conditions of the in vitro assays were represented in each independent experiment. Experiment data shown for Fig. 1d,i represent three independent experiments. Experiment data shown in Fig. 2c,e represent three independent experiments. Representative

images in Fig. 2f,i,k,m show the outcome of one of three independent experiments. Representative microphotographs in Fig. 3c,e show representative images from experiments that were independently repeated at least five times.

Reporting summary

Further information on research design is available in the Nature Portfolio Reporting Summary linked to this article.

Data availability

Further information, data and requests for resources or reagents should be directed to and will be fulfilled by the corresponding authors.

35. Kilkenny, C., Browne, W. J., Cuthill, I. C., Emerson, M. & Altman, D. G. Improving bioscience research reporting: the ARRIVE guidelines for reporting animal research. *PLoS Biol.* **8**, e1000412 (2010).
36. Green, J. P. et al. Discovery of an inhibitor of DNA-driven inflammation that preferentially targets the AIM2 inflammasome. *iScience* **26**, 106758 (2023).
37. Chen, Y. C. et al. A novel mouse model of atherosclerotic plaque instability for drug testing and mechanistic/therapeutic discoveries using gene and microRNA expression profiling. *Circ. Res.* **113**, 252–265 (2013).
38. Stremmel, C. et al. Inducible disruption of the c-myc gene allows allogeneic bone marrow transplantation without irradiation. *J. Immunol. Methods* **457**, 66–72 (2018).
39. Hettwer, J. et al. Interleukin-1 β suppression dampens inflammatory leukocyte production and uptake in atherosclerosis. *Cardiovasc. Res.* <https://doi.org/10.1093/cvr/cvab337> (2021).
40. Butcher, M. J., Herre, M., Ley, K. & Galkina, E. Flow cytometry analysis of immune cells within murine aortas. *J. Vis. Exp.* <https://doi.org/10.3791/2848> (2011).
41. Winter, C. et al. Chrono-pharmacological targeting of the CCL2–CCR2 axis ameliorates atherosclerosis. *Cell Metab.* **28**, 175–182.e5 (2018).
42. Lugin, J. & Martinon, F. Detection of ASC oligomerization by western blotting. *Bio Protoc.* <https://doi.org/10.21769/BioProtoc.2292> (2017).
43. Neiman, D. et al. Multiplexing DNA methylation markers to detect circulating cell-free DNA derived from human pancreatic β cells. *JCI Insights* **5**, e136579 (2020).
44. Lubotzky, A. et al. Liquid biopsy reveals collateral tissue damage in cancer. *JCI Insight* **7**, e153559 (2022).
45. Fox-Fisher, I. et al. Remote immune processes revealed by immune-derived circulating cell-free DNA. *eLife* **10**, e70520 (2021).
46. Cicchi, R. et al. Scoring of collagen organization in healthy and diseased human dermis by multiphoton microscopy. *J. Biophotonics* **3**, 34–43 (2010).
47. Tsai, M. R., Chiu, Y. W., Lo, M. T. & Sun, C. K. Second-harmonic generation imaging of collagen fibers in myocardium for atrial fibrillation diagnosis. *J. Biomed. Opt.* **15**, 026002 (2010).

Acknowledgements We thank K. Thuß-Silczak for excellent technical support; Q. Zhou for support with ultrasound analysis; U. Schillinger and R. Fang for support in establishing the small-animal MRI analysis; O. Söhnlein for critical input in study design and establishing the tandem stenosis model; and R. D. Stauss, C. Schrimpf and M. Wilhelmi for their support in collecting human carotid plaque samples. This work was funded by the Vascular Dementia Research Foundation, the European Research Council (ERC-SIGs 802305 and 759272), the 'Else-Kröner-Fresenius-Stiftung' (2020_EKSE.07), the China Scholarship Council, the Medical Research Council grant MR/T016515/1, and the German Research Foundation (DFG) under Germany's Excellence Strategy (EXC 2145 SyNergy ID 390857198 and EXC-2049 ID 390688087), through FOR 2879 (ID 405358801), CRC 1123 (ID 238187445), TRR 295 (ID 424778381), TRR 332 (ID 449437943), TRR 355 (ID 490846870) and by grant ME 3696/3-1.

Author contributions J.C. and S.R. performed most of the experiments, analysed the data and contributed to the writing of the manuscript. G.M.G. provided the human carotid endarterectomy samples. M.G., A.K., T.L. and S.W. acquired and analysed the clinical epidemiological data. A.H., R.S. and Y.D. performed the DNA methylome analysis on human samples, which were collected and analysed by S.T. D.M. and C.S. performed the bone marrow transfer experiments. C.J., A.P. and D.V. performed the in vivo MRI. V.H. provided AIM2-deficient, NLRP1-deficient and NLRP3-deficient animals. S.Z., C.F., X.L., O.C., J.Z., S.M., C.S. and Y.A. performed the experiments and analysed the data. D.B., J.P.G., H.S. and M.D. contributed critical material and techniques for this study. H.B.S. and M.D. contributed critical input to study design and manuscript writing. A.L. initiated and coordinated the study, analysed the data and wrote the manuscript.

Competing interests The authors declare no competing interests.

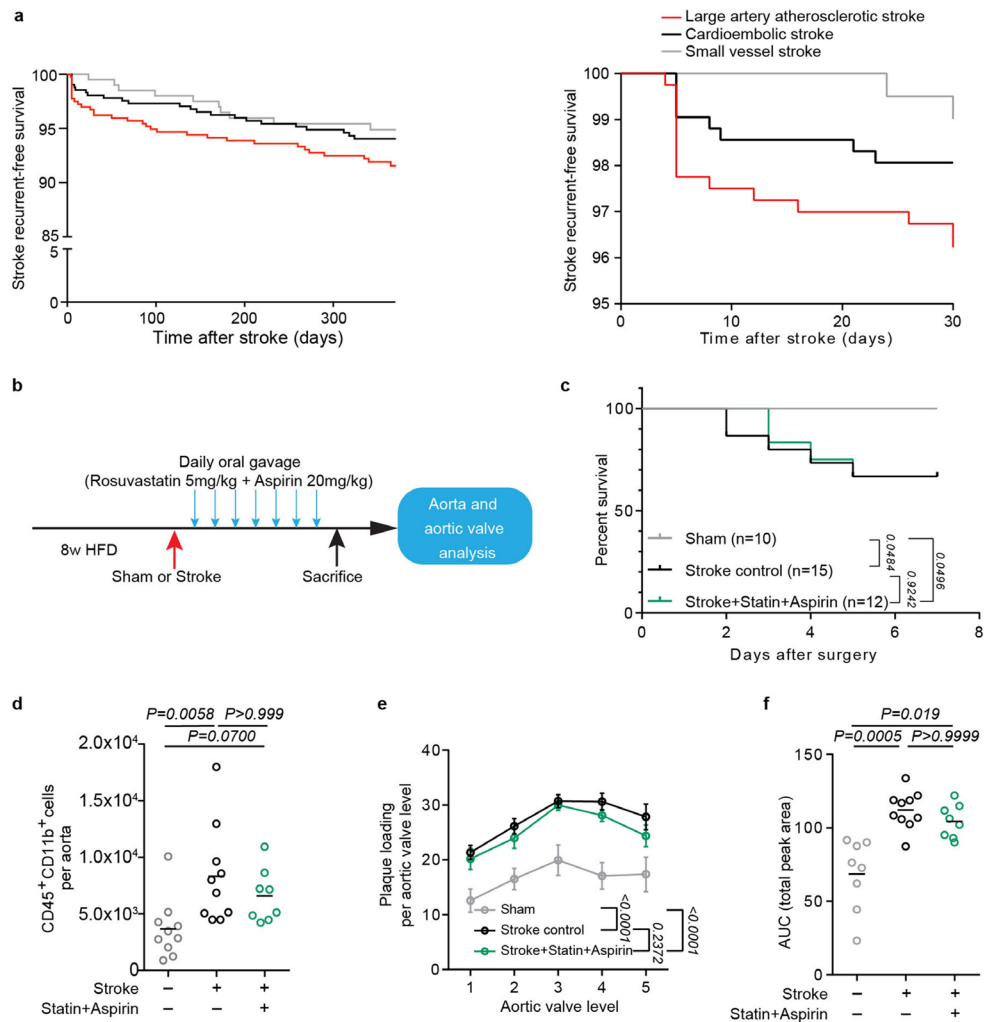
Additional information

Supplementary information The online version contains supplementary material available at <https://doi.org/10.1038/s41586-024-07803-4>.

Correspondence and requests for materials should be addressed to Stefan Roth or Arthur Liesz.

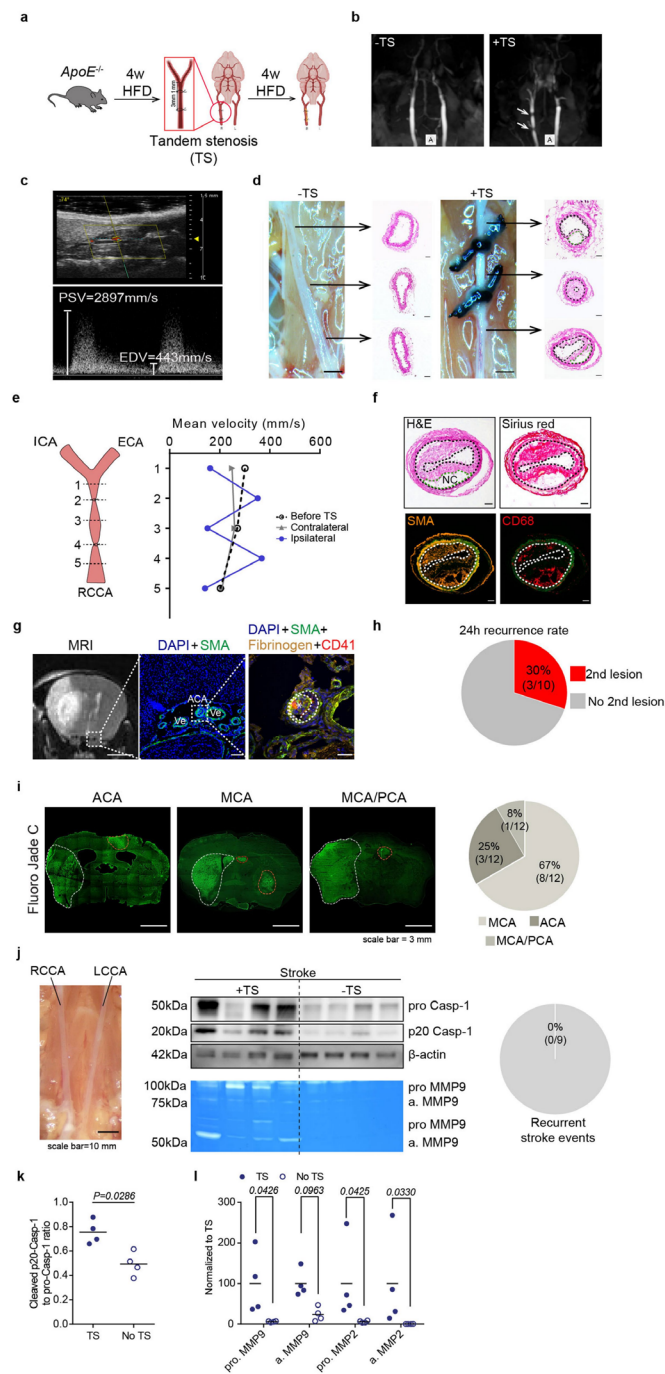
Peer review information Nature thanks Alan Tall and the other, anonymous, reviewer(s) for their contribution to the peer review of this work. Peer reviewer reports are available.

Reprints and permissions information is available at <http://www.nature.com/reprints>.



Extended Data Fig. 1 | Established secondary prevention fails to attenuate early post-stroke vascular inflammation and atheroprotection. a. Kaplan-Meier curves for recurrence-free survival of stroke patients from the same cohorts (PROSCIS and DEMAS/DEMAS) as shown in Fig. 1a. Recurrence-free survival is illustrated by etiology of the incident stroke for the full-time range of 1 year after the incident event (left) and magnified for the first post-stroke month (right). Recurrence risk is highest after large artery atherosclerosis stroke in the early (first week) after the incident event. **b.** Experimental design: 8 w-old HFD fed *ApoE*^{-/-} mice underwent sham or stroke surgery. Mice were treated orally with either control or a combination of Rosuvastatin (5 mg/kg)

and Aspirin (20 mg/kg) for 7 consecutive days after stroke. **c.** Kaplan-Meier survival curves of stroke control, statin and aspirin treated, or sham operated mice. Mantel-Cox test; n = 10 (sham), n = 15 (control), n = 12 (statin + aspirin treatment). **d.** Flow cytometry analysis of whole aorta cell suspensions for total monocyte (CD45⁺CD11b⁺) cell counts between control or treated mice after stroke compared to sham-operated mice (ANOVA, n = 8–10 per group). **e, f.** Quantification of aortic valve plaque load displayed no differences between stroke control and statin + aspirin-treated mice. Data is shown as **e.** percentage of plaque area per aortic valve level and **f.** area under the curve (ANOVA, n = 8–10 per group).

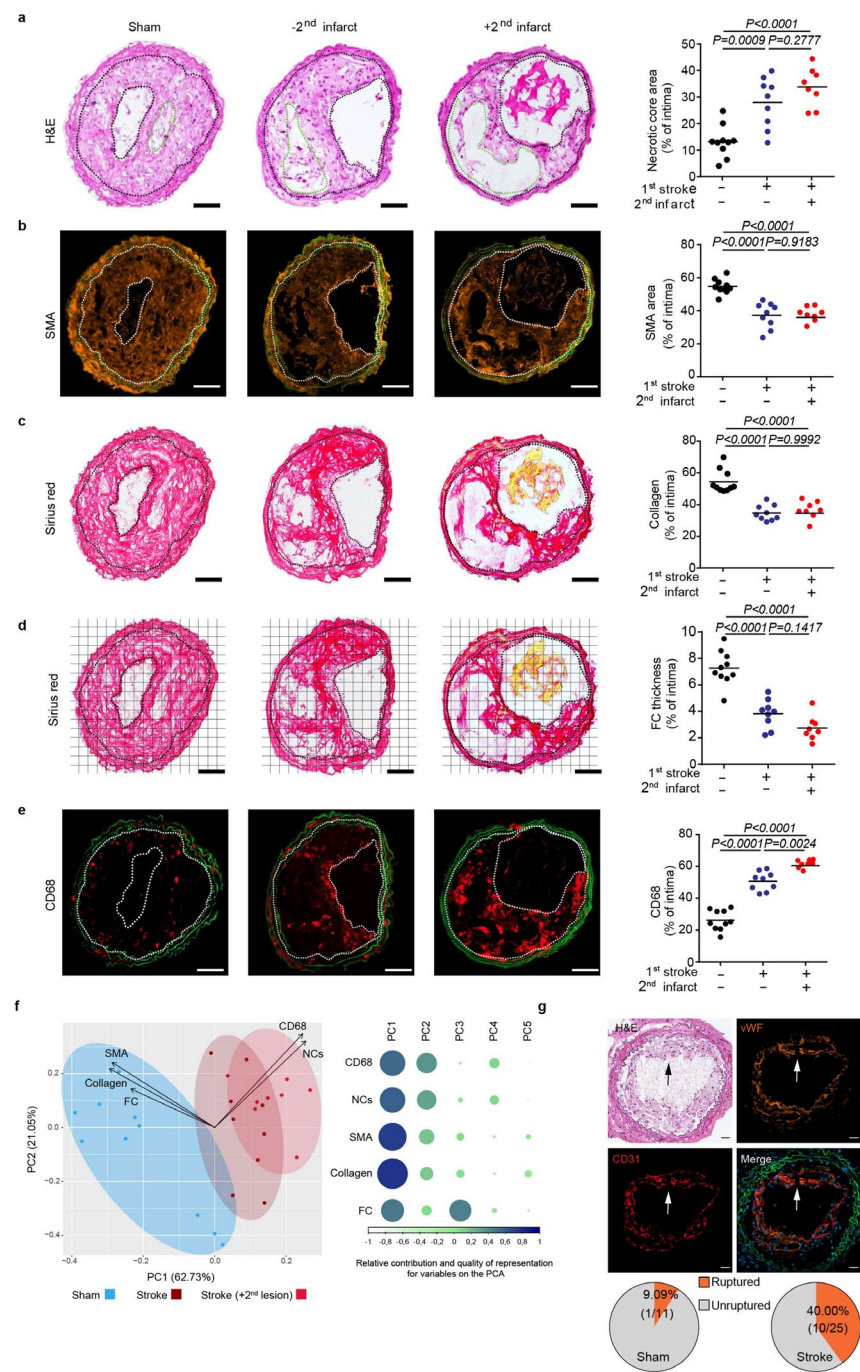


Extended Data Fig. 2| See next page for caption.

Extended Data Fig. 2 | Animal model of rupture-prone CCA plaques.

a. Schematic illustration of the tandem stenosis (TS) model for induction of vulnerable atherosclerotic plaques: 8 w-old HFD fed *ApoE*^{-/-} mice received tandem stenosis (TS) surgery on the right common carotid artery (RCCA). Mice were then fed with high fat diet for an additional 4 w. **b.** Representative images of CCA MRI TOF sequence 4w after mice received control or TS surgery. White arrows highlight the two ligations on the RCCA. **c.** Representative pulse-wave mode ultrasound image of the RCCA 4 w after TS, imaged at the location of proximal ligation at 40 MHz (upper panel). Corresponding CCA velocity waveform measured at the location of proximal ligation location 4 w after TS surgery (lower panel). PSV: peak systolic velocity, EDV: end diastolic velocity. **d.** Representative photograph of the CCA anatomy and corresponding H&E staining for each vessel segment 4 w after TS surgery of both CCAs (-TS represents contralateral (left) CCA without TS ligation; +TS represents ipsilateral (right) CCA with TS ligation, scale bar = 100 μ m; H&E staining, scale bar = 50 μ m). **e.** Schematic description of locations for blood flow measurement on the right CCA (ICA: internal carotid artery; ECA: external carotid artery; RCCA: right common carotid artery). Corresponding quantification of mean velocity in the CCA measured at both CCAs before and 4 w after TS surgery (right). **f.** Representative images of the unstable plaque in the right CCA 4 w after TS surgery (area between two dotted lines indicates intima area, green dotted line

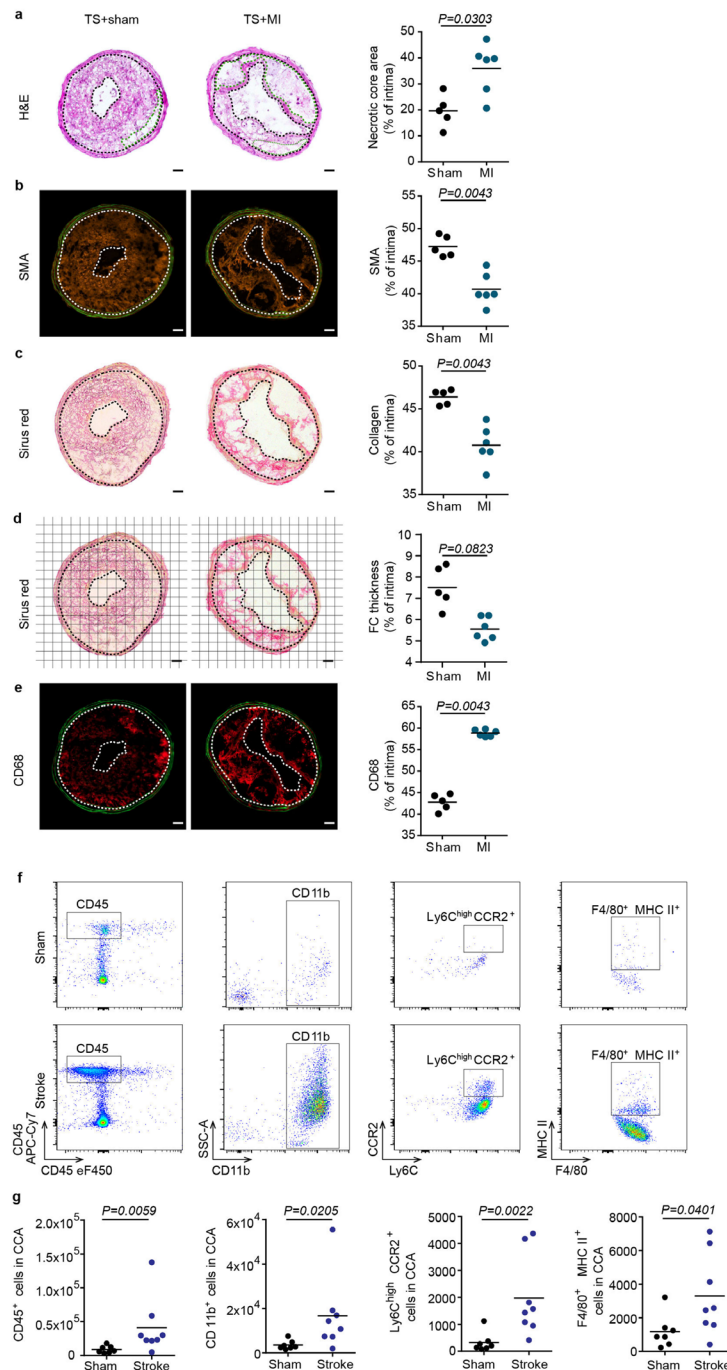
indicates necrotic core, scale bar = 50 μ m). **g.** Representative T2 MRI image (left) and immunohistochemistry of a thrombus formation stained for smooth muscle actin (SMA), Fibrinogen and thrombocytes (CD41) in the ACA territory. **h.** 8-week-old *ApoE*^{-/-} mice fed a high cholesterol diet (HCD-fed *ApoE*^{-/-}) underwent tandem stenosis (TS) surgery, and stroke surgery 4w later. The recurrence of secondary ischemia in the contralateral hemisphere was examined by histological analysis 24 h after stroke surgery (n = 10 per group). **i.** Analysis of the vessel territory of secondary ischemic events in all mice from Fig. 1c. Vessel territories were defined as MCA, ACA or MCA/PCA territory (n = 12 per group). **j.** HCD-fed *ApoE*^{-/-} mice did not undergo tandem stenosis (TS) surgery, but stroke surgery 4w later. Left: Representative microphotograph of the RCCA and LCCA without TS. Middle: Western blot analysis of caspase-1 cleavage and MMP2/9 zymography in the CCA without TS. Right: Detection of recurrent ischemic events in mice without TS, but stroke (n = 9 per group). Raw membrane images of immunoblots and zymography images with cropping indication can be found in Supplementary information 1. **k.** Quantification of cleaved caspase-1 p20 intensity normalized to b-actin in CCA lysates with or without TS surgery (U test, n = 4 per group). **l.** Quantification of MMP2 and MMP9 (pro- and active form) normalized to TS surgery in CCA lysates from mice with or without TS surgery (n = 4 per group; K test).



Extended Data Fig. 3 | See next page for caption.

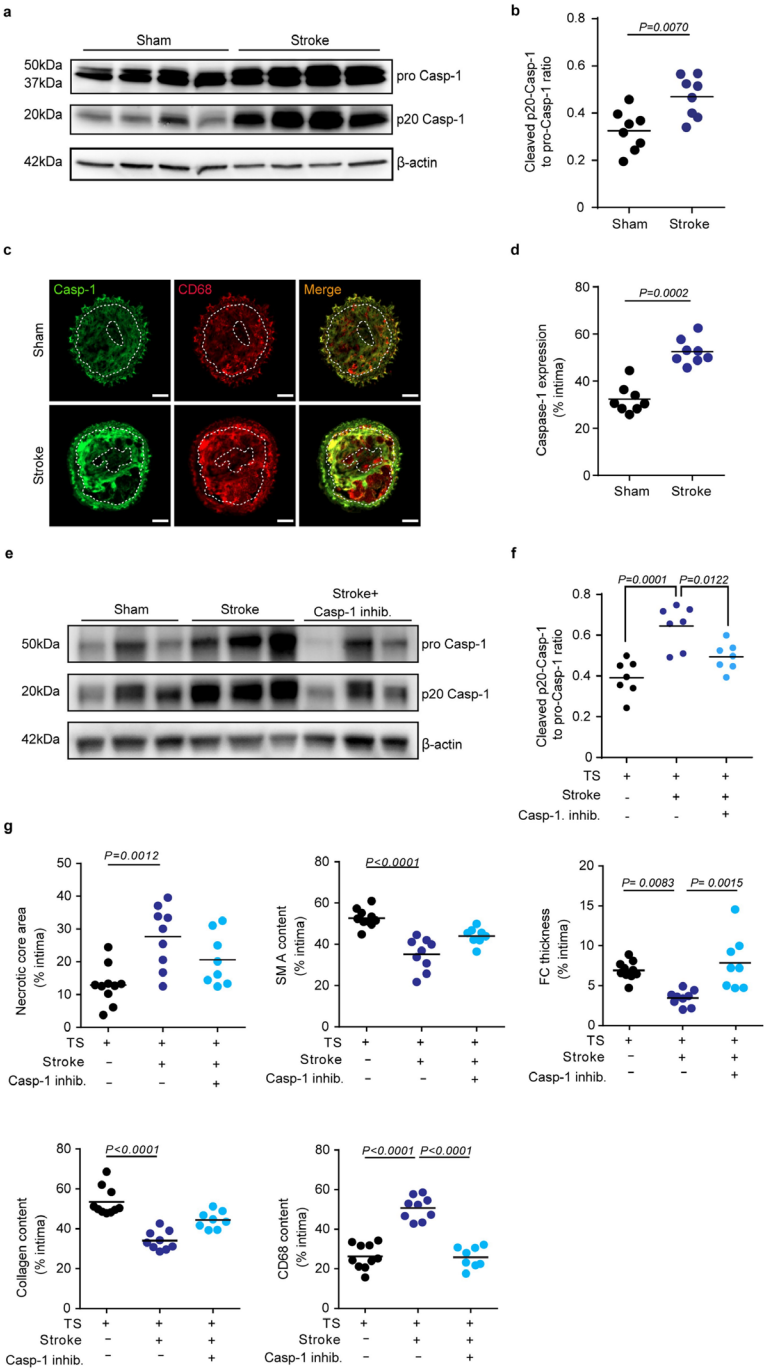
Extended Data Fig. 3 | Stroke accelerates plaque destabilization and causes plaque rupture. **a.** Representative microphotographs of CCA H&E staining. Area between two black dotted lines represents intima. Green dotted lines represent necrotic cores. Necrotic core area was quantified as the percentage of total intima area (ANOVA, $n = 8-10$ per group). **b.** Representative images of smooth muscle actin (SMA) immunofluorescence staining. SMA area was quantified as the percentage of total intima area (ANOVA, $n = 8-10$ per group). **c.** Representative microphotographs of Picro-Sirius red staining. Collagen area was quantified as the percentage of total intima area (ANOVA, $n = 8-10$ per group). **d.** Representative images of Picro-Sirius red stained CCA sections with the according grid for fibrous cap (FC) thickness quantification. FC thickness was quantified at the locations where the FC crossed the applied grid (ANOVA,

$n = 8-10$ per group). **e.** Representative microphotographs of CD68 immunofluorescence staining. Images were segmented by thresholding to convert fluorescence signal into a binary image. CD68 area was quantified as the percentage of total intima area (ANOVA, $n = 8-10$ per group). **f.** Left: Principal component analysis (PCA) using CCA plaque vulnerability readouts from sham, stroke and stroke mice with detected secondary lesion found in **a.** to **e.** ($n = 8-10$ per group) Right: Contribution of the Plaque vulnerability readouts in principal component 1 to 5 (PC1 to PC5), weighted for their relative quality of representation in the PCA. **g.** Arrows indicate a disrupted fibrous cap in lesion. The pie charts illustrate the proportion of mice with ruptured CCA plaques 1 w after sham or stroke surgery ($n = 11$ or 25 mice per group)(all scale bars = $50 \mu\text{m}$).



Extended Data Fig. 4 | MI exacerbates plaque vulnerability and stroke leads to more cellular inflammation. Representative microphotographs of H&E a., SMA b., Picro-Sirius red c., fibrous cap thickness analysis d., and CD68 e. staining in CCA sections 1w after sham or myocardial infarction (MI) surgery (scale bar = 50 μ m). Area between two dotted lines indicate intima area. Green dotted line represents necrotic core area. Corresponding quantification of necrotic core area, SMA, collagen and CD68 area 1w after sham or MI operated

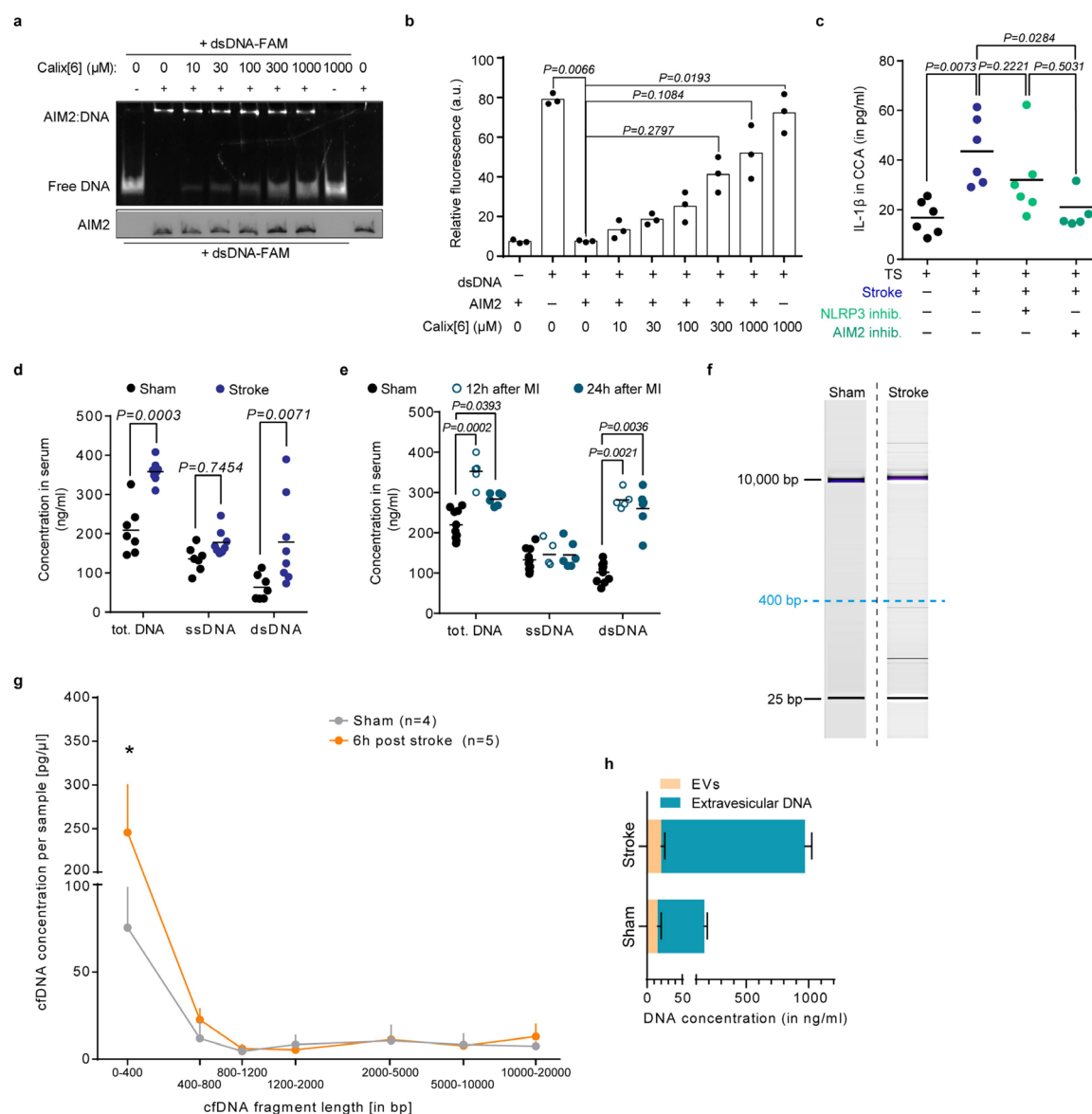
mice (quantification were performed as described in Extended Data Fig. 3, U test, $n = 5-6$ per group). **f.** Representative gating strategy for flow cytometry analysis of whole CCA cell suspensions 24 h after sham or stroke surgery. **g.** Flow cytometry analysis of CCA cell suspensions showing total leukocytes (CD45⁺), monocytes (CD11b⁺), proinflammatory subset (Ly6C^{high} CR2⁺) and macrophages (F4/80⁺ MHCII⁺) cell counts after experimental stroke compared to sham (U test, $n = 7-8$ per group).



Extended Data Fig. 5 | See next page for caption.

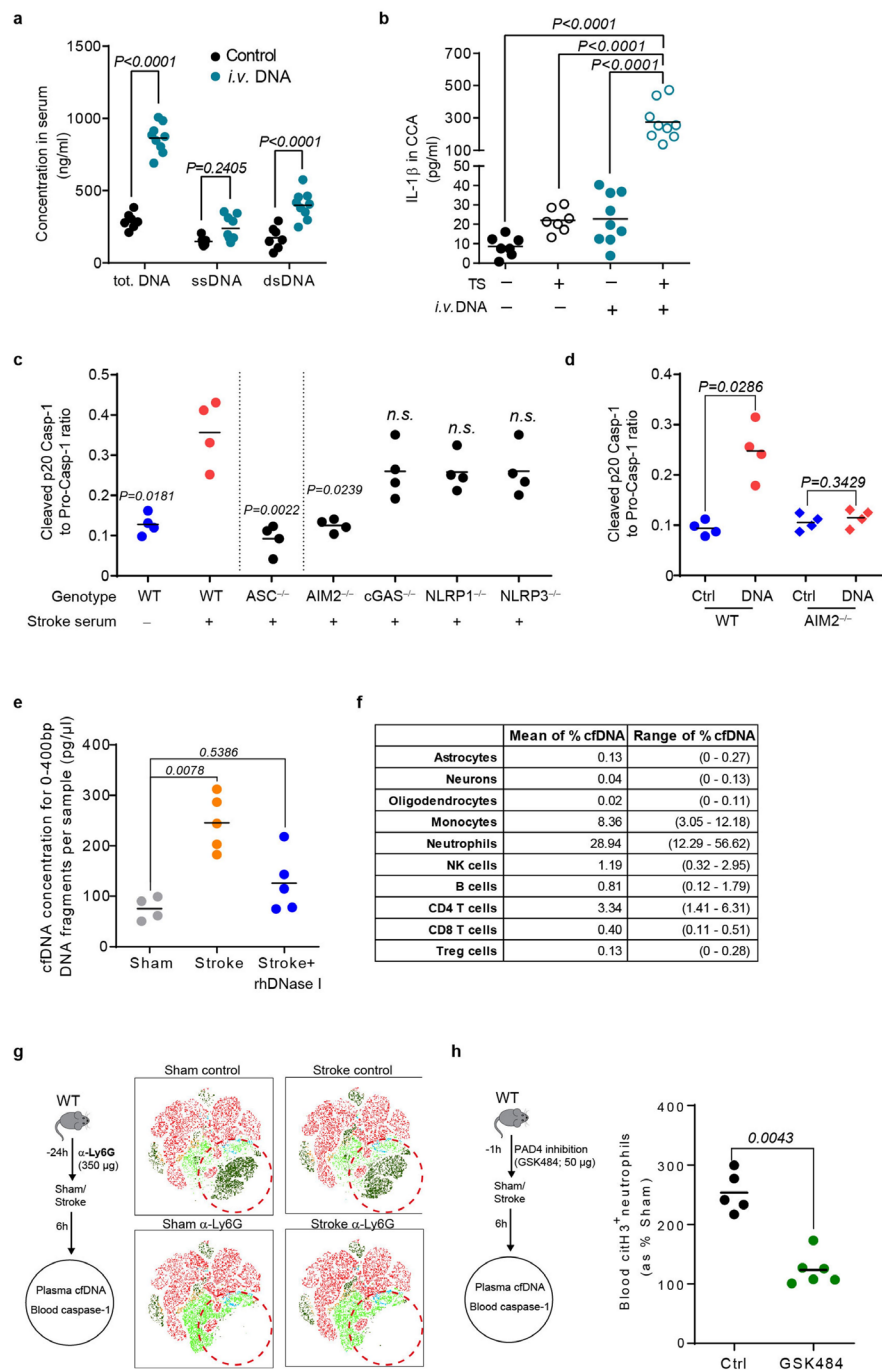
Extended Data Fig. 5 | Stroke induces inhibitable inflammasome activation in atherosclerotic plaques. **a.** Representative immunoblot of different cleavage forms of caspase-1 in CCA lysates with TS 1w after sham or stroke surgery. **b.** Quantification of cleaved caspase-1 (p20 Casp-1) as ratio to pro caspase-1 (ProCasp-1; U test, n = 8 per group). **c.** Representative immunofluorescence staining of caspase-1 (Casp-1) in CCA sections 1w after sham or stroke surgery (scale bar = 50 μ m). Images were segmented by thresholding to convert fluorescence signal into a binary image. Area between two white dotted lines represent intima. **d.** Caspase-1 expression was quantified as the percentage of total intima area (U test, n = 8 per group). **e.** Representative immunoblot image

of the different cleavage forms of caspase-1 (Casp-1) in CCA lysates 1w after sham, stroke control and stroke + caspase-1 inhibitor (VX765) administration. **f.** Quantification of cleaved p20 Casp-1 intensity normalized to β -actin in CCA lysates (+TS) 1w in the three treatment groups (black: sham; blue: stroke; light blue: stroke + VX765, ANOVA, n = 7 per group). **g.** Quantification of necrotic core area, SMA, Fibrous cap thickness, collagen and CD68 area 1w after sham or stroke in the respective treatment groups (performed as shown in Extended Data Fig. 3, ANOVA, n = 8–10 per group). Raw membrane images of all immunoblots can be found in Supplementary Fig. 1.



Extended Data Fig. 6 | Post-stroke plaque inflammasome activation is mediated by cell-free DNA. **a**, Representative EMSA gel microphotograph of different Calixarene concentrations (0–1000 μM) interfering with the AIM2-dsDNA complex resulting in increased free DNA. **b**, Quantification of AIM2-free DNA based on its relative fluorescence in the EMSA assay (K test; n = 3 per group; 3 independent experiments). **c**, ELISA analysis of IL-1β in CCA lysates from mice with tandem stenosis (TS), 24 h after stroke in control-, NLRP3 inhibitor- (MCC950) or AIM2 inhibitor- (4-sulfonic calixarene) treated mice, and in sham operated mice (K test; n = 5–6 per group). **d**, Total cell-free DNA (cfDNA), single-stranded DNA (ssDNA) and double-stranded DNA (dsDNA) in mouse serum 24 h after sham or stroke surgery (U test, n = 7–8 per group).

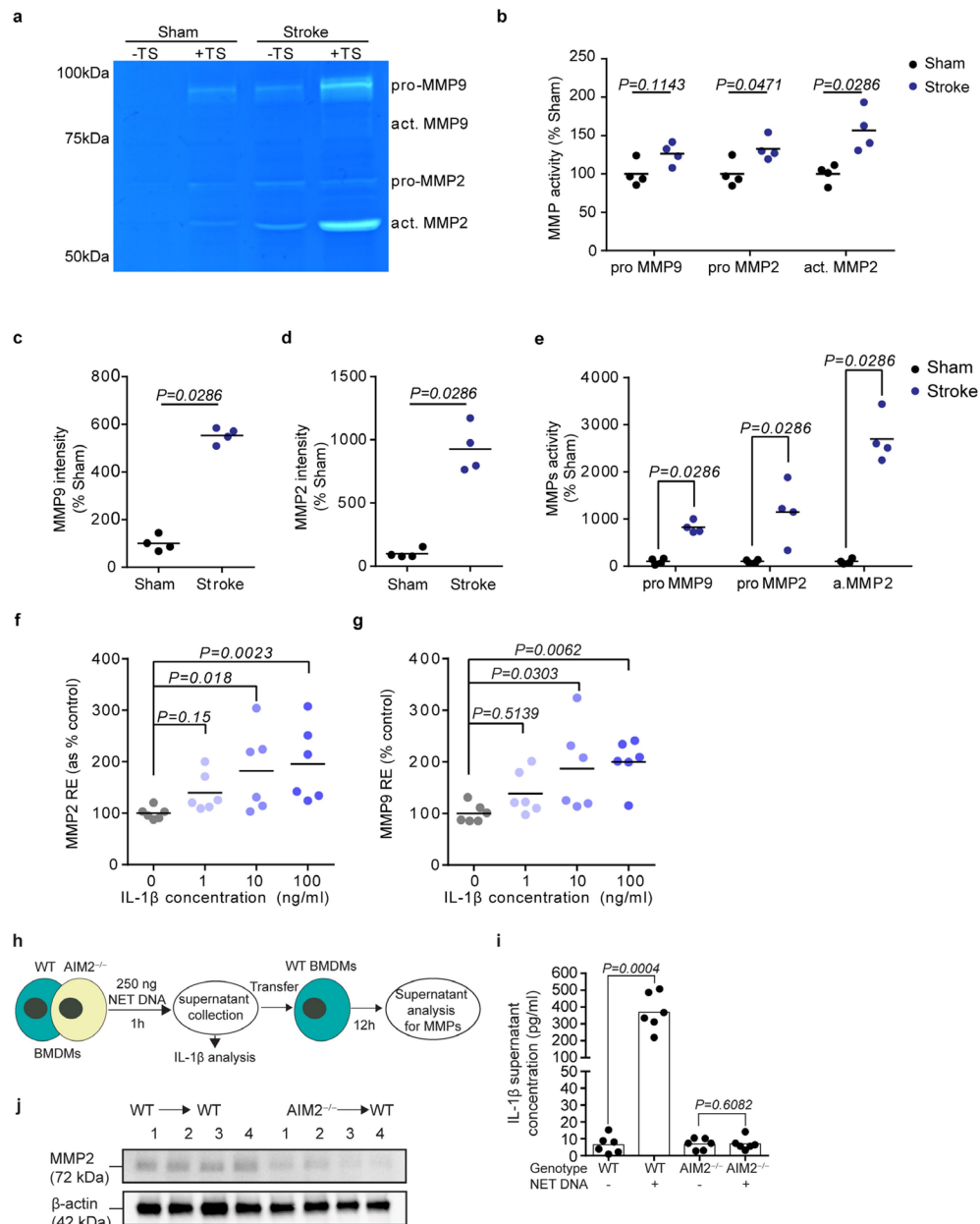
e, Total DNA, ssDNA and dsDNA in mice serum after sham or 12 h, 24 h after myocardial infarction (MI) surgery (black: sham; blue circle: 12 h after MI; blue dot: 24 h after MI, multiple t test, n = 5–10 per group). **f**, Representative gel electrophoresis photographs of cfDNA isolated from sham and stroke-operated mouse plasma. **g**, Quantification of electrophoresis-based cfDNA fragment length analysis of sham or stroke-operated mice (K test; n = 4–5 per group; 0–400 bp fragments: Sham vs Stroke: $P < 0.0001$). **h**, Quantification of extra-vesicular and intra-vesicular DNA after sham or stroke surgery (U test; EV DNA: Sham vs Stroke $P = 0.1746$; vesicle-free DNA: Sham vs Stroke $P = 0.0079$; n = 5 per group).



Extended Data Fig. 7 | See next page for caption.

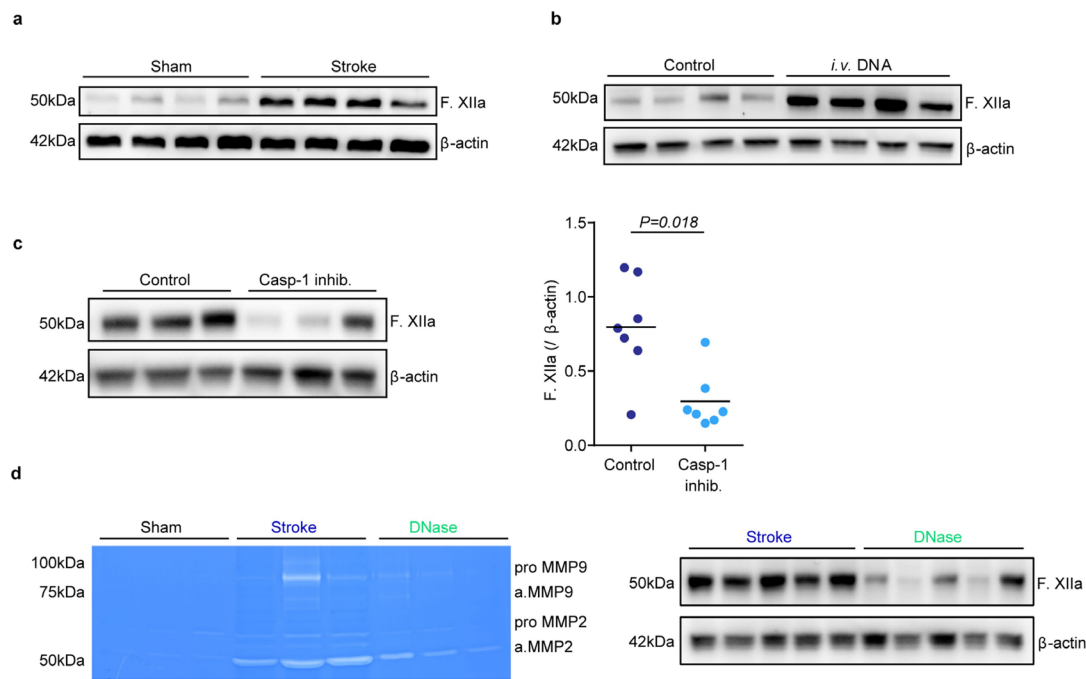
Extended Data Fig. 7 | Early neutrophil activation after stroke drives systemic inflammasome activation. **a.** total DNA, ssDNA and dsDNA in mouse serum were measured 24 h after control or *i.v.* DNA intravenous injection (multiple t test, control, n = 7; DNA challenge, n = 9). **b.** ELISA analysis for IL-1 β in CCA lysates 24 h after *i.v.* DNA challenge (black, control; blue, DNA challenge, ANOVA, n = 7–9 per group). **c.** Caspase-1 cleavage was analyzed via western blotting in BMDMs primed (100 ng/ml LPS for 4 h) and stimulated for 2 h with 25% serum of stroke-operated WT mice. WT BMDMs were compared with BMDMs deficient for ASC, AIM2, cGAS, NLRP1 and NLRP3 (K test; n = 4 per group; 2–3 independent experiments). **d.** Caspase-1 cleavage in WT and AIM2-deficient BMDMs was analyzed by priming (100 ng/ml LPS for 4 h)

and stimulating with 250 ng cell-free NET DNA for 2 h (K test; n = 4 per group; 2 independent experiments). **e.** Quantification of short-fragmented (0–400 bp) cfDNA from sham or stroke-operated mice which received rhDNase I treatment (1000U) immediately after stroke surgery (K test; n = 4–5 per group). **f.** Exact percentages (mean and range) of total cfDNA per cell population presented in Fig. 3a. **g.** Representative t-distributed stochastic neighbor embedding (tSNE) plot of antibody-based (α -Ly6G; 1A8) neutrophil depletion efficacy 24 h after antibody administration. **h.** Quantification of citrullinated Histone3' (citH3') neutrophils in control or PAD4 inhibitor treated mice. Data is presented as percentage of respective sham group (U test; n = 5–6 per group).



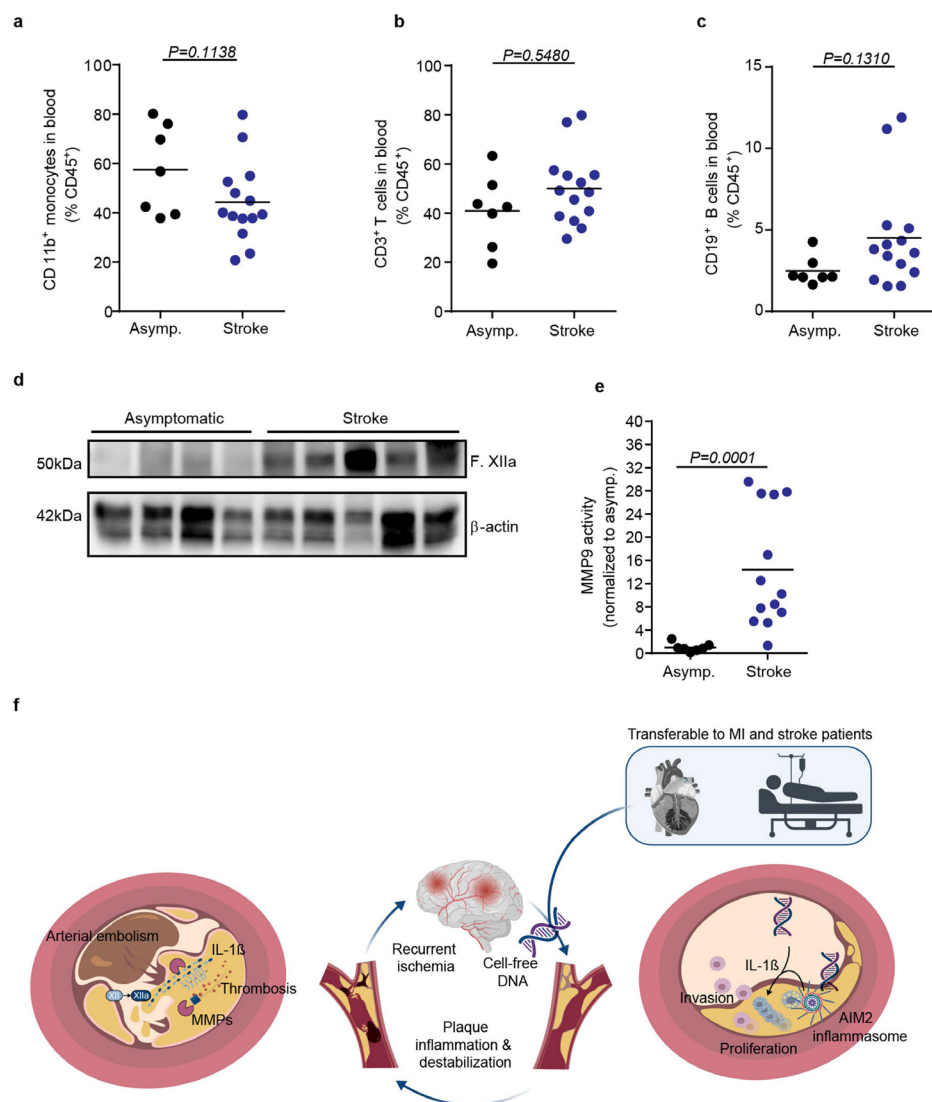
Extended Data Fig. 8 | Stroke increases matrix metalloproteinase activity in atherosclerotic plaques. **a**. Representative images of gelatin zymography of CCA lysates for MMP activity in mice 1w after sham or stroke surgery. The region of MMP activity appears as a clear band against dark blue background where the MMP has digested the gelatin substrate on the zymogram gel. **b**. MMP activity shown in **a** was quantified as the gelatin digestion area 1w after stroke surgery normalized to sham operated mice (multiple t test, $n = 4$ per group). **c**, **d**. Quantification of MMP9 and MMP2 intensity from immunoblot micrograph shown in Fig. 3b (normalized to sham stimulated, U test, $n = 4$ per group). **e**. MMP activity shown in Fig. 4c was quantified as the gelatin digestion area in the stroke serum-stimulated medium normalized to sham

serum-stimulated group (t test, $n = 4$ per group). **f**. Relative expression (RE) of MMP2 expression in WT BMDMs after IL-1 β stimulation was quantified as the percentage of the control group (H test, $n = 6$ per group). **g**. Relative expression (RE) for MMP9 mRNA in BMDMs after IL-1 β stimulation (H test, $n = 6$ per group). **h**. Schematic for NET DNA challenge on WT or AIM2 $^{-/-}$ BMDMs and subsequent supernatant transfer to WT BMDMs for MMP expression. **i**. IL-1 β supernatant concentration from WT and AIM2 $^{-/-}$ BMDMs stimulated with NET DNA ($n = 6$ per group). **j**. Representative Immunoblot image of Supernatant MMP2 analysis from BMDM supernatants ($n = 3$ per group). Raw images of zymography with cropping indication can be found in Supplementary Fig. 1h.



Extended Data Fig. 9 | Stroke initiates the intrinsic coagulation cascade at atherosclerotic plaques. All analyses were performed on CCA lysates in mice with stenotic CCA plaques after TS surgery in HFD fed *ApoE*^{-/-}. **a.** Representative immunoblot of activated Factor XII (F. XIIa) 1 w after stroke or sham surgery. **b.** Representative immunoblot micrograph of F. XIIa in CCA lysates 24 h after *i.v.* DNA challenge. **c.** Representative immunoblot of the F. XIIa in CCA lysates 24 h after stroke in mice treated with control treatment or caspase-1 inhibition

(VX765). Corresponding quantification of F. XIIa intensity normalized to β-actin in CCA lysates 1 w after stroke in control- or caspase-1 inhibitor-treated mice (U test, n = 7 per group). **d.** Representative gelatin zymography of CCA lysates for MMP activity in mice 24 h after sham, stroke or stroke + rhDNase I treatment (left). Representative immunoblot of F. XIIa in +TS CCA lysates 24 h after surgery (right). Raw membrane images of immunoblots with cropping indication can be found in Supplementary Fig. 1j–n.



Extended Data Fig. 10 | Blood leukocyte counts do not differ between stroke and asymptomatic patients with high-grade atherosclerosis.

a–c. Flow cytometry analysis of blood from asymptomatic patients or stroke patients showing the percentage of monocytes (CD11b⁺), T cells (CD3⁺) and B cells (CD19⁺) out of total leukocytes (CD45⁺) (U test, asymptomatic patients, $n = 7$; symptomatic patients, $n = 13$). **d.** Representative immunoblot from asymptomatic and stroke patients for F. XIIa and β -actin (Quantification can be found in Fig. 4i). **e.** Quantification of MMP9 activity normalized to the activity in asymptomatic patients (Representative image shown in Fig. 4h).

Raw membrane images of immunoblots with cropping indication can be found in Supplementary Fig. 1q. **f.** Overview schematic: Stroke leads to the release of NETosis-derived cell-free DNA activating the AIM2 inflammasome and subsequent secretion of IL-1 β . The release of IL-1 β drives MMP expression in atherosclerotic plaque, leading to fibrous cap destabilization. The fibrous cap rupture initiates the activation of the intrinsic coagulation cascade resulting in atherothrombosis and subsequent arterio-arterial embolism with secondary brain infarctions.

4. Publication II

Innate immune memory after brain injury drives inflammatory cardiac dysfunction

Alba Simats^{1,2,22}, Sijia Zhang^{1,22}, Denise Messerer³, Faye Chong⁴, Sude Beşkardeş⁴, Aparna Sharma Chivukula³, Jiayu Cao¹, Simon Besson-Girard¹, Felipe A. Montellano^{7,13}, Caroline Morbach⁸, Olga Carofiglio¹, Alessio Ricci¹, Stefan Roth¹, Gemma Llovera¹, Rashween Singh¹, Yiming Chen¹, Severin Filser¹, Nikolaus Plesnila^{1,9}, Christian Braun¹⁰, Hannah Spitzer¹, Ozgun Gokce^{1,11}, Martin Dichgans^{1,9,11,12}, Peter U. Heuschmann^{13,14,15}, Kinta Hatakeyama¹⁶, Eduardo Beltrán^{9,17,18}, Sebastian Clauss^{3,5,6,19}, Boyan Bonev^{4,20}, Christian Schulz^{3,5,6,12,21}, Liesz A^{1,9,23*}

1 Institute for Stroke and Dementia Research (ISD), University Hospital, LMU Munich, Munich, Germany

2 Cerebrovascular Research Laboratory, Institute of Biomedical Research of Barcelona (IIBB), Spanish National Research Council (CSIC), Barcelona, Spain

3 Medizinische Klinik und Poliklinik I, University Hospital, LMU Munich, Munich, Germany

4 Helmholtz Pioneer Campus, Helmholtz Zentrum München, Neuherberg, Germany

5 Institute of Surgical Research at the Walter-Brendel-Centre of Experimental Medicine University Hospital, LMU Munich Munich Germany

6 German center for Cardiovascular Research (DZHK), Partner Site Munich Heart Alliance, Munich, Germany

7 Department of Neurology, University Hospital Würzburg, Würzburg, Germany

8 Department Clinical Research & Epidemiology, Comprehensive Heart Failure Center, and Department Medicine I, University Hospital Würzburg, Germany

9 Munich Cluster for Systems Neurology (SyNergy), Munich, Germany

10 Institute of Legal Medicine, Faculty of Medicine, LMU Munich, Munich, Germany

11 German Center for Neurodegenerative Diseases (DZNE), Partner Sites Munich and Bonn, Germany

12 German center for Cardiovascular Research (DZHK), Partner Site Munich Heart Alliance, Munich, Germany

13 Institute for Clinical Epidemiology and Biometry, Institute for medical Data Sciences, Clinical Trial Centre Würzburg, Julius-Maximilian University Würzburg, Würzburg, Germany

14 Institute for medical Data Sciences, University Hospital Würzburg, Würzburg, Germany

15 Clinical Trial Centre Würzburg, University Hospital Würzburg, Würzburg, Germany

16 Department of Pathology, National Cerebral and Cardiovascular Center, Suita, Japan

17 Institute of Clinical Neuroimmunology, University Hospital, LMU Munich, Munich, Germany

18 Biomedical Center (BMC), Faculty of Medicine, LMU Munich, Martinsried, Germany

19 Interfaculty Center for Endocrine and Cardiovascular Disease Network Modelling and Clinical Transfer (ICONLMU), LMU Munich Munich Germany

20 Physiological Genomics, Biomedical Center, Ludwig-Maximilians-Universität München, Munich, Germany

21 Department of Immunopharmacology, Mannheim Institute for Innate Immunoscience (MI3), Medical Faculty
Mannheim, Heidelberg University, Mannheim, Germany.

22 These authors contributed equally

23 Lead contact

*Correspondence to: Arthur.Liesz@med.uni-muenchen.de

Summary

The medical burden of stroke extends beyond the brain injury itself and is largely determined by chronic comorbidities that develop secondarily. We hypothesized that these comorbidities might share a common immunological cause, yet chronic effects post-stroke on systemic immunity are underexplored. Here, we identify myeloid innate immune memory as a cause of remote organ dysfunction after stroke. Single-cell sequencing revealed persistent pro-inflammatory changes in monocytes/macrophages in multiple organs up to three months after brain injury, notably in the heart, leading to cardiac fibrosis and dysfunction in both mice and stroke patients. IL-1 β was identified as a key driver of epigenetic changes in innate immune memory. These changes could be transplanted to naïve mice, inducing cardiac dysfunction. By neutralizing post-stroke IL-1 β or blocking pro-inflammatory monocyte trafficking with a CCR2/5 inhibitor, we prevented post-stroke cardiac dysfunction. Such immune-targeted therapies could potentially prevent various IL-1 β -mediated comorbidities, offering a framework for secondary prevention immunotherapy.

INTRODUCTION

We and others have previously shown that acute brain injuries induce a sterile, systemic inflammatory response.¹ The inflammatory response to sterile injury is rapidly initiated by the release of immunogenic alarmins, such as nuclear proteins or DNA from necrotic cells to the blood circulation.² It is further characterized by an increase in blood cytokine levels, the mobilization of immune cells and profound changes in immune cell composition and function.³ In contrast to the acute inflammatory response within hours to few days, the chronic effects of brain injury on systemic immunity are largely unknown. Few studies mainly investigating blood biomarkers have suggested chronic changes in the concentrations of circulating cytokines and other inflammatory markers, such as Interleukin (IL)-6, IL-1, C-reactive protein (CRP), Interferon (IFN)- γ and High-Mobility Group Box 1 (HMGB1).⁴⁻⁷ However, a detailed analysis of the chronically compromised systemic immune compartment after brain injury is still missing and the underlying mechanisms are largely unknown.

Acute brain injuries due to ischemic stroke are a leading cause of mortality and long-term disabilities in adults. Besides the early mortality and morbidity due to the ischemic brain injury itself, long-term morbidity after stroke is also due to the high prevalence of secondary comorbidities and complications, such as cognitive impairment and dementia, post-stroke depression, cardiac events, persistent vascular inflammation and stroke-induced metabolic disturbances.⁸⁻¹² Yet, the exact cause of this increased risk of long-term secondary comorbidities after stroke remains elusive.

Recent studies have demonstrated long-term changes in the function of innate immune cells after bacterial infections or vaccination. This phenomenon has been termed innate immune memory or ‘trained immunity’ in contrast to antigen-specific adaptations in long-lived lymphocytes (T and B cells).¹³ Innate immune memory has been demonstrated in proof-of-concept infection studies to alter the responsiveness to pathogens after re-infection. This represents a beneficial evolutionary mechanism for the clearance of infectious pathogens, but can also result in potentially pathological functions during aging and autoimmunity due to aberrant inflammation.¹⁴ Yet, barely any information is available on mechanisms and consequences of trained immunity after sterile tissue injuries. Epigenetic changes in myeloid cells have been reported in models of organ transplantation,¹⁵ experimental arthritis and in patients with systemic lupus erythematosus.^{16,17} Similarly, alterations in hematopoiesis and pro-inflammatory monocyte priming has been associated with cardiovascular disease,

particularly atherosclerosis and associated comorbidities.¹⁸ We hypothesized that sterile tissue injuries such as stroke might result in similar long-term innate immune memory, and that these long-term immunological consequences after stroke might drive secondary comorbidities.

RESULTS

Stroke induces long-term inflammatory changes in systemic monocytes/macrophages

To test a potential effect of stroke on long-term systemic inflammation, we performed a comprehensive single-cell mRNA sequencing analysis of CD45⁺CD11b⁺ myeloid cells from blood and multiple peripheral organs 1 month after experimental ischemic stroke, which have previously been associated with inflammatory consequences of brain injury in the acute phase (**Fig. 1A**).^{2,19–21} For this, we used a well-established experimental stroke model of transient occlusion of the middle cerebral artery²², which results in relatively large lesion volumes, but mice largely recover from the neurological symptoms already within 1-2 weeks (Fig. S1A). After performing unsupervised clustering, we projected a total of 29,124 myeloid cells and identified 20 independent clusters based on the most variable genes (**Fig. 1B**, Fig. S1B). We found a large number of genes to still be differentially regulated at this late chronic time point after stroke particularly within the population of monocytes/macrophages, while other cell populations including neutrophils or dendritic cells were less affected (**Fig. 1C**). Also, transcriptomic changes in monocytes/macrophages were not associated with changes in the frequencies of any subcluster (Fig. S1C, D) that would explain the difference. The post-stroke monocytic transcriptomic signature was associated with a pro-inflammatory phenotype, characterized by significant upregulation of various biologically relevant inflammatory signaling pathways of circulating monocytes and tissue macrophages, including increased expression of genes involved in chemotaxis and cell adhesion (e.g. Cx3cr1, Lyz2, Icam1 and Itga4), cytokine- and interferon (IFN)-mediated signaling pathways (e.g. Csf1r, Cebpa, Itgb2, Il10ra, Aim2, Irf8 and Irf5) and pattern recognition receptors (PRRs) (e.g. Irak2 and Tab2) (**Fig. 1D**, Fig. S1E,F).^{23,24} Furthermore, through a biological network analysis, we confirmed the involvement of other pro-inflammatory mediators, such as interleukin (IL)-12, IL-1 and IFN- α and - β , and the downstream NF- κ b and Akt signaling pathways in the activated phenotype of resident monocytes/macrophages in peripheral organs one month after stroke (Fig. S1G).

Across organs, changes in the monocyte/macrophage population were particularly pronounced in the heart and liver. Principal component analysis based on a total of 18,835 genes showed that changes in blood, spleen, and lung were more subtle (**Fig. 1E**, Fig. S1H). Specifically, we detected the selective expansion of a Ly6C^{high}-expressing monocyte population in hearts 1 month after stroke (**Fig. 1 F, G**, Fig. S1I), which changed the

differentiation trajectories of monocytes to cardiac macrophages. Correspondingly, we term this population “post-stroke monocytes/macrophages” (**Fig. 1H**, Fig. S1K, L). In addition, cardiac Ly6C^{high} monocytes after stroke showed increased expression of genes related to tissue residency when compared to circulating monocytes (Fig. S1J). Moreover, we found that the genes driving the post-stroke differentiation of monocytes into cardiac macrophages positively correlate with immune response and leukocyte activation pathways (Fig. S1M, N). Taken together, these results suggest that stroke chronically promotes the recruitment of circulating Ly6C^{high} monocytes to the heart, which might further differentiate into tissue-resident macrophages.

Stroke results in chronic cardiac diastolic dysfunction

To assess the functional consequences of changes in the cardiac monocyte/macrophage population during the chronic phase following stroke, we investigated cardiac function using Doppler echocardiography. We observed a persistent reduction in end-diastolic left ventricle (LV) volume, while the systolic function, measured by the ejection fraction and fractional shortening, was only transiently affected by stroke in the acute phase (**Fig. 2A**, Fig. S2A, Table S1). These findings suggest the selective development of chronic diastolic dysfunction, which was further confirmed using pulse wave doppler of the apical four-chamber-window demonstrating compromised left ventricular compliance by decreased mitral valve E wave deceleration time (Fig. S2B). Heart failure in patients with preserved ejection fraction but diastolic dysfunction is commonly associated with cardiac fibrosis, which impairs the rapid LV filling due to increased myocardial stiffness.^{25,26} Hence, we evaluated the amount of fibrosis in hearts after stroke or in control mice and observed significantly increased LV fibrosis one month after stroke, which remained increased still at 3 months post-stroke (**Fig. 2B**, Fig. S2C, D). Importantly, this observed post-stroke cardiac fibrosis was not associated with renal dysfunction, gross anatomical cardiac alterations or persistent perturbations in autonomous cardiac innervation beyond the acute post-stroke phase (Fig. S2E-J). To test the potential impact of post-stroke cardiac fibrosis, we next conducted an invasive electrophysiological (EP) study one month after stroke. In line with a previous study identifying the role of cardiac inflammation as a risk factor for atrial fibrillation²⁷, we observed a higher inducibility of atrial arrhythmias following burst stimulation in stroke mice, which was absent for control mice (**Fig. 2C**, Table S2).

We further characterized the composition of the extracellular matrix (ECM) in hearts after stroke, and observed that increased cardiac fibrosis was mainly due to increased deposition of type I collagen (**Fig. 2D**, Fig. S2K). Further analysis of collagen orientation in the LV myocardium by second harmonic generation microscopy revealed increased fiber disorganization after stroke, suggesting ECM remodeling in addition to increased deposition (**Fig. 2E**). Therefore, we analyzed cardiac matrix metalloproteinase (MMP) activity—key effector enzymes in ECM remodeling—and observed significantly increased MMP9 activity by gel zymography (**Fig. 2F**) as well as total pro-MMP9 protein content after stroke (Fig. S2L). More specifically, we detected by smFISH significantly increased *Mmp9* transcripts in cardiac macrophages, as the most likely source of increased cardiac MMP9 expression, which was confirmed by rt-PCR of sorted cardiac monocytes/macrophages (**Fig. 2G**, Fig. S2M). Corresponding to results of the single-cell sequencing analysis (see Fig. 1F, G), we also observed by flow cytometry an increased number of Ly6C^{high} monocytes and CCR2⁺ cardiac monocytes/macrophages in post-stroke hearts (**Fig. 2H**, Fig. S2N). These results suggest a higher infiltration of circulating monocytes and an enhanced monocyte-to-macrophage differentiation chronically after stroke.^{28,29} In addition, we observed that circulating monocytes after stroke also have a significantly increased expression of *Mmp9* (**Fig. 2I**).

We next aimed to validate the translational relevance of these observations. First, we were able to confirm the development of post-stroke chronic cardiac dysfunction in three representative stroke patients recruited by the Stroke Induced Cardiac FAILure study (SICFAIL) consortium that have been followed-up by cardiac echocardiography at 3 and 6 months after the incident stroke event (**Fig. 3A**). In addition, we obtained myocardial autopsy samples from patients that had died 1-3 months after stroke or from age-matched control subjects that had died without cardiac or brain disorder (confirmed by autopsy, **Fig. 3B**, Table S3). We observed significantly increased ECM deposition in the left ventricular wall of stroke patients (**Fig. 3C, D**). We also detected a significant increase in CCR2⁺ monocyte counts in post-stroke hearts, which correlated with cardiac collagen content, while total monocyte and macrophage counts did not differ between groups (**Fig. 3E-G**). Consistent with our experimental results, human cardiac macrophages also expressed significantly more *MMP9* transcripts after stroke (**Fig. 3H**). Finally, we performed bulk mRNA sequencing on adjacent tissue sections used for the histological analyses above and found significant transcriptional differences between control subjects and after stroke (**Fig. 3I, J**). Interestingly, several of the upregulated genes in stroke patients were associated with extracellular matrix remodeling

including *PON1* (paraoxonase 1) and *KRTCAP2* (Keratinocyte-associated protein 2). Taken together, we observed marked cardiac fibrosis and ECM remodeling in both experimental mice and stroke patients, which was further associated with diastolic dysfunction after experimental stroke. A hallmark of this secondary cardiac pathology after stroke is the increased recruitment and proinflammatory profile of cardiac monocytes/macrophages.

Stroke promotes chronic monocyte recruitment into the heart

Using an inducible myeloid progenitor reporter mouse strain (Ms4a3^{creERT2}xAi14; Fig. S3A-C), we observed that cellular recruitment of cardiac monocytes/macrophages occurs not only as an acute response to stroke, but persists over time as a chronic long-term consequence (**Fig 4A**). In addition, based on *in vivo* EdU-labeling experiments, we observed that more than 95% of cardiac myeloid cells will have been replaced within one month after stroke (**Fig. 4B**), underscoring the significance of infiltrated monocytes in influencing post-stroke cardiac function. Therefore, we further studied the contribution of peripheral monocytes to heart fibrosis using an inducible reporter mouse strain under control of the *Ccr2* promoter to label infiltrating monocytes (*Ccr2*^{creERT2}xAi14, **Fig 4C**). Cardiac interstitial cells from mice one month after stroke and control mice were analyzed by single cell sequencing, excluding intravascular cells by i.v. antibody labeling. We identified 20 cell clusters corresponding to the heterogeneous cell populations of cardiac cell subsets (Fig. S3D). A more detailed analysis identified 7 distinct populations of cardiac monocytes and macrophages (**Fig 4D**, Fig. S3E). *Ccr2*-tdTomato (tdT) expression was specifically enriched in 4 of the monocyte/macrophage subsets (**Fig. 4E, F**). Unsupervised trajectory analysis further confirmed our finding that circulating Ly6C^{high} monocytes infiltrate the heart and acquire a tissue-resident monocyte/macrophage phenotype (**Fig 4G, H**). In addition, we observed that invading tdT⁺ cells after stroke are characterized by an upregulation of various biologically relevant signaling pathways (**Fig. 4I**). Furthermore, we performed cell-cell interaction analysis using CellChat between the tdT⁺ cell subsets as source and cardiac fibroblasts as target cells, revealing a large number of up-regulated interactions (while none were down-regulated) associated with processes involved in tissue fibrosis and inflammation (**Fig. 4J**). Using *in situ* smFISH for Collagen I mRNA in conjunction with Vimentin staining, we detected a significant increase in Vimentin-positive fibroblasts as well as higher expression of *Collagen-I* transcripts in fibroblasts chronically after stroke (**Fig. 4K**).

Bone marrow cellularity and function is chronically altered after stroke

To explore the potential mechanisms of post-stroke immune mediated cardiac dysfunction, we performed an in-depth analysis of the bone marrow (BM) myeloid compartment in the chronic phase after stroke. We analyzed long-term effects of stroke on the BM by single cell sequencing. We identified 21 cell clusters and the respective differentiation trajectories from hematopoietic stem and progenitor cells (HSPCs) to all other mature myeloid populations (**Fig. 5A, B**, Fig. S4A) and uncovered a distinct transcriptomic signature in Ly6C^{high} monocytes chronically after stroke (**Fig. 5C**). Additionally, we observed a substantial number of DEGs in HSPCs, suggesting that also progenitor populations exhibited persistent transcriptional alterations during the chronic stage after stroke which were associated with inflammatory pathways (Fig. S4B, C). Moreover, the post-stroke transcriptomic signature in mature monocytes from the BM was also highly conserved in circulating monocytes and differentiated monocytes recruited to peripheral organs (Fig. S4D). Apolipoprotein E (ApoE) and Lipoprotein lipase (Lpl) were consistently transcriptionally upregulated after stroke, which was additionally confirmed on protein level (Fig. S4E). Stroke-induced transcriptional changes in HSPCs and mature monocytes persisted up to three months after stroke, suggesting a sustained and potentially progressive effect of stroke on the BM transcriptomic landscape (Fig. S4F).

To validate these findings, flow cytometry analyses were conducted, confirming altered BM cellularity (**Fig. 4D, E**, Fig. S4G, H). Labeling of proliferating cells with a single intraperitoneal EdU injection one month after stroke indicated significantly increased proliferation rates of myeloid progenitor cell populations (Fig. S4I). Of note, the increased myelopoiesis after stroke was dependent on the lesion severity, since no effect on BM cellularity was observed after a transient ischemic attack or minor stroke (Fig. S4J).

Stroke induces persistent innate immune memory

To test the persistence and potentially causal role of the observed myeloid changes chronically after stroke, we transplanted GFP-positive, enriched HSPCs from BM one month after stroke or control surgery into naïve recipients, using a genetic BM depletion model (poly(I:C) administration to Mx1^{Cre}:c-myb^{fl/fl} mice) in order to avoid confounding effects by irradiation or chemotherapy (**Fig. 5F**). One month after transplantation, we isolated GFP⁺ transplanted myeloid cells for single-cell mRNA sequencing and confirmed successful BM repopulation

for all analyzed animals, without differences in the BM repopulation potential between groups (**Fig. 5G**, Fig. S5A-E). Differential gene expression between stroke and control transplanted BM cells showed substantial transcriptomic differences one month after transplantation in the naïve recipient mice (Fig. S5F, G). Interestingly, comparing the most significantly regulated transcriptomic pathways between the transplanted mice to the original differences between animals one month after stroke and control surgery revealed a highly conserved phenotype in the transplanted cells after stroke (**Fig. 5H**). Both BM cells from stroke mice and BM cells from recipient mice transplanted with stroke BM cells retained a pro-inflammatory activated phenotype. Projecting all individual samples into a PCA bidimensional space, we found that cells from mice transplanted with stroke BM showed spatial proximity to cells from stroke mice (Fig. S4H, I), confirming that myeloid cells acquire a distinct pro-inflammatory phenotype after stroke that is transmissible by BM transplantation.

One month after BM transplantation, we also isolated GFP⁺ transplanted myeloid cells (CD45⁺CD11b⁺) from the heart and blood of recipient mice. Using unsupervised clustering, we identified distinct myeloid GFP⁺ populations in both the heart and blood (Fig. S5J). Using pseudotime analysis on the combined dataset from blood and heart, we observed a shift in the differentiation trajectory from blood monocytes to heart monocytes/macrophages following stroke (**Fig. 5I**). The altered pseudotime trajectory post-stroke was driven by a differentially higher contribution of blood-derived Ly6C^{high} monocytes to tissue-resident monocytes and macrophages after stroke (**Fig. 5I, J**). In addition, we found that a considerable proportion of the DEGs identified in circulating monocytes also remained differentially expressed in cardiac monocyte/macrophages after stroke (Fig. S5K). These common genes were found to participate in pathways related to stress response, immune cell activation, migration, and differentiation. We next analyzed the hearts of BM recipient mice for hallmarks of ECM remodeling observed after stroke. We found significantly increased *Mmp9* expression in cardiac macrophages of mice receiving BM from stroke donors and more specifically, an increase of *Mmp9* expression particularly in transplanted GFP⁺ cardiac monocytes/macrophages (**Fig. 5 K, L**). Moreover, we observed significantly increased cardiac fibrosis in animals receiving the stroke BM transplant in comparison to control BM recipients (**Fig. 5M**). Together, these findings demonstrate that myeloid function is not only stably altered after stroke but that these changes in the myeloid compartment are sufficient to drive secondary cardiac fibrosis.

Innate immune memory is mediated by early post-stroke Interleukin-1 β secretion

The observed effects all indicate a phenomenon described after vaccination and in infection models as “trained immunity”¹⁴, which generally describes a heightened response of innate immune cells to subsequent stimuli. Indeed, we observed that primary monocytes as well as BM-derived macrophages isolated from stroke mice had an increased phagocytic activity compared to cells from control mice (**Fig. 6A**). Furthermore, cells from mice with a stroke also showed an increased response to cytokine stimulation (Fig. S6A), overall confirming the development of trained immunity due to stroke.

A characteristic hallmark of trained immunity is epigenetic reprogramming of myeloid cells. Therefore, we first assessed histone modifications at one month after stroke or in control mice for key histone marks and identified changes in both enhancer-associated marks (H3K4me1 and H3K27ac), as well as in H3K4me3, which is a histone modification associated with active promoters¹⁴ (Fig. S6B). Next, we wanted to examine if similar TFs are involved in rewiring of the epigenetic landscape at promoters in HSPC and monocytes. Correspondingly, we identified differential enrichment of several transcription factor (TF) motifs including CTCF, STAT1/2, GABPA, CEBPD, GFI and KLF14 in HSPC (**Fig. 6B**). These TF have been previously described to regulate survival and proliferation of HSPC, their differentiation towards the myeloid lineage and their inflammatory phenotype.^{30–34} We also evaluated the chromatin profiling of mature monocytes isolated from mice one month after stroke or control conditions. Consistent with the findings in HSPCs, we found that H3K4me3 levels in monocytes were tightly linked to diverse TF motifs after stroke, including CTCF and several regions associated with the NF-kb and IL-1 signaling pathways, and a pro-inflammatory response, such as E2F2, ATF7, STAT1 and KLF14 (**Fig. 6C**).^{32,34–36}

We previously identified systemic inflammasome activation and subsequent Interleukin (IL)-1 β secretion in response to tissue injury including stroke, with serum IL-1 β concentrations peaking within the first hours after injury to similar peak levels as observed after stimulation with lipopolysaccharide (Fig. S6C, D).² Studies in experimental infection models have suggested IL-1 β -mediated effects to be involved in epigenetic reprogramming.¹⁷ Therefore, we performed single-cell ATAC sequencing for analysis of open chromatin accessibility in control mice and in animals one month after stroke which either received IL-1 β neutralizing antibodies or vehicle control. We obtained a total of 13,520 nuclei from Lin⁻CD45⁺CD11b⁺ BM cells, and identified a total of 11 clusters which were superimposed on the BM mRNA

sequencing UMAP plot (see Fig. 5A), confirming coverage of the complete BM cell heterogeneity (**Fig. 6D**). We identified in the HSPC as well as in the mature Ly6C^{high} monocyte clusters distinct differences in chromatin accessibility one month after stroke compared to control mice (Fig. S6E, F, Table S4). Next, we particularly focused on potentially important cell-type-specific differentially-active regulatory sequences,³⁷ and identified significant changes in TF motifs between stroke and control conditions (**Fig. 6E**). These analyses confirm our findings that stroke induces a pronounced alteration in the activity of several TF in HSC, including CTCF, ETV4 and RUNX2, which have been previously described to regulate HSPC function.^{38–40} Similarly, we also confirmed that stroke changed the epigenetic landscape of mature Ly6C^{high} monocytes, by changing the motif accessibility associated with TF involved in stress and immune responses, such as CTCF, NRF1 (also known as NFE2) and FOS:JUND(AP1).^{41–46} Importantly, IL-1 β neutralization prevented most of the stroke-induced changes in chromatin accessibility in both, HSPC and mature Ly6C^{high} monocytes (**Fig. 6E**). To explore stroke-regulated TFs, we identified genes with differential expression between control and stroke conditions linked to these transcription factors. These genes were involved in inflammation and cytokine signaling, including IL-1 β signaling. (Fig. S6G,H).

Finally, to confirm that IL-1 β drives the epigenetic reprogramming observed after stroke we used bulk ATAC-sequencing of the HSPC-enriched myeloid fraction of BM (i.e. HSPCs) cells treated with recombinant IL-1 β . We observed significant alterations in chromatin accessibility across a range of genomic regions in HSPCs treated with IL-1 β , although most of the changes were quantitative (**Fig. 6F**). This analysis revealed an enrichment of TF motifs in IL-1 β -treated HSPCs that are consistent with those identified in both the analysis of histone modification sites and the single-cell ATAC-seq analyses after experimental stroke. Altogether, these results demonstrate the critical role of IL-1 β in inducing epigenetic changes leading to post-stroke trained immunity.

Interleukin-1 β -driven innate immune memory mediates remote organ dysfunction after stroke

Beyond its role in post-stroke trained immunity, we aimed to further test the role of IL-1 β in the post-stroke increased myelopoiesis and monocyte recruitment to the heart. Therefore, we evaluated the heart and BM myeloid composition one week after injection of recombinant (r)IL-1 β in naive mice without a stroke (**Fig. 7A**). By flow cytometry, we observed a

substantial increase in the Ly6C^{high} cardiac monocytes and CCR2^{high} monocytes/macrophages in the hearts rIL-1 β -treated mice (**Fig. 7B**) and found correspondingly increased myelopoiesis, characterized by elevated counts of HSPCs and mature monocytes after rIL-1 β injection (**Fig. 7C**). Notably, we observed efficient normalization of BM cellularity to levels of control mice in stroke animals receiving acute IL-1 β neutralization by rIL-1 β -specific antibodies (**Fig. 7D, E**, Fig. S7A, B). In turn, anti-IL-1 β treatment during the acute phase reduced circulating Ly6C^{high} monocyte counts one month post-stroke (**Fig. 7F**), and the post-stroke increase in CCR2^{high} cardiac monocytes/macrophages was also restored to control levels after IL-1 β neutralization (**Fig. 7G**). Correspondingly, preventing release by blocking caspase-1 activation by administration of the caspase-1 inhibitor VX-765,² similarly prevented the post-stroke increase in myelopoiesis (Fig. S7C). Of note, delayed neutralization of IL-1 β levels at 2 weeks after stroke failed to rescue the post-stroke increase in myelopoiesis (Fig. S7D), confirming that the post-stroke inflammasome-dependent acute IL-1 β release but not a chronic stimulation by potentially residual circulatory IL-1 β primes the post-stroke increase in myelopoiesis and cardiac pathology.

Finally, we observed that acute (but not delayed) neutralization of the early IL-1 β release was sufficient to prevent the long-term cardiac phenotype by significantly reducing *Mmp9* expression of cardiac monocytes/macrophages and cardiac fibrosis to levels of control mice without a stroke (**Fig. 7H, I**, Fig. S7E). These findings suggest that the IL-1 β -driven epigenetic changes leading to trained immunity can be causally involved in mediating the chronic cardiac fibrosis after stroke.

Blocking BM-to-heart trafficking of monocytes prevents post-stroke cardiac dysfunction

Despite its striking efficacy on innate immune memory and cardiac secondary comorbidities, the translational use of neutralizing IL-1 β in stroke patients is limited by an increased risk of infections.⁴⁷ Therefore, we sought for alternative options by blocking the migration of pro-inflammatory myeloid cells to secondary organs using the dual C-C chemokine receptors type 2 and 5 antagonist Cenicriviroc (CVC), which has been developed and proven safe for HIV infections and for steatohepatitis.^{48–50} We found that daily treatment with CVC after experimental stroke substantially reduced monocyte recruitment to the heart (**Fig. 7J, K**, Fig. S7F, G). This effect is likely attributable to blocking the chemokine-dependent invasion of

monocytes to secondary organs, because CVC increased circulating Ly-6C^{high} monocyte counts and had no direct cytotoxic effect on monocytes (Fig. S7H, I). Consequently, CVC treatment significantly reduced *Mmp9* expression by cardiac monocytes/macrophages and reduced cardiac fibrosis (**Fig. 7L, M**, Fig. S7J). Importantly, this therapeutic reduction in inflammatory cardiac ECM remodeling by CVC also significantly improved diastolic cardiac function in the chronic phase after stroke to comparable levels of control mice without a stroke (**Fig. 7N**). In summary, these results demonstrate the therapeutic potential of blocking the BM-to-heart migration of pro-inflammatory programmed monocytes as a strategy to prevent secondary cardiac comorbidity following stroke.

DISCUSSION

Systemic inflammation following a stroke has been identified as a critical factor affecting the short- and long-term prognosis of stroke patients.^{51,52} Interestingly, many of the pre-existing or acquired health conditions that arise after a stroke share common inflammatory mechanisms. These mechanisms can potentially exacerbate the development of other medical complications, leading to a worsened long-term outcome. Consequently, addressing systemic inflammation has emerged as a novel focus for translational research, with initial clinical trials already conducted to minimize functional disabilities in patients and prevent secondary complications.³

Our study reveals that stroke triggers persistent inflammation in multiple organs by inducing innate immune memory. Specifically, we discovered that IL-1 β -mediated epigenetic changes in the myeloid compartment play an unrecognized role in cardiac fibrosis, leading to diastolic dysfunction following ischemic brain injury.

Cardiovascular diseases, such as atrial fibrillation, valvular heart disease, and congestive heart failure, are well-known risk factors for ischemic stroke.^{53,54} However, this relationship is bidirectional, as the incidence of cardiovascular disorders also increases after an initial stroke.^{55,56} After a stroke, more than 60% of patients experience electrocardiographic (ECG) abnormalities,⁹ 25% are diagnosed with serious arrhythmias,⁵⁷ and approximately 19% develop at least one significant cardiac adverse event.¹⁰ Interestingly, a previous report demonstrated a causal role of monocytes to the development of atrial arrhythmias.²⁷ Previous studies in mice have demonstrated that stroke results in chronic systolic dysfunction lasting up to 8 weeks after the brain injury, leading to a delayed reduction in left ventricular ejection fraction and an increase in left ventricular volume.^{58,59} The SICFAIL study, a prospective clinical study involving 696 stroke patients, demonstrated a surprisingly high incidence of cardiac dysfunction after stroke. Diastolic dysfunction was found to be the most prevalent type of cardiac dysfunction, affecting 23% of patients without signs of systolic dysfunction.⁶⁰ This study clearly highlights the previously unrecognized burden of secondary cardiac dysfunction following ischemic stroke. Although diastolic dysfunction is highly prevalent, it is not routinely assessed in stroke patients^{61,62} and its clinical relevance in patients with acute ischemic stroke is not well understood. In our study – investigating a small subgroup of the SICFAIL cohort – we observed that in principle progressive diastolic dysfunction can also

occur in stroke patients, similar to our experimental stroke model. Similarly, we demonstrated in a cohort of autopsy samples the development of cardiac fibrosis after stroke.

Patients with chronic systemic inflammatory diseases, such as rheumatoid arthritis, psoriasis, or psoriatic arthritis, are known to have an increased risk of cardiovascular disease. For example, a recent population-based cohort study described an increased incidence of cardiovascular disease in patients with inflammatory bowel disease even in the absence of common risk factors like obesity, lipid disturbances, or hypertension, suggesting that inflammation may be a key factor underlying the development of these cardiovascular complications.^{18,63} Therefore, it is reasonable to consider that the systemic inflammatory response triggered by the ischemic brain lesion itself may further predispose stroke patients to secondary (inflammatory) vascular events.

Here, we demonstrate that persistent pro-inflammatory changes in myeloid cells after stroke are a causal factor for the development of cardiac fibrosis independent of other predisposing factor for cardiovascular disorders. Innate immune memory—defined as long-term changes in the innate immune cell compartment that alters its responsiveness to a second stimulation—has so far been described in infection models and in vaccination,¹³ but was so far not recognized as a pathogenic mechanism after sterile tissue injuries including stroke. Importantly, innate (trained) immunity to a pathogen not only heightens innate immune responsiveness to the same pathogen but was demonstrated to also affect unrelated inflammatory processes, as for example the disease-modifying effect of periodontitis for atherosclerosis progression.¹⁷ In this study, we make the observation of innate immune memory in response to a sterile tissue injury, which links this acute event to the development of a chronic, secondary pathology at a remote organ site.

Our study highlights IL-1 β -mediated epigenetic changes and the recruitment of reprogrammed cells to the healthy heart as critical events in the development of chronic secondary organ dysfunction after a stroke. Notably, epigenetic changes induced by the acute surge of IL-1 β post-stroke are comparable to the observed epigenetic modifications in previous studies using infection models.^{64,65} Based on our findings, targeting IL-1 β systemically can potentially prevent post-stroke epigenetic changes and the resulting pro-inflammatory effects on remote organ homeostasis. This aligns well with previous research demonstrating the cardiovascular benefits observed in the CANTOS trial using anti-IL-1 β therapy.⁴⁷ However, the trial also revealed significant risks of increased infection rates

associated with this non-specific approach that targets a key pro-inflammatory cytokine involved in pathogen clearance. This limitation poses a challenge for the further development of this approach in translational research.

Therefore, in our study, we explored an alternative strategy to limit the recruitment of monocytes from BM and circulation to remote organs by using a dual chemokine inhibitor targeting CCR2/5 (Cenicriviroc).⁴⁸ Notably, genetic studies have provided evidence of the involvement of CCL2-CCR2 signaling in various cardiovascular disorders, suggesting that targeting this signaling pathway could have beneficial effects on monocyte recruitment.⁶⁶ Moreover, Cenicriviroc has demonstrated safety and efficacy in other conditions, including HIV and hepatosteatosis.^{48–50}

In conclusion, our study provides mechanistic insights into immune-mediated secondary comorbidities following stroke, such as cardiac dysfunction and potentially others. We have identified innate immune memory as a causal mechanism underlying chronic changes in resident innate immune cells across multiple organs, which contribute to the development or progression of secondary organ dysfunction. These discoveries offer a therapeutic rationale for the secondary prevention of post-stroke comorbidities.

Limitations of the study.

There are several limitations to our study. While our results propose IL-1 β as a principal mediator of trained immunity and its significance for cardiac pathology after stroke, we did not test in this study the generalizability of this IL-1 β -mediated pathway to other conditions of acute tissue injury or infection models. Also, the exact molecular mechanisms by which IL-1 β induces epigenetic changes and altered hematopoiesis remain unclear, including the intracellular mechanisms as well as potential effects on structural BM organization and interaction of HSC with stromal cells. Similarly, the effects of stroke on long-term myelopoiesis and trained immunity in humans is so far unknown. In relation to the cardiac phenotype of diastolic dysfunction and delayed cardiac fibrosis after stroke, this phenotype remains to be validated in human stroke patients in a prospective clinical study; also, a potential mechanistic relationship between early systolic and later diastolic cardiac dysfunction remains so far unexplored. Our study found no indications for a direct effect of changes in the autonomic nervous system on post-stroke trained immunity or chronic diastolic dysfunction although we cannot exclude a contribution of the autonomic nervous system on

myelopoiesis, structural remodeling of BM stromal cells or other peripheral immune compartments (e.g. the spleen and intestine), that might indirectly contribute to the phenotype observed in the chronic phase post-stroke.

Acknowledgments

The authors thank Christina Fürle and Kerstin Thuß-Silczak for excellent technical support and Burkhardt Becher (University of Zurich) for providing Ccr2^{creERT2}xAi14 mice. The study was supported by the Vascular Dementia Research Foundation, the European Research Council (ERC-StG 802305), the German Research Foundation (DFG) under Germany's Excellence Strategy (EXC 2145 SyNergy – ID 390857198 and EXC2151 ImmunoSensation – ID 390873048), through FOR 2879 (ID 405358801), CRC 1123 (ID 238187445), TRR 274 (ID 408885537), TRR 355 (ID 490846870), TRR 332 (INST 211/1066-1), a Walter-Benjamin Fellowship (SI 2832/1), the Corona Foundation (S199/10079/2019), the Munich School for Data Science (MUDS) and the China Scholarship Council and the UNION-CVD clinician scientist programme (ID 413657723). The SICFAIL study was funded by the German Ministry of Research and Education (Comprehensive Heart Failure Centre Würzburg, BMBF #01EO1004 and #01EO1504).

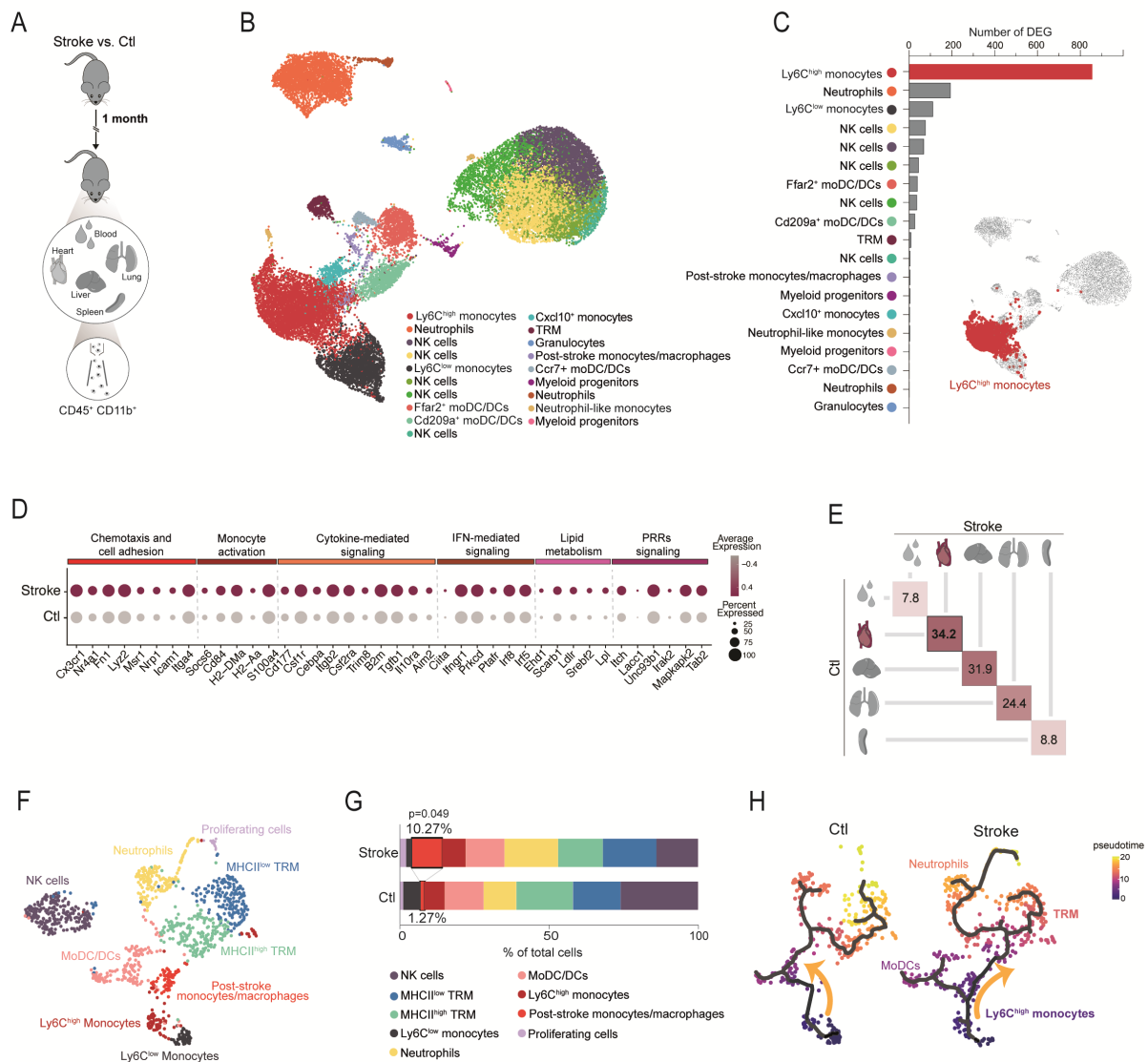
Author contributions

Conceptualization, A.S., A.L.; Investigation, A.S., S.Z., J.C., D.M., C.F., O.C.; S.B., A.S.C., F.A.M., P.U.H., A.R., S.R., G.L., R.S., Y.C., C.M.; Formal Analysis, A.S., S.Z., F.C., A.S.C., S.B.G, H.S., E.B., S.R., G.L., F.A.M., P.U.H.; Resources, C.B., K.H., S.F., N.P., O.G., E.B., C.S., B.B., S.C.; Writing – Original Draft, A.S., S.Z., A.L.; Writing – Review & Editing, A.S., M.D., P.H., S.C., F.A.M., P.U.H., B.B., C.S., A.L.; Visualization, A.S., S.Z., F.C., B.B., A.L.; Supervision: S.C., B.B., C.S., A.L.; Funding Acquisition: S.C., B.B., C.S., A.L.

Declaration of interests

All authors declare no competing interests.

Figure 1

**Figure 1. Stroke induces long-term inflammatory changes in systemic monocytes/macrophages.**

(A) Myeloid cells were sorted from blood and peripheral organs 1 month after experimental ischemic stroke (n=4/group) for single-cell mRNA sequencing. (B) UMAP plot of 29,124 CD45⁺ CD11b⁺ cells, colored by identified clusters. (C) Number of differentially expressed genes (DEG) between conditions per identified population (adj. p value < 0.05). Ly6C^{high} monocytes show the highest number of DEG (857 genes). (D) Expression levels of selected genes in the Ly6C^{high} monocytes highlighted in (C) and selected from the enriched GO terms in the set of DEG between conditions (adj. p value < 0.1). The dot size corresponds to the fraction of cells within each condition and the color indicates average expression. (E) Euclidean distances in the PCA space between the stroke and control per organ. The PCA was calculated from a total of 18,834 genes identified in all CD45⁺CD11b⁺ cells. (F) UMAP plot of 1,117 CD45⁺ CD11b⁺ cells from the heart, colored by identified populations and (G) stacked bar graph for percentage of identified population per condition (chi-square test). (H) Monocle3

pseudo-temporal ordering of CD45⁺ CD11b⁺ cells from the heart superimposed on the UMAP plot and split by condition. Cells are colored based on their progression along pseudo-temporal space.

Figure 2

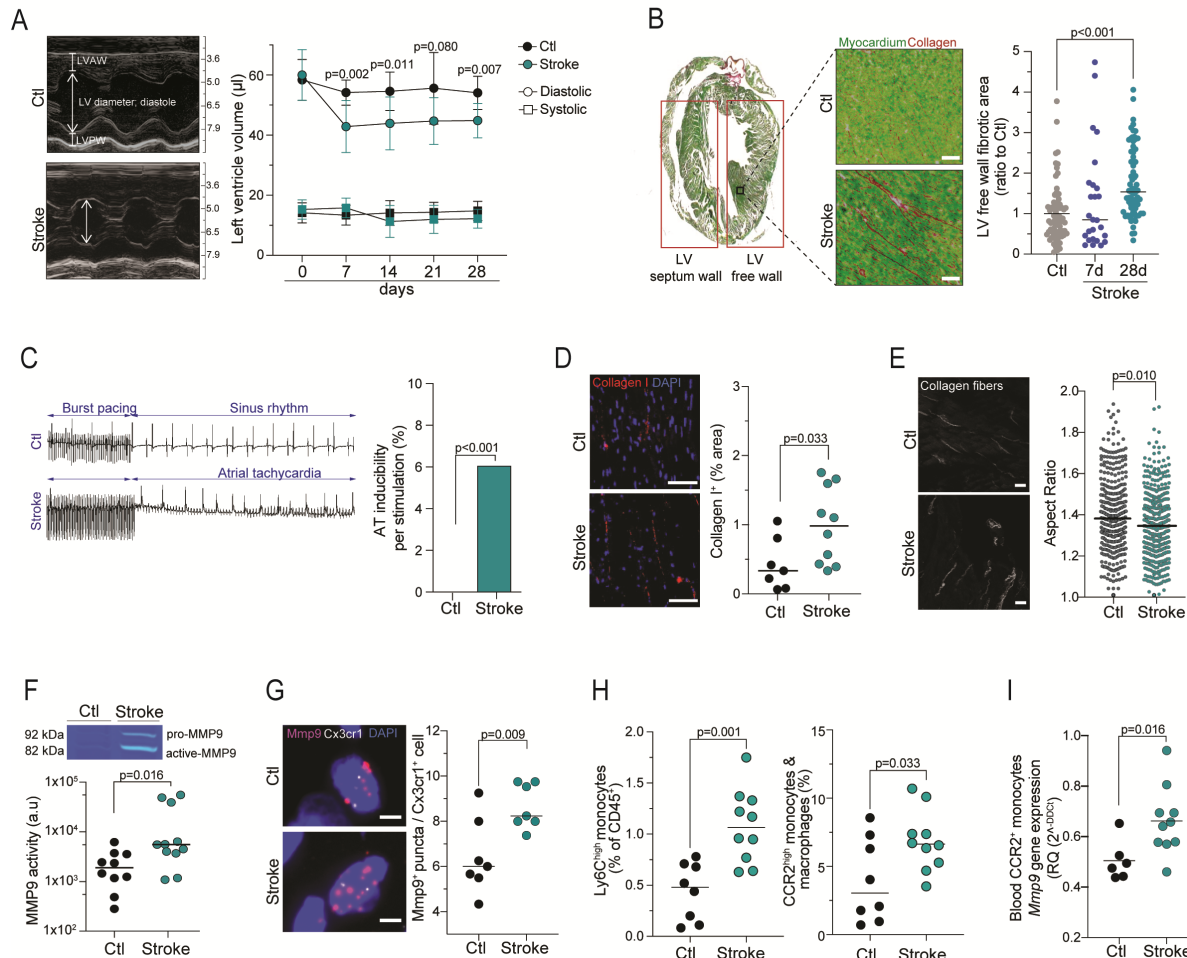


Figure 2. Stroke results in chronic cardiac diastolic dysfunction and inflammatory cardiac remodeling. (A) Representative ultrasound images (M-mode) performed at indicated time points (n = 12(stroke)/6(control)) and quantification of the left ventricle (LV) volume in systole (squares) and diastole (circles). LVAW: Left ventricle anterior wall; LVPW: left ventricle posterior wall. (B) Representative images (Sirius red/Fast green staining) and quantification of cardiac fibrosis in the LV free wall (t test, n=7/10 per group, 4 independent sections per mouse). (C) Representative image of cardiac electrophysiology at 1 month after stroke or control (n=7/group) and quantification of inducibility of atrial tachycardia (AT). (D) Representative image and quantification of collagen I content, expressed in percentage of total area of the LV free wall (scale bar = 50 μ m; t test, n = 8/10 per group). (E) Representative second harmonic generation (SHG) images for the detection of the organization of fibrillar collagen and quantification of the Aspect ratio (scale bar = 20 μ m; nested t test, n = 9/10 mice per group, 35-50 images per mouse heart). (F) Enzymatic MMP9 activity using gel zymography of heart samples one month after stroke or control (U test, n = 10/11 per group). (G)

Representative images of single molecule fluorescence *in situ* hybridization (smFISH) and quantification of the number of *Mmp9* mRNA puncta per *Cx3cr1*⁺ cell (scale bar = 5 μ m; t test, n = 7 per group). **(H)** Quantification of flow cytometry for Ly6C^{high} monocytes (CD45⁺ Ly6G⁻ CD11b⁺ F4/80⁻ Ly6C^{high}) and CCR2^{high} monocytes/macrophages (CD45⁺ Ly6G⁻ CD11b⁺ F4/80⁺ CCR2^{high}) in the heart one month after stroke or control (t test; n=8/10 per group). **(I)** *Mmp9* mRNA expression (RT-qPCR) in sorted blood CCR2⁺ monocytes relative to *Ppia* expression and normalized to control (U test, n=6/10 per group).

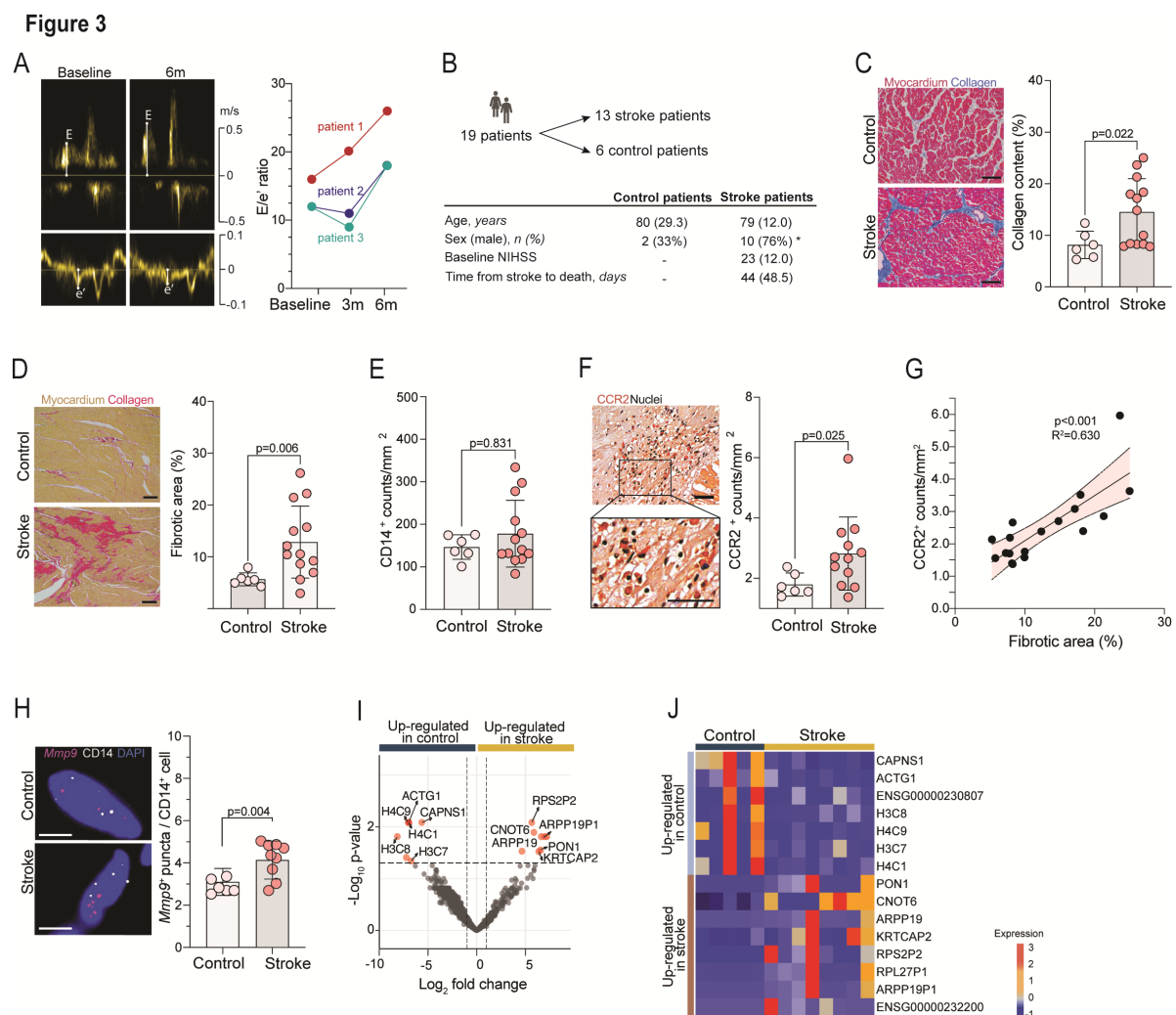


Figure 3. Stroke increases cardiac fibrosis and monocyte accumulation in patients. **(A)** Representative images of the patient with chronic diastolic dysfunction recruited by the Stroke Induced Cardiac FAILURE study (SICFAIL) consortium. Corresponding quantification of the E/e' of 3 patients identified with chronic diastolic dysfunction. **(B)** Myocardial autopsy samples were collected from a total of 19 patients: 12 ischemic stroke (IS) patients and 7 controls, who died without cardiac or brain disorder (confirmed by autopsy). Basic demographical and clinical characteristics are depicted. Data is expressed as median (IQR), unless stated otherwise. *p<0.05 (chi-square test). **(C)**

Representative images (Masson Trichrome staining, scale bar = 0.1 mm) and quantification of collagen content (t test). **(D)** Representative images (Sirius red/Fast green staining, scale bar = 0.2 mm) and quantification of the collagen content expressed as percentage of total cardiac area (t test). **(E)** Quantification of CD14⁺ cells (t test). **(F)** Representative image (scale bar = 0.05 mm) and quantification (t test) of CCR2⁺ cells. **(G)** Correlation of CCR2⁺ cell counts with cardiac fibrosis (Masson Trichrome staining, Pearson correlation test). **(H)** Representative images and quantification of single molecule fluorescence *in situ* hybridization (smFISH) for the detection of *Mmp9* mRNA puncta expression in CD14⁺ cardiac cells from stroke and control patients (scale bar = 5 μ m; t test, n = 7/9 per group). **(I)** Volcano plot showing regulated genes in the myocardium between IS and control patients. Colored genes are p<0.05. **(J)** Heatmap showing the TOP differentially expressed genes in the heart between IS and control patients.

Figure 4

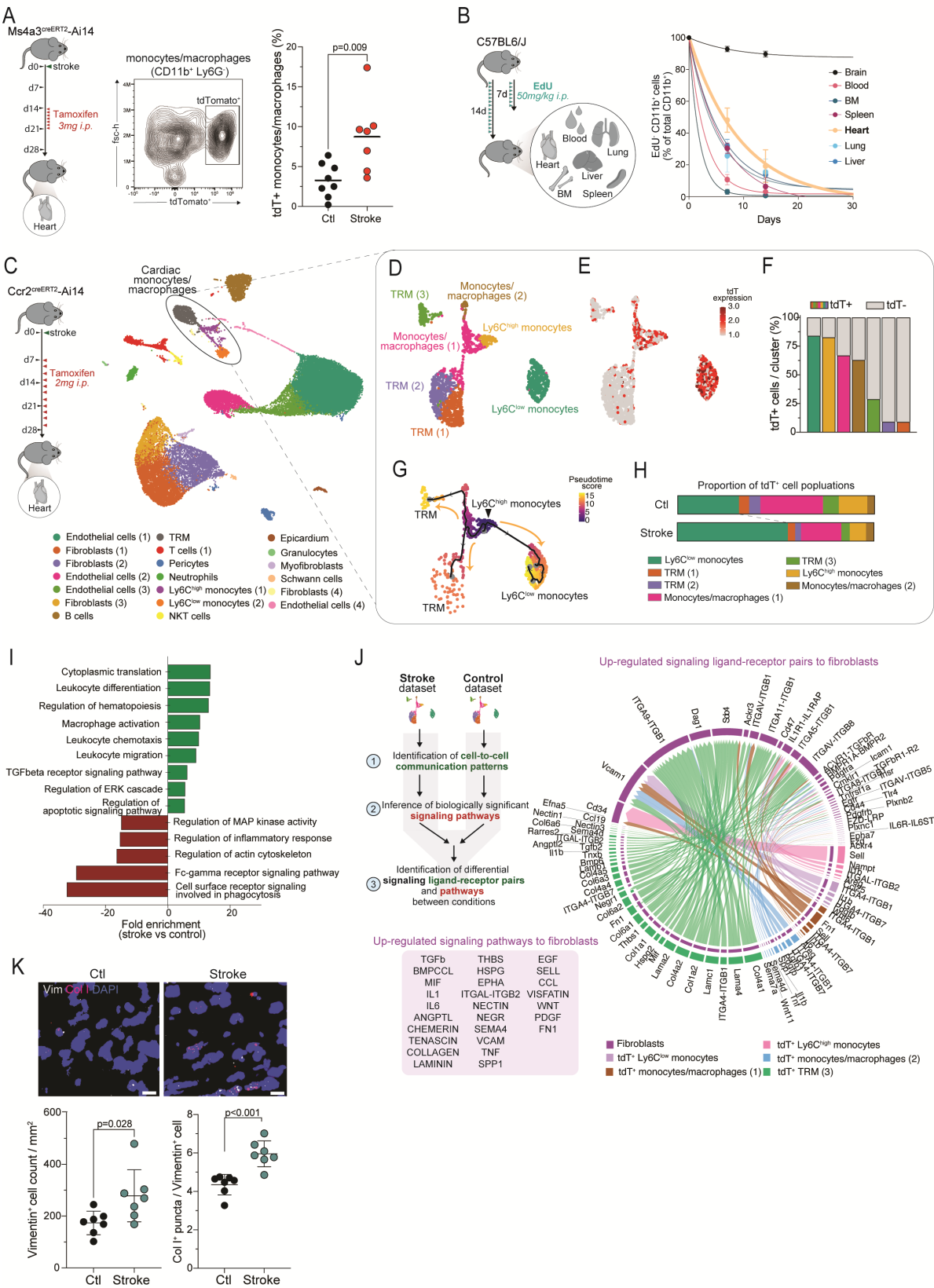


Figure 4. Stroke promotes chronic monocyte recruitment into the heart. (A) Ms4a3^{creERT2}-Ai14 stroke and control mice were daily administered with Tamoxifen for 7 consecutive days from day 14 after stroke. Cardiac myeloid cells were analyzed by flow cytometry one month after stroke or control

(n=7/8 per group). Representative gating strategy for the tdTomato (tdT⁺) cardiac monocytes/macrophages (CD45⁺ Ly6G⁻ CD11b⁺, mid panel) and quantification of tdT⁺ cardiac monocytes/macrophages (right panel). **(B)** Mice were daily administered with EdU for 7 or 14 days after stroke. Lineage negative myeloid cells from the blood, and peripheral organs were analyzed by flow cytometry for percentage of EdU⁺ CD11b⁺ cells per timepoint (n=6/7 per organ). **(C)** CCR2^{creERT2}-Ai14 reporter mice received Tamoxifen every second day from day 7 after stroke or control surgery until one month and cardiac interstitial cells analyzed using single-cell mRNA sequencing (n=2 mice/group). UMAP plot of a total of 34,927 cardiac interstitial cells, colored by identified clusters and **(D)** UMAP plot of the cardiac monocytes/macrophages subsets. **(E)** UMAP plot showing the expression of tdT within the cardiac monocytes/macrophages. **(F)** Percentage of tdT⁺ cells per cell subset. **(G)** Monocle3 pseudo-temporal ordering of tdT⁺ cardiac monocytes/macrophages superimposed on the UMAP plot. Cells are colored based on their progression along pseudo-temporal space. **(H)** Stacked bar graph for percentage of cells per population. **(I)** Pathway analysis for tDEGs between conditions in tdT⁺ cardiac monocytes/macrophages. Biological processes were grouped and sorted by p value. **(J)** Schematic design of cell-cell interaction analysis (left upper panel) and chord plot showing up-regulated ligand-receptor pairs from tdT⁺ cardiac monocytes/macrophages populations to fibroblasts after stroke. List of up-regulated signaling pathways from tdT⁺ cardiac monocytes/macrophages populations to fibroblasts after stroke. **(K)** Representative images and quantification of single molecule fluorescence *in situ* hybridization (smFISH) for the detection of the count of *Vimentin*⁺ cardiac fibroblasts and the *Collagen I* mRNA expression in *Vimentin*⁺ fibroblasts one month after stroke or control (scale bar = 5 μ m; t test, n = 7/group).

Figure 5

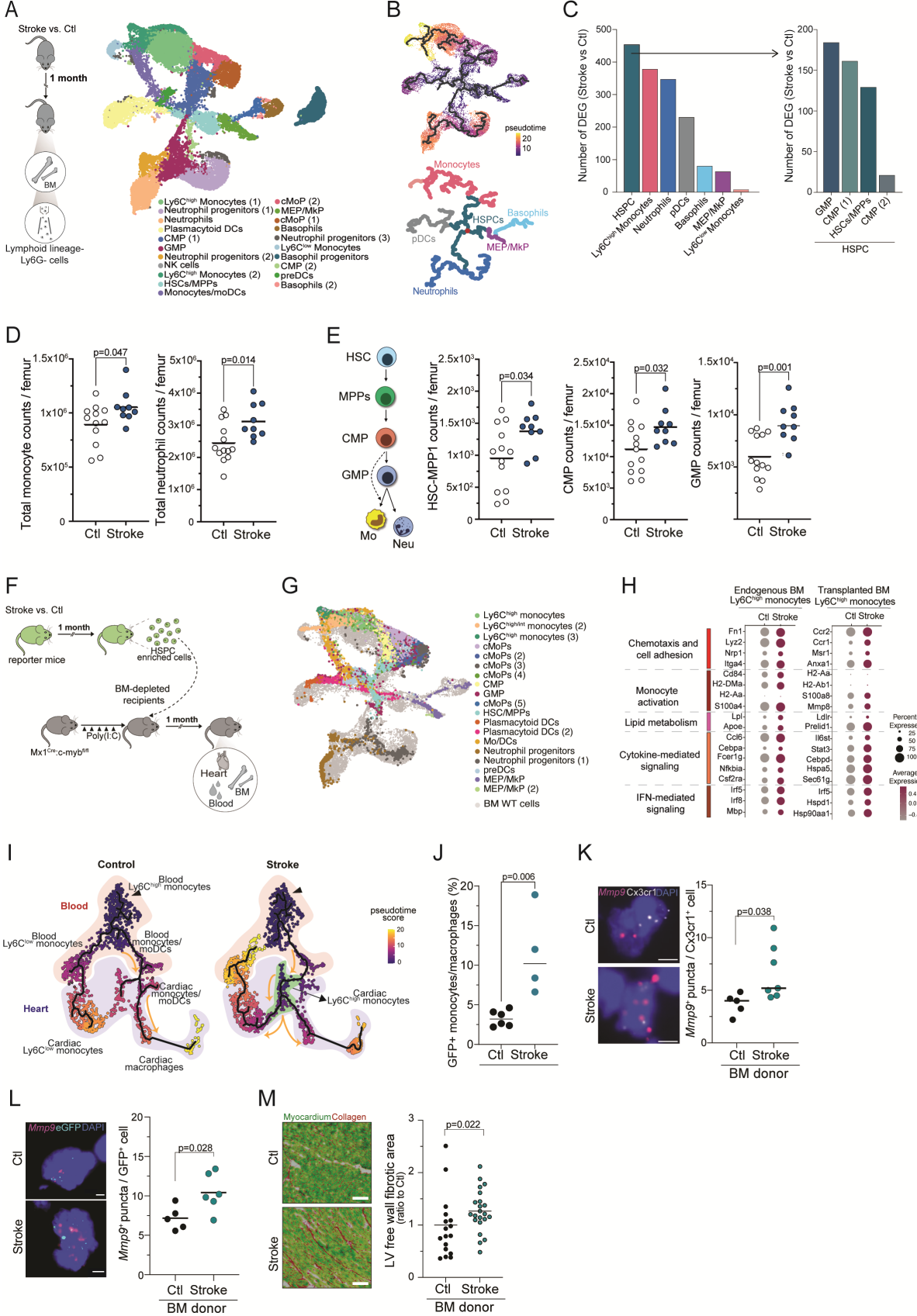


Figure 5. Stroke induces persistent innate immune memory. (A) Schematic experimental design: lymphoid lineage- (CD3, CD4, CD8a, CD19 and Ter119) and neutrophil- (Ly6G) negative myeloid

cells were sorted from the BM of control and stroke mice one month after stroke (n=8) for single-cell mRNA sequencing. UMAP plot of the 22,169 myeloid cells sorted from the BM of control and stroke mice. **(B)** Monocle3 pseudo-temporal ordering of myeloid BM cells, superimposed on the UMAP plot. Cells are colored based on their progression along pseudo-temporal space (left panel) or by cell types (right panel). **(C)** Number of differentially expressed genes (DEG) between conditions per cell type (adj. p value <0.05). **(D)** Quantification of monocyte and neutrophil cell counts between conditions (U-test; n=9/13 per group). **(E)** Schematic of the differentiation path of hematopoietic stem cells (HSC) towards monocytes (Mo) and neutrophils (Neu) (left panel) and quantifications of HSC-multipotent progenitors 1 (MPP1), common myeloid progenitors (CMP) and granulocyte-monocyte progenitors (GMP) (U-test; n=9/13 per group). **(F)** Schematic experimental design: bone marrow (BM) cells enriched for HSPCs were isolated from stroke and control actin-GFP mice and transplanted into BM-depleted $Mx1^{Cre};c-myb^{fl/fl}$ mice. One month after transplantation, mice were sacrificed and GFP-positive myeloid cells from BM, blood and heart were isolated and analyzed using single-cell mRNA sequencing and flow cytometry. **(G)** UMAP plot of 25,358 myeloid GFP⁺ cells from the BM of transplanted mice, colored by identified populations and superimposed on the UMAP plot of the myeloid cells from the endogenous BM (cells in gray, Fig. 5A for reference). **(H)** Dot plot showing the expression of selected genes in the Ly6C^{high} monocytic populations from the endogenous BM of stroke and control mice (left column) and the BM of recipient mice transplanted with stroke and control GFP⁺ HSPC-enriched BM cells (right column). Genes were selected from the enriched GO terms in the set of DEG between conditions in Ly6C^{high} monocytes (adjusted p value<0.1). The dot size corresponds to the fraction of cells within each condition and the color indicates average expression. **(I)** Monocle3 pseudo-temporal ordering of GFP⁺ cells from recipient mice, superimposed on the UMAP plot and split by condition. Cells are colored based on their progression along pseudo-temporal space. **(J)** Quantification of the flow cytometry analysis of GFP⁺ cardiac monocytes/macrophages from recipient mice transplanted with stroke or control BM cells. **(K, L)** Representative images for single molecule fluorescence *in situ* hybridization (smFISH) (left, scale bar = 5 μ m) and quantification of the number of *Mmp9* puncta per *Cx3cr1*⁺ cardiac cells (**K**; U test, n=5/7 per group) and GFP⁺ cardiac cells (**L**; U test, n=5/6 per group). **(M)** Representative images (Sirius red/Fast green staining) and quantification of cardiac fibrosis in the left ventricle (LV) free wall of recipient mice (t test, n=5/7 per group, 3/4 heart sections per mouse).

Figure 6

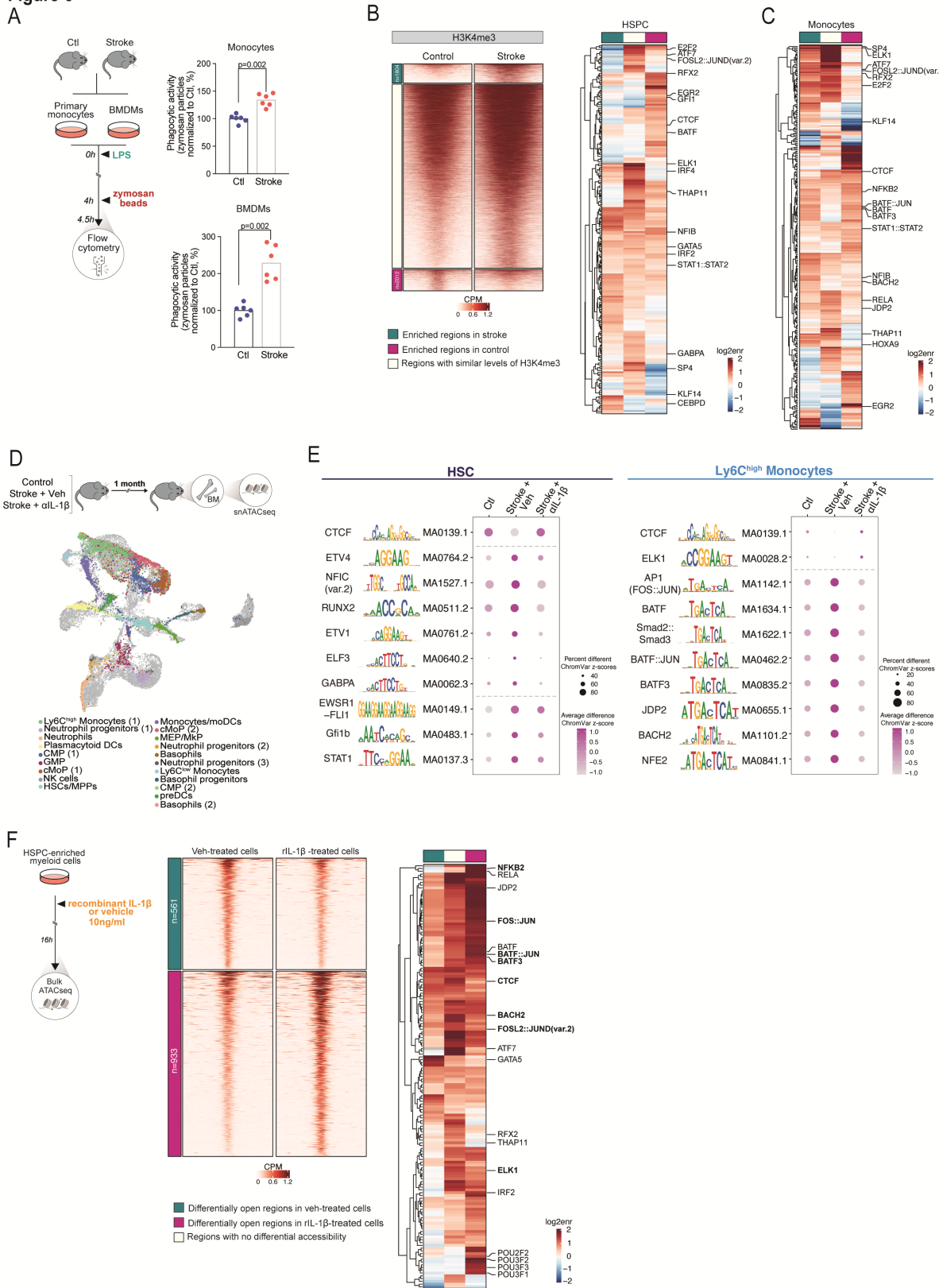


Figure 6. Innate immune memory is mediated by early post-stroke IL-1 β secretion. (A) Schematic experimental design: bone marrow-derived macrophages (BMDM) and primary monocytes were isolated from mice one month after stroke or control. Uptake of zymosan beads was quantified by flow cytometry (t test, n=6 per group). **(B)** Density heatmaps for enriched H3K4me3 peaks in

lymphoid lineage- (CD3, CD4, CD8a, CD19 and Ter119) and neutrophil- (Ly6G) negative myeloid cells from mice one-month post-stroke (up, green) or control mice (down, pink), split by condition. Heatmap of motif enrichment for H3K4me3 peaks for HSPCs between mice one-month post-stroke and control mice and **(C)** corresponding heatmap for Ly6C^{high} monocytes. **(D)** Schematic experimental design: mice received Interleukin (IL)-1 β neutralizing antibodies or vehicle 1h before and 1h after stroke induction. One month later, nuclei were isolated from lineage-negative myeloid cells (n=3/group) for single-nuclei ATAC-sequencing. UMAP plot of 13,520 myeloid nuclei, colored by identified populations and superimposed on the UMAP plot of the myeloid cells from the endogenous BM of control and stroke mice (cells in gray, Fig. 5A). **(E)** Dot plot showing per-cell differential motif activity scores between experimental conditions in HSC (left panel) and Ly6C^{high} monocytes (right panel). Identified motifs with the highest and lowest activity scores between control and vehicle-treated strokes are represented (adj. p value <0.05). **(F)** Schematic experimental design: HSPC-enriched myeloid cells were cultured with either recombinant (r)IL-1 β or vehicle for 16h, and analyzed by ATAC sequencing (left panel). Density heatmaps for differentially open chromatin regions split by condition (middle panel). Heatmap of motif enrichment for differentially accessible peaks between groups (right panel).

Figure 7

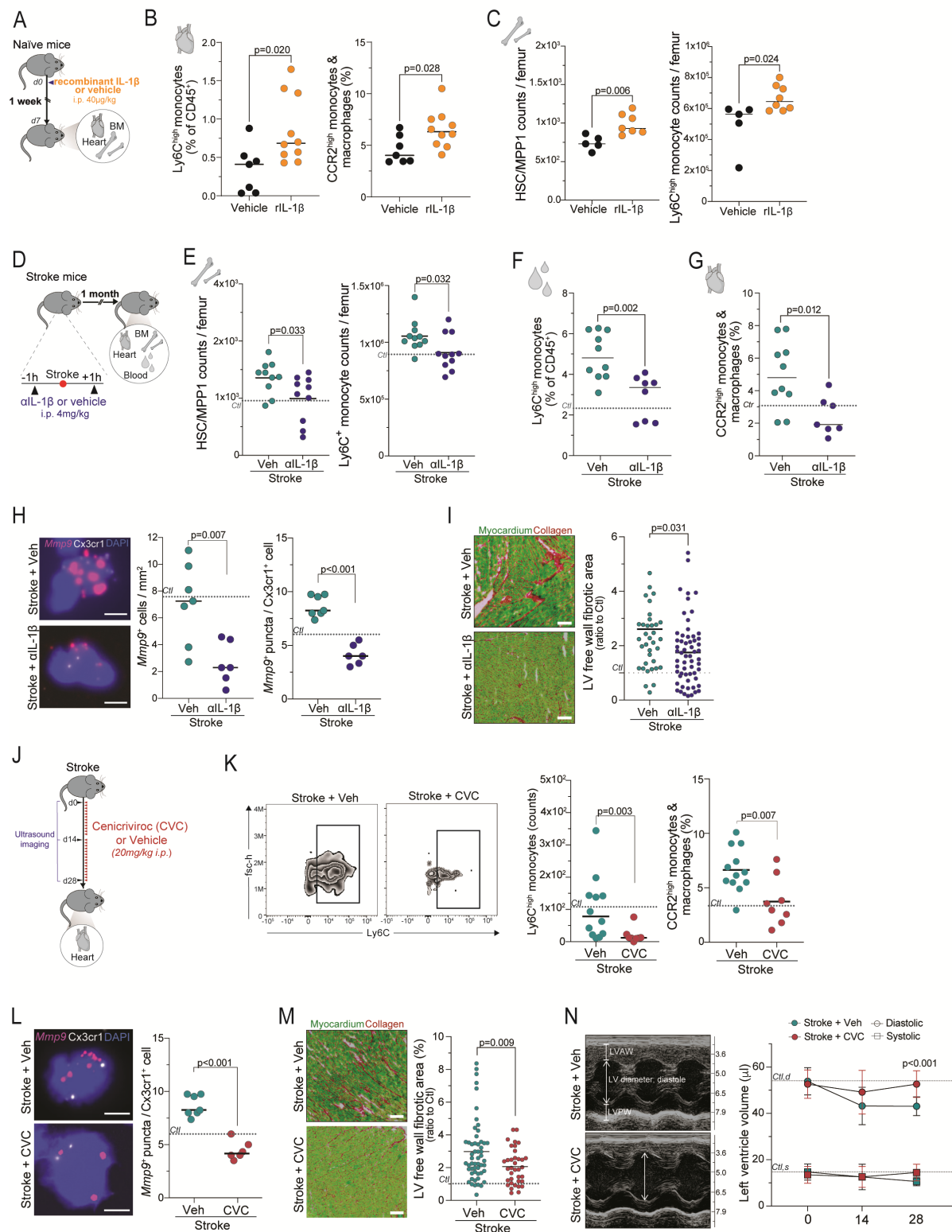


Figure 7. IL-1 β -driven innate immune memory mediates cardiac dysfunction after stroke. (A) Schematic experimental design: naive WT mice received rIL-1 β or vehicle intraperitoneally (i.p.) and organs collected 7d later for flow cytometry. **(B)** Quantification of Ly6C^{high} monocytes (CD45⁺ Ly6G⁻ CD11b⁺ F4/80⁻ Ly6C^{high}) and CCR2^{high} monocytes/macrophages (CD45⁺ Ly6G⁻ CD11b⁺ F4/80⁺ CCR2^{high}) between groups (t test, n=7/10 per group). **(C)** Quantification of HSC-multipotent

progenitors 1 (HSC-MPP1) and Ly6C^{high} monocytes in BM (t test, n=5/8 per group). **(D)** Schematic experimental design: mice received IL-1 β -specific neutralizing antibodies or vehicle 1h before and 1h after stroke induction and organs collected for analysis one month later. **(E)** HSC-multipotent progenitors 1 (HSC-MPP1) and total monocytes in BM from stroke mice (U-test; n=10/11 per group) and **(F)** Ly6C^{high} monocytes (CD45⁺ Ly6G⁻ CD11b⁺ Ly6C^{high}) in blood (t-test; n=10/8 per group) and **(G)** CCR2^{high} monocytes/macrophages (CD45⁺ Ly6G⁻ CD11b⁺ F4/80⁺ CCR2^{high}) in hearts (t-test; n=10/7 per group). **(H)** Representative images and quantification of *Mmp9* mRNA expression in *Cx3cr1*⁺ cardiac myeloid cells between treatment groups by single molecule fluorescence in situ hybridization (smFISH, scale bar = 5 μ m, U test, n=6/7 per group). **(I)** Representative images (Sirius red/Fast green staining) and quantification of cardiac fibrosis in the left ventricle (LV) free wall (t test, n=8/14 per group, 4 heart sections per mouse). **(J)** Schematic experimental design: Stroke mice were administered daily with the dual C-C chemokine receptors type 2 and 5 antagonist Ceniviroc (Stroke+CVC) or vehicle (Stroke+Veh) for 28 days. Cardiac ultrasound imaging was performed at day 0, 14 and 28. Hearts were collected at 28d for flow cytometry and histological analysis. **(K)** Gating strategy for Ly6C^{high} monocytes in CVC- and vehicle-treated stroke mice and corresponding quantification (U-test; n=8-12 per group). **(L)** Representative smFISH images and quantification of the number of *Mmp9* puncta per *Cx3cr1*⁺ cardiac myeloid cell (U test, n=6/7 per group). **(M)** Representative images (Sirius red/Fast green staining) and quantification of cardiac fibrosis in the LV free wall in CVC- and vehicle-treated stroke mice. Dashed line indicates mean percentage of fibrotic area in control mice (t test, n=9/14 per group, 4 heart sections per mouse). **(N)** Representative ultrasound images (M-mode) performed at day 0, 14 and 28 after stroke on CVC- and vehicle-treated stroke mice (left panel). Quantification of the left ventricle (LV) volume in systole (squares) and diastole (circles). Dashed line indicates mean LV volume in control mice at day 28. Multiple t tests, n=6/12 per group. LVAW: Left ventricle anterior wall; LVPW: left ventricle posterior wall.

Figure S1

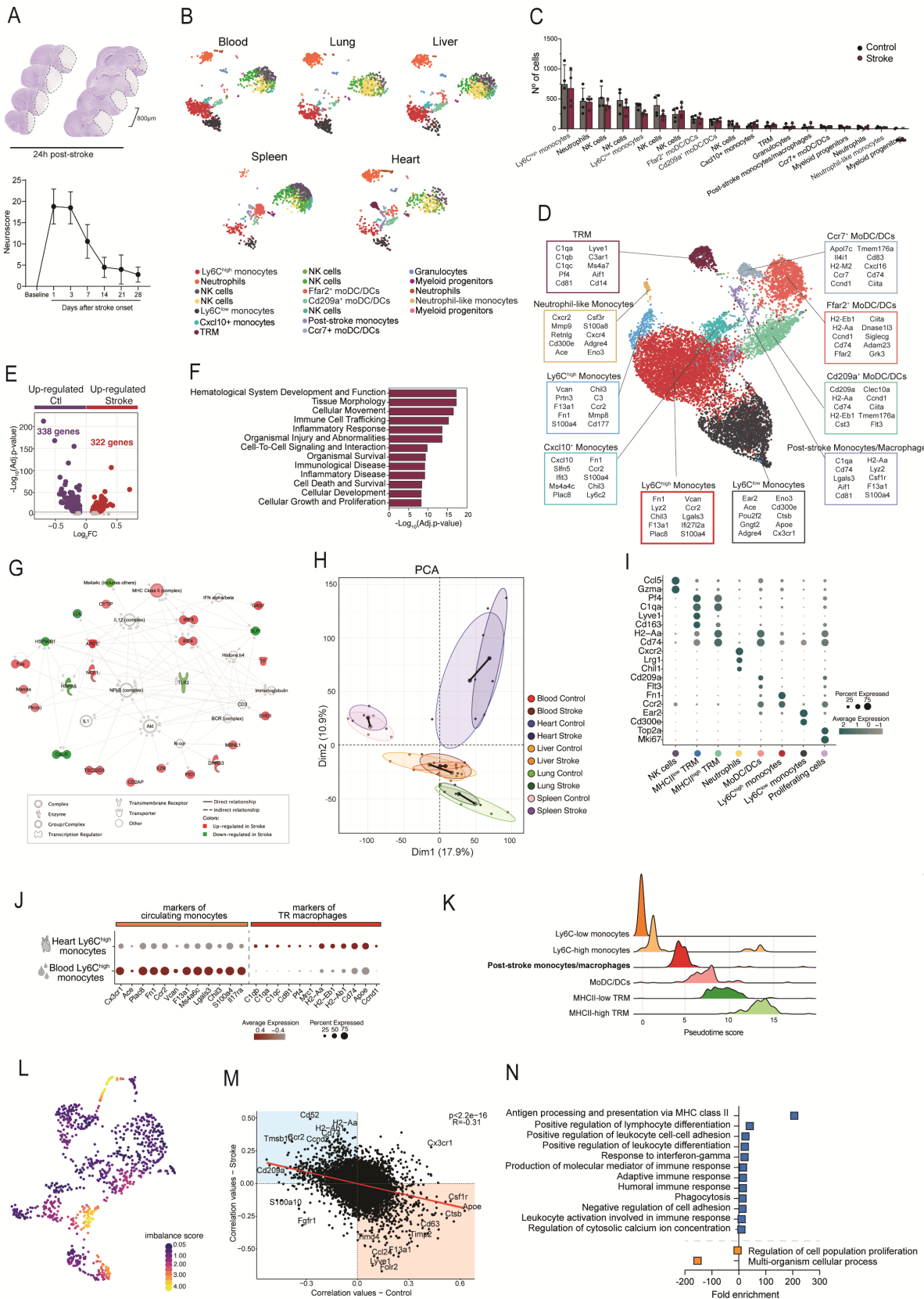


Figure S1. Stroke induces long-term inflammatory changes in monocytes/macrophages from peripheral organs, related to Figure 1. (A) Representative images of ischemic stroke lesions from the transient middle cerebral artery occlusion (tMCAo) stroke mouse model (upper panel). Graph

showing the neurological deficits of mice over time after stroke, assessed by the Neuroscore test. **(B)** Uniform manifold approximation and projection (UMAP) plots of a representative set of 1,000 CD45⁺ CD11b⁺ cells per peripheral organ, colored by identified populations. **(C)** Number of cells per identified population, split by condition. **(D)** UMAP plot of the monocytes and macrophages clusters identified in peripheral organs, annotated with key expressed genes per population. **(E)** Volcano plot showing the up (322 genes, red) and down-regulated genes (338 genes, purple) of Ly6C^{high} monocytes from stroke and control mice. Colored genes are $p < 0.05$ and $|\text{fold-change}| > 1.25$. **(F)** Pathway analysis was performed using Ingenuity Pathway Analysis (IPA, Qiagen) using the DEG from Ly6C^{high} monocytes, with an adjusted p value < 0.05 and $|\text{fold-change}| > 1.58$. Top diseases and functions categories sorted by p value are displayed. **(G)** Functional gene interaction network analysis using IPA. Genes are colored based on fold-change values determined by the single cell mRNA sequencing analysis, where red indicates an increase in stroke and green in control animals. **(H)** PCA plot displaying all analyzed samples from all peripheral organs. The PCA was calculated from a total of 18,834 genes identified in peripheral CD45⁺CD11b⁺ myeloid cells. The Euclidian distances between stroke and control clusters per organ are indicated in black lines. **(I)** Dot plot showing the expression profile of selected genes key for the identification of the cell populations in the heart. The dot size corresponds to the fraction of cells within each condition expressing the indicated transcript, and the color indicates average expression. **(J)** Dot plot showing the expression levels of selected gene features in Ly6C^{high} monocytes from the heart and blood. Genes were selected from the list of DEG between both cell populations. The dot size corresponds to the fraction of cells within each condition expressing the indicated transcript, and the color indicates average expression. **(K)** Ridge plots showing the pseudotime score distribution in each cell population identified in the heart. **(L)** UMAP plot showing the imbalance score. **(M)** Correlation values of the trajectory-driver genes between stroke and control conditions. **(N)** Pathway analysis using ShinyGO for differential trajectory-driver genes between stroke and control conditions.

Figure S2.

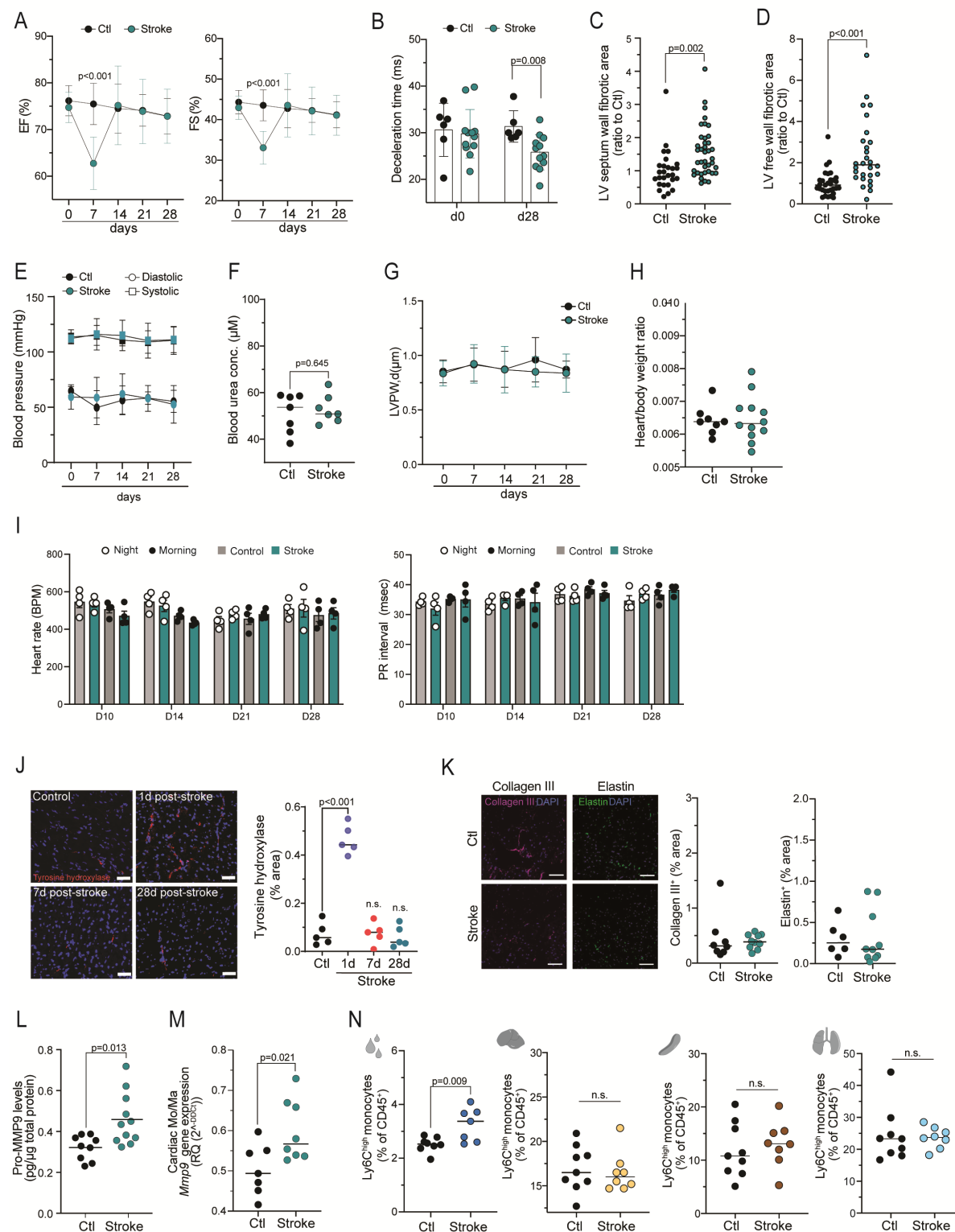


Figure S2. Stroke results in chronic cardiac diastolic dysfunction, related to Figure 2. (A) Quantification of the ejection fraction (EF, left panel) and fractional shortening (FS, right panel) at indicated time points (days) before (day 0) and after stroke, and control (U tests, $n=6/12$ per group). **(B)** Quantification of the transmitral deceleration time at day 0 and 28 in control and stroke mice (U tests, $n=6/12$ per group). **(C)** Quantification of cardiac fibrosis in the LV septum wall at 1m after

stroke and control (t test, n=7/10 per group, 4 heart sections per mouse). **(D)** Quantification of cardiac fibrosis in the LV free wall at 3m after stroke and control (t test, n=7/10 per group, 4 heart sections per mouse). **(E)** Quantification of the blood pressure at the indicated time points (days) before (day 0) and after stroke, and control conditions (n=3/8 per group). **(F)** Blood urea concentration was measured in mice one month after stroke or in control mice (t test, n=7 per group). **(G)** Quantification of the LV posterior wall thickness at the end of diastole (LVPW, d) at indicated time points (days) before (day 0) and after stroke, and control mice (U tests, n=6/12 per group). **(H)** Heart-body ratio was measured in mice one month after stroke and control mice (t tests, n=8/12 per group). **(I)** Quantification of heart rate (right panel) and PR interval (left panel) at indicated time points (days) after stroke and control, using continuous ECG telemetry (U tests, n=4 per group). Each timepoint include the measurement in the morning and at night. **(J)** Representative immunofluorescence images of the tyrosine hydroxylase (TH) in the heart at indicated time points (days) after stroke and control. DAPI was used as nuclear dye (left, scale bar = 50 μ m). Quantification of the TH content, expressed in percentage of total area of the LV free wall (right; t test, n = 5/group). **(K)** Representative images of immunofluorescence staining for the detection of collagen III and elastin in heart coronal sections (left; scale bar = 50 μ m). Corresponding quantification of collagen III and elastin content, expressed in percentage of total area of the LV free wall (right; t test, n = 8/10 per group). **(L)** Total pro-MMP9 protein levels were measured in heart samples from stroke and control mice. Pro-MMP9 protein levels are normalized to total protein content (U-test, n=9/11 per group). **(M)** RT-qPCR was performed on sorted monocyte/macrophages (Mo/Ma, CD45⁺Ly6G⁻CD11b⁺) to measure the expression levels of *Mmp9* mRNA, quantified relative to the expression of the housekeeping gene encoding for *Ppia* and normalized to control levels (U test, n=7 per group). **(N)** Quantification of the Ly6C^{high} monocytes (CD45⁺CD11b⁺Ly6G⁻Ly6C^{high}) in blood, liver, spleen and lung from mice one month after stroke and control mice, measured by flow cytometry and expressed as percentage of total CD45⁺ cells (t test, n=8/7 per group).

Figure S3.

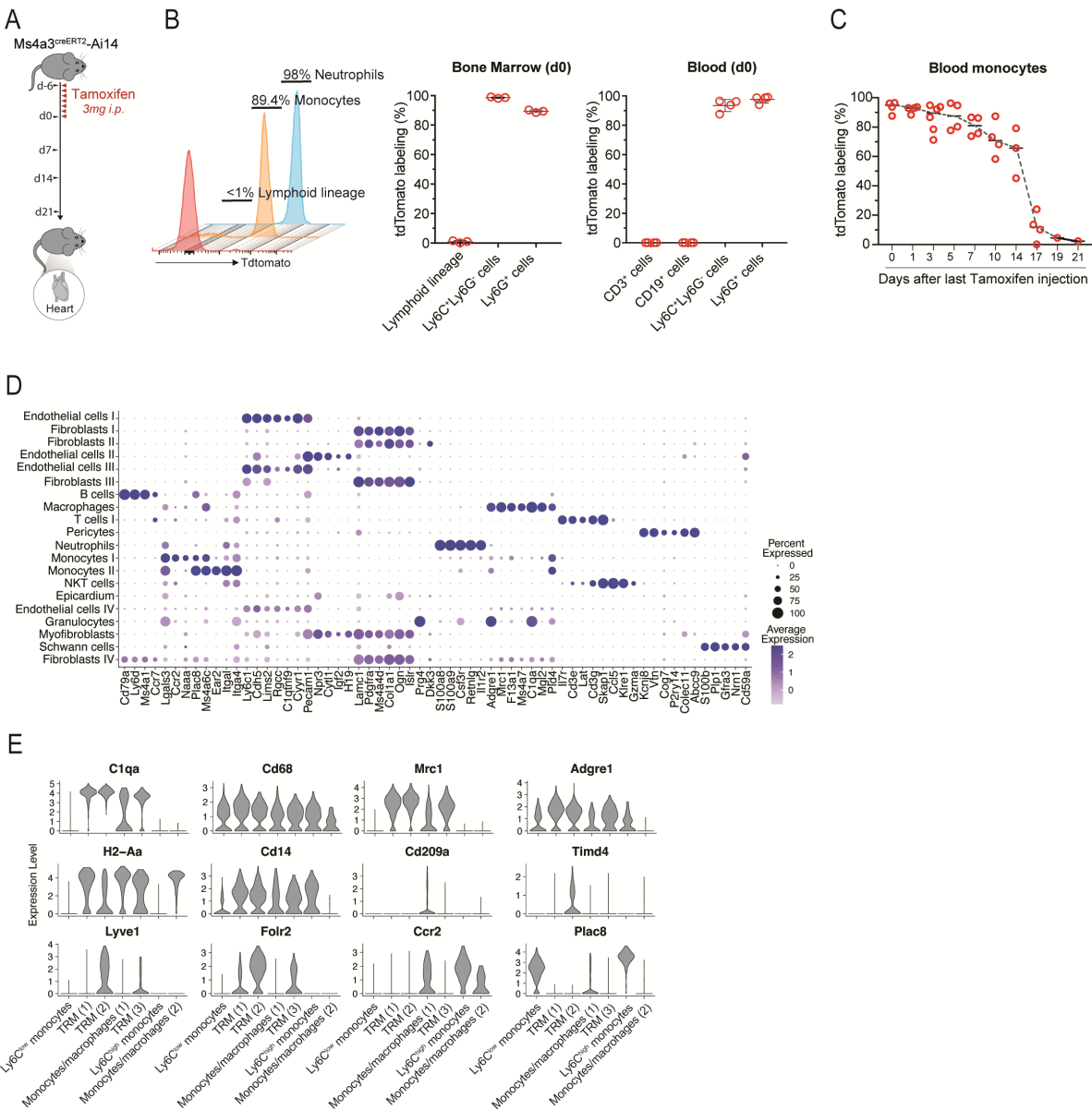


Figure S3. Stroke promotes chronic monocyte recruitment into the heart, related to Figure 4. (A) Schematic experimental design: Ms4a3^{creERT2}xAi14 mouse were treated with tamoxifen for 7 consecutive days. Mice were sacrificed at different time points within the 3 weeks after tamoxifen treatment and the heart myeloid cells were analyzed by flow cytometry (left panel). (B) TdTomato labeling of lymphocytes (CD3⁺, CD4⁺, CD8a⁺, CD19⁺, Ter119⁺), monocytes (Ly6C⁺Ly6G⁻) and neutrophils (Ly6C⁺Ly6G⁺) in bone marrow (mid panels) and blood (right panel) after 7 daily doses of tamoxifen (n=3/4). (C) TdTomato labeling of monocytes (Ly6C⁺Ly6G⁻) in blood over time after 7 daily doses of tamoxifen (n=4). (D) Dot plot showing the expression profile of selected key genes for the identification of cell subsets of cardiac interstitial cells sorted from hearts one month after stroke or control surgery in Ccr2^{creERT2}xAi14 reporter mice (n=2 mice/group). The dot size corresponds to the fraction of cells within each condition expressing the indicated transcript, and the color indicates

average expression. (E) Violin plots showing the expression levels of selected key genes for the identification of the populations of cardiac monocytes and macrophages.

Figure S4.

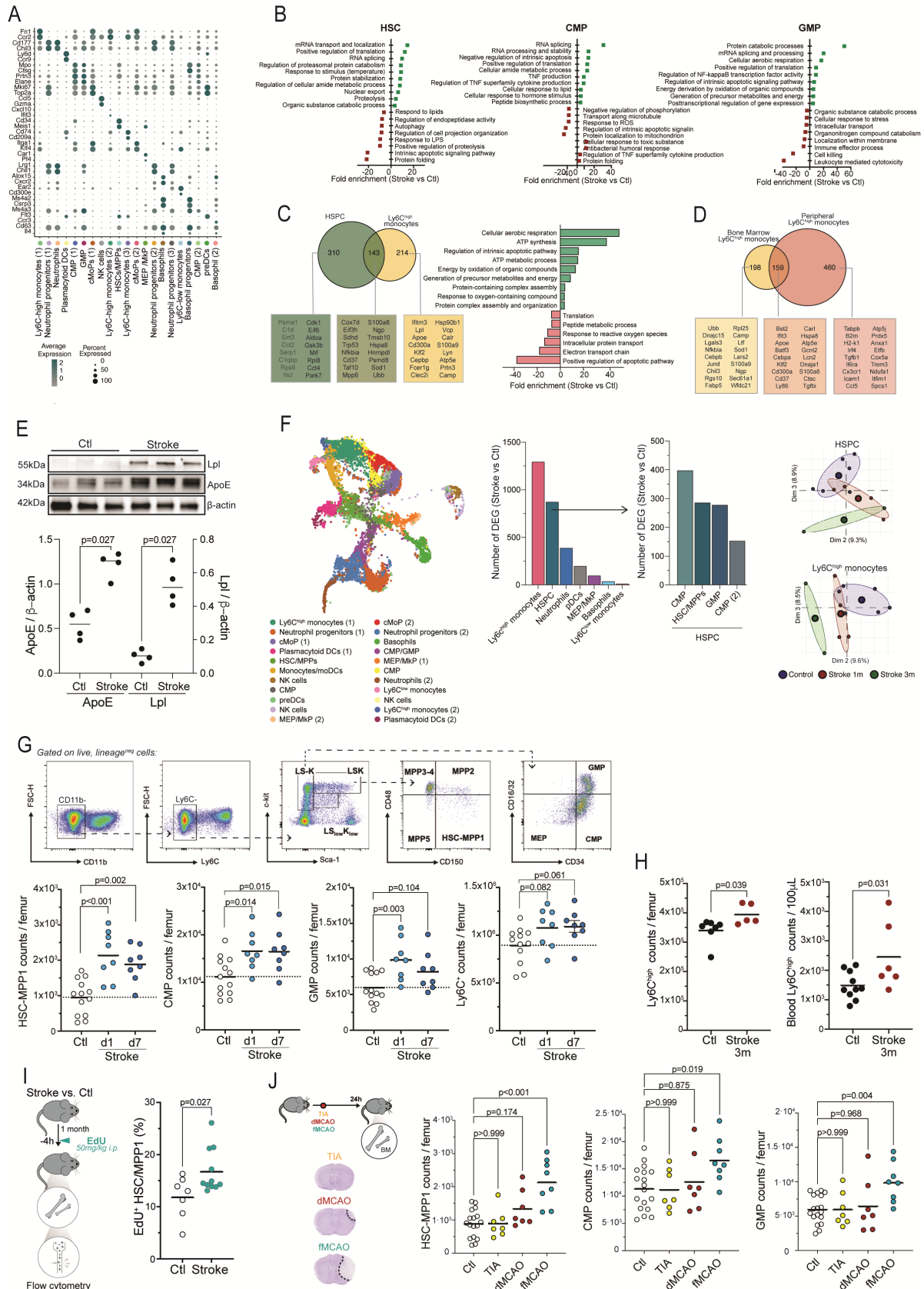


Figure S4. Bone marrow cellularity and function is chronically altered after stroke, related to Figure 5. (A) Dot plot showing the expression profile of selected key genes for the identification of the populations of lymphoid (CD3, CD4, CD8a, CD19 and Ter119)-lineage and neutrophil (Ly6G) negative myeloid cells sorted from the BM of control and stroke mice 1 month after stroke (n=4/group). The dot size corresponds to the fraction of cells within each condition expressing the indicated transcript, and the color indicates average expression. (B) Pathway analysis was performed using differentially expressed genes between stroke and control conditions in hematopoietic stem cells (HSC), common myeloid progenitors (CMP) and granulocyte-monocyte progenitors (GMP). Biological processes were grouped and sorted by p value. (C) Venn analysis illustrating shared DEGs between stroke and control conditions in both HSC and Ly6C^{high} monocytes (right panel). Pathway analysis of the shared DEGs in HSC and Ly6C^{high} monocytes. Biological processes were grouped and sorted by p value (left panel). (D) Venn diagram illustrating shared DEGs between stroke and control conditions in bone marrow (BM) and circulating (blood) Ly6C^{high} monocytes. (E) Representative immunoblot graph of the Lipoprotein ligase (Lpl) and Apolipoprotein E (APOE) in cultured BM derived macrophages (BMDM) isolated from mice one month after stroke and control mice (upper panel). Corresponding quantification of the APOE and Lpl intensity normalized to β -actin (U test, n=4 per group). (F) UMAP plot of the 23,516 lymphoid lineage- (CD3, CD4, CD8a, CD19 and Ter119) and neutrophil- (Ly6G) negative myeloid cells sorted from the BM three months after stroke or control (left panel). Quantification of DEGs between stroke and control conditions per identified subset (adj. p value <0.05) (middle panels). Euclidian distances in the PCA space of HSPC and Ly6C^{high} monocytes from control mice and mice one month and three months after stroke. (G) Representative gating strategy for BM progenitor cells and cell count quantifications of hematopoietic stem cells-multipotent progenitors 1 (HSC-MPP1), common myeloid progenitors (CMP), granulocyte-monocyte progenitors (GMP) and Ly6C⁺ monocytes in stroke and control mice at 1 and 7 days after stroke (U-test; n=9/13 per group). LSK: Lin-Sca1+c-Kit⁺; LS-K: Lin-Sca1-c-Kit⁺; LS^{low}K^{low}: Lin-Sca1^{low}c-Kit^{low}; MMP: multipotent progenitors. (H) Cell count quantification of BM (left panel, t test, n=7/5 per group) and blood Ly6C^{high} monocytes (right panel, t test, n=10/6 per group) at three month after stroke and control. (I) Schematic experimental design: stroke and control mice were administered with EdU 4h before sacrifice. Subsequently, BM cells were isolated and analyzed by flow cytometry (left panel). Corresponding quantification of the percentage of EdU⁺ cells from HSC/MPP1 in stroke and control mice (U-test; n=7/11 per group). (J) Schematic experimental design: mice underwent either transient ischemic attack (TIA), distal Middle Cerebral Artery occlusion (dMCAo) or filament-induced occlusion of the proximal Middle Cerebral Artery (fMCAO). BM was collected 24h post-surgery and analyzed by flow cytometry (upper left panel). Representative images of the corresponding brain lesions 24h after each surgery (bottom left panel – no structural lesion after TIA). Cell count quantification of HSC-MPP1, CMP and GMP for each condition (U-test; n=7-17 per group).

Figure S5.

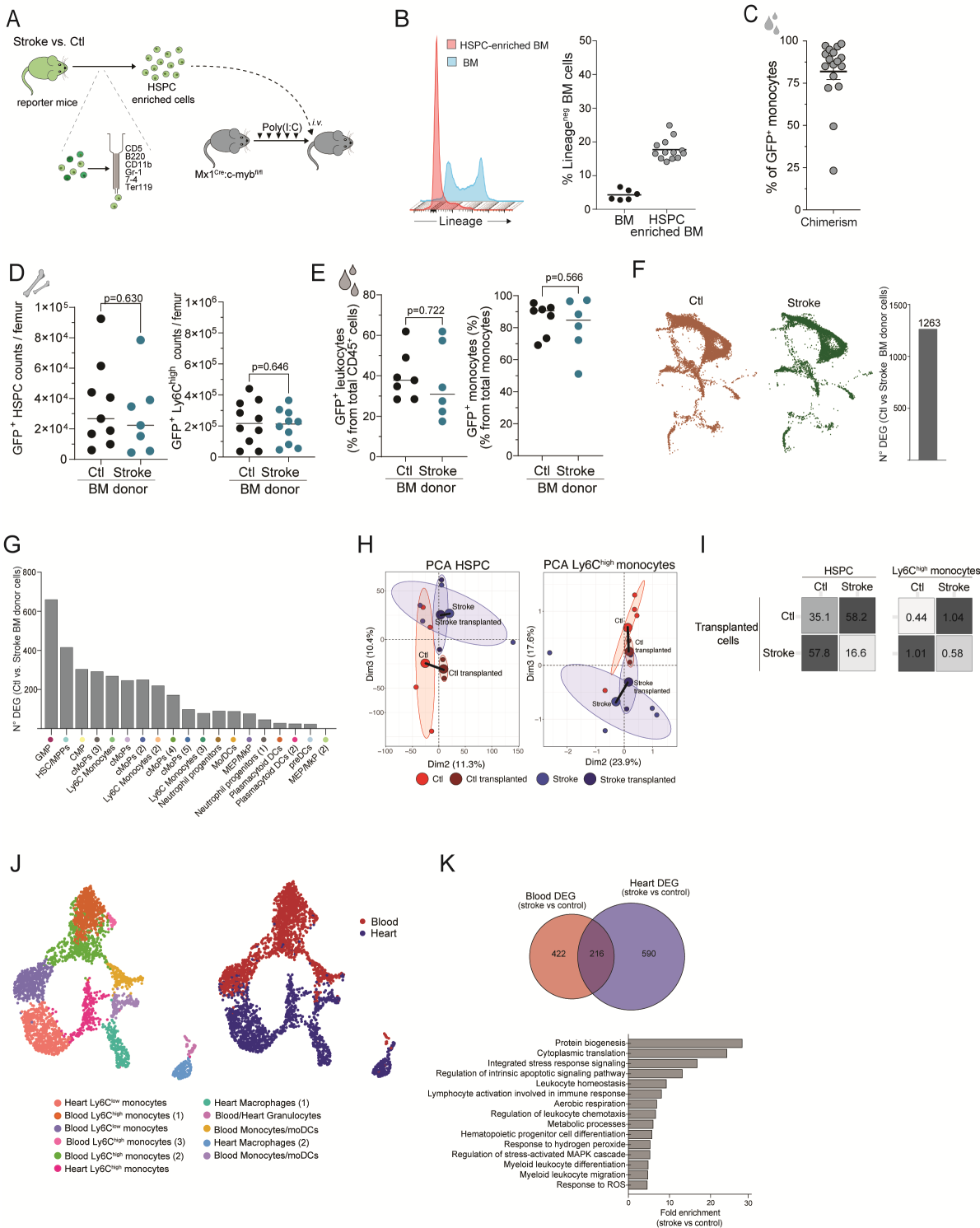


Figure S5. Stroke induces persistent innate immune memory, related to Figure 5. (A) Schematic experimental design: bone marrow (BM) cells were isolated from actin-eGFP or kikGR control and stroke mice 1 month after stroke and enriched for hematopoietic stem and progenitor cells (HSPC). HSPC-enriched GFP⁺ cells were transplanted into BM-depleted Mx1^{Cre};c-myb^{fl/fl} mice. **(B)** Histogram of cells before and after HSPC enrichment showing the proportion of lineage^{neg} and lineage^{pos} BM

cells (right panel). Corresponding flow cytometry quantification of the percentage of lineage^{neg} cells before and after HSPC enrichment (n=6/12 per group, right panel). **(C)** Blood chimerism 1 month after BM transplantation, depicted as the percentage of GFP⁺ monocytes in blood from recipient mice. **(D)** Percentage of GFP⁺ donor-derived HSPC (Lineage⁻ c-kit⁺) cells and Ly6C^{high} monocytes from recipient mice (n=7/10 per group). Results indicate no difference in repopulation efficacy between control and stroke donors. **(E)** Percentage of circulating eGFP⁺ leukocytes (CD45⁺) monocytes (Ly6C^{high}) from recipient mice (n=7/6 per group). **(F)** UMAP plot of myeloid cells from the BM of transplanted mice, split by condition (left panel) and number of differentially expressed genes (DEG) between stroke and control (adjusted p value <0.05). **(G)** Number of DEG between stroke and control conditions per cell type. **(H)** PCA plot displaying individual samples from the BM of stroke (light blue) and control mice (light red) and the BM of recipient mice transplanted with stroke (dark blue) and control (dark red) GFP⁺ HSPC-enriched BM cells (left panels). The PCA was calculated from a total of 18,834 genes identified in BM myeloid cells. Euclidian distances between stroke samples and control samples are indicated in black lines and were calculated from the mean of each cluster. **(I)** Euclidian distances in the PCA space between the stroke and control samples and samples from recipient mice transplanted with stroke and control GFP⁺ HSPC-enriched BM cells. **(J)** UMAP plot of a total of 3,098 GFP⁺ blood monocytes and cardiac monocytes/macrophages from recipient mice transplanted with stroke or control GFP⁺ HSPC-enriched BM cells, colored by identified cluster (left panel) or by organ (right panel). **(K)** Venn diagram illustrating shared DEGs between blood and heart GFP⁺ cells isolated from recipient mice transplanted with stroke or control GFP⁺ HSPC-enriched BM cells (upper panel). Pathway analysis was performed using ShinyGO for shared DEGs between blood and heart, with an FDR-adj. p value <0.05 (bottom panel).

Figure S6

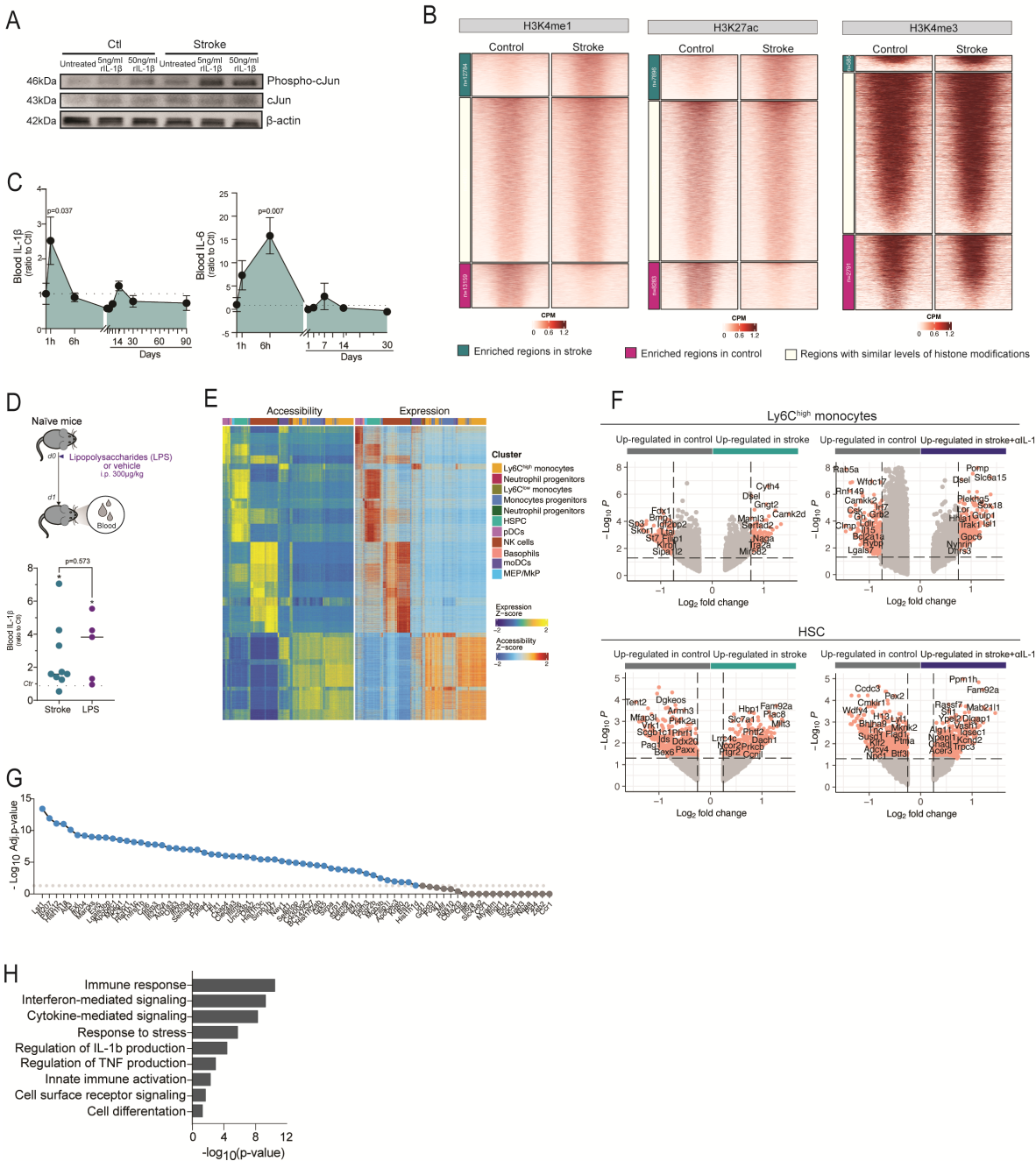


Figure S6. Innate immune memory is mediated by early post-stroke IL-1 β secretion, related to Figure 6.

(A) Representative immunoblot graph of the protein levels of cJun and phospho-cJun in cultured bone marrow-derived macrophages (BMDM) isolated from mice one month after stroke and control mice, and following stimulation with 5ng/ml or 50ng/ml of recombinant IL-1 β . (B) Density heatmaps H3K4m1, H3K27ac or H3K4me3 peaks in Ly6C^{high} monocytes from mice one month post-stroke (up, green) or control mice (down, pink), split by condition. Regions with similar levels of histone modifications are also shown (middle, white) (left panel). (C) Plasma IL-1 β and IL-6 levels at indicated time points after stroke, expressed as ratio to control levels (baseline) before stroke. (D)

Schematic experimental design: mice received a single injection intraperitoneal (i.p.) injection of lipopolysaccharides (LPS). Twenty-four hours later, mice were sacrificed, and blood was collected (upper panel). Plasma IL-1 β levels 24h after stroke or LPS treatment, expressed as ratio to IL-1 β levels from naïve mice (control). **(E)** Side-by-side heatmaps showing the correspondence links of peaks (left) and gene (right) from the single nuclei ATAC sequencing and single cell mRNA sequencing, respectively. **(F)** Volcano plots showing the differentially accessible peaks between vehicle-treated stroke and control and between α IL-1 β -treated stroke and control mice for Ly6C^{high} monocytes (upper panel) and HSC (lower panel). Colored peaks are $p < 0.05$ and $\log_2FC > 0.75$, and top peaks were associated to the closest genes (Table S4). **(G)** Dot plot showing the statistical significance of the differential expression of genes that showed a significant correlation with the top 10 transcription factors with highest differential activity between stroke and control conditions in Ly6C^{high} monocytes. **(H)** Pathway analysis performed by g:Profiler using the differential expressed genes between stroke and control conditions that showed significant correlation with the top 10 transcription factors with highest differential activity between these two conditions in Ly6Chigh monocytes. Biological processes were grouped and sorted by p value.

Figure S7.

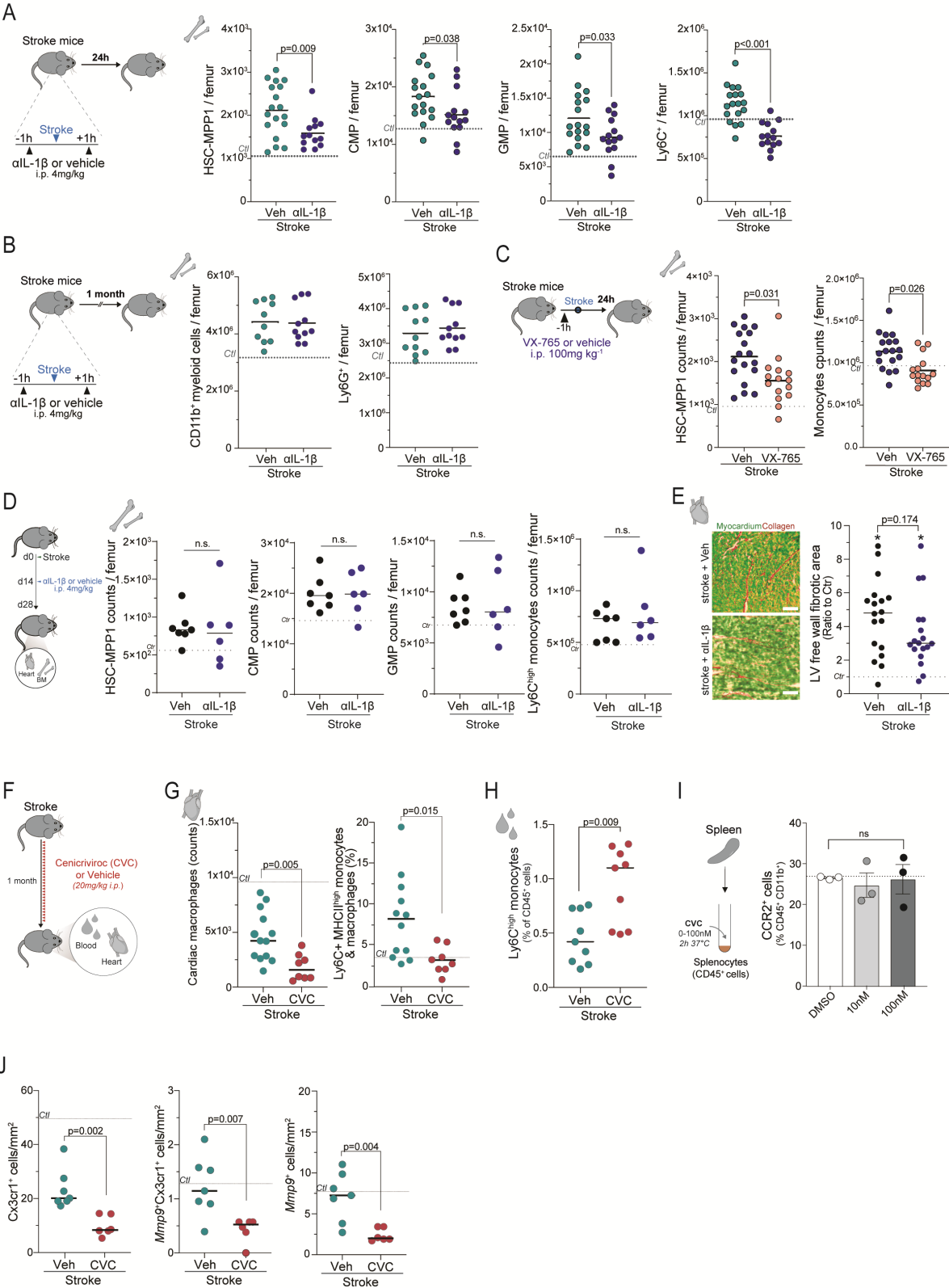


Figure S7. Interleukin-1 β -driven innate immune memory mediates remote organ dysfunction after stroke, related to Figure 7. (A) Schematic experimental design: mice received IL-1 β -specific neutralizing antibodies or vehicle 1h before and 1h after stroke induction. Twenty-four hours later, BM cells were isolated for flow cytometry (left panel). Cell count quantifications of hematopoietic

stem cells-multipotent progenitors 1 (HSC-MPP1), common myeloid progenitors (CMP), granulocyte-monocyte progenitors (GMP) and total Ly6C⁺ monocytes in BM from anti-IL1 β or vehicle-treated stroke mice (U-test; n=13/18 per group). **(B)** Same experimental design as in (A), but BM were collected 1 month after stroke for flow cytometric cell count quantifications of total CD11b⁺ myeloid cells and Ly6G⁺ neutrophils (U-test; n=10/11 per group). **(C)** Schematic experimental design: mice received the caspase-1 inhibitor VX-765 or vehicle 1h before stroke induction. Twenty-four hours later, BM were collected for flow cytometry analysis (left panel). Cell count quantifications of HSC-MPP1 and total Ly6C⁺ monocytes in BM from VX-765 or vehicle-treated stroke mice (U-test; n=18/15 per group). **(D)** Schematic experimental design: mice received IL-1 β neutralizing antibodies or vehicle 14d after stroke. Two weeks later, one month after stroke, BM and hearts were collected for flow cytometry and histology staining, respectively (left panel). Cell count quantifications of HSC-MPP1, CMP, GMP and Ly6C^{high} monocytes in BM from anti-IL1 β or vehicle-treated stroke mice (t-test; n=7/6 per group). **(E)** Representative images of the Sirius red/Fast green collagen staining performed on cardiac coronal sections from delayed anti-IL1 β and vehicle-treated stroke mice (left panel). Quantification of cardiac fibrosis in the LV free wall in anti-IL1 β and vehicle-treated stroke mice. Dashed line indicates mean percentage of fibrotic area in control mice, * indicates significant difference between respective stroke to control mice per treatment condition (t test, n= 5 per group, 3-4 heart sections per mouse). **(F)** Schematic experimental design: Stroke mice were administered daily with the dual C-C chemokine receptors type 2 and 5 antagonist Cenriciviroc (Stroke+CVC) or vehicle (Stroke) for 28 days. Mice were sacrificed at day 28 and the heart and blood were collected for flow cytometry and histological analysis. **(G)** Flow cytometry of total CCR2⁺ and Ly6C⁺MHC-II^{high} monocytes/macrophages in the heart of stroke mice treated with CVC or vehicle (t test; n=8/12 per group). **(H)** Flow cytometry for circulating Ly6C^{high} monocytes in CVC- or vehicle-treated stroke mice, expressed as percentage of total circulating CD45⁺ cells. Dashed lines indicate mean values in control mice (t test; n=9 per group). **(I)** Schematic experimental design: splenocytes were freshly isolated from naïve mice and treated with CVC at a dose of 0 (DMSO), 10 and 100 nM. Two hours after treatment, the percentage of live CCR2⁺ cells was evaluated by flow cytometry. **(J)** smFISH quantification for the detection of total *Cx3cr1*⁺ cells (left panel), *Mmp9*⁺ *Cx3cr1*⁺ cells (mid panel) and *Mmp9*⁺ cells (right panel) in the hearts of CVC- or vehicle-treated stroke mice. DAPI was used as nuclear dye. Dashed lines indicate mean values in control mice (t test, n=6/7 per group).

STAR METHODS

RESOURCE AVAILABILITY

Lead contact

Further information and requests for resources and reagents should be directed to and will be fulfilled by the lead contact, Arthur Liesz (Arthur.Liesz@med.uni-muenchen.de).

Materials availability

This study did not generate new unique reagents.

Data and code availability

Single-cell RNA-seq and single-nuclei ATAC-seq data have been deposited at GEO and are publicly available as of the date of publication. Accession numbers are also listed in the key resources table. This paper does not report original code. The used scripts for bioinformatic analyses of sequencing data are available at Mendeley Data (DOI: 10.17632/xygfn6kbg.1) and at <https://github.com/Lieszlab>. Any additional information required to reanalyze the data reported in this paper is available from the lead contact upon request.

EXPERIMENTAL MODEL AND STUDY PARTICIPANTS DETAILS

Clinical patient population

Clinical data from three stroke patients recruited within the Stroke Induced Cardiac FAILURE study (SICFAIL) consortium that were followed-up by cardiac echocardiography at three and 6 months after the incident stroke event was obtained. Methods of the SICFAIL study have been published elsewhere.⁶⁰ Patients underwent transthoracic echocardiography as part of the clinical routine by expert sonographers of the Comprehensive Heart Failure Centre Würzburg of the University Hospital Würzburg using standardized protocols. Pulsed-wave tissue Doppler imaging was obtained at the septal and lateral mitral annulus in the apical four-chamber view. The E/e' ratio was calculated averaging the lateral and septal e' velocities.⁸² Worsening of diastolic function was defined as an increase in the E/e' ratio of at least 5 points. This study complied with the Declaration of Helsinki and was approved by the Ethics

Committee of the Medical Faculty of the University of Würzburg (176/13). Demographical and clinical characteristics of the three patients are shown below.

	Patient 1	Patient 2	Patient 3
Age range, years	70-80	70-80	60-70
Sex	Male	Male	Male
Baseline NIHSS	9	0	4
HS-CRP	N/A	0.26	0.17
NT-proBNP	N/A	908	270

Human postmortem material was obtained from the National Center Biobank Network (NCBN) from Japan and the Institute of Legal Medicine, LMU University from Munich. Ethical approval for the use of human postmortem material was granted according to institutional ethics board protocol and national regulations. Detailed demographics and clinical characteristics of the patients are found in Table S3.

	Stroke (n=13)	Control (n=6)
Age, years	79 (12)	80 (29.3)
Sex (male), n (%)	76% (10)	33% (2)
Baseline NIHSS	23 (12)	N/A
Time from stroke to death, days	44 (48.5)	N/A

Shown as Median (Interquartile range, IQR), unless indicated

Animal experiments

All animal procedures were performed in accordance with the guidelines for the use of experimental animals and were approved by the respective governmental committees (Regierungspraesidium Oberbayern, the Rhineland Palatinate Landesuntersuchungsamt Koblenz). Wild-type C57BL/6/J mice were purchased from Charles River. eGFP reporter mice (C57BL/6-Tg (CAG-EGFP)131Osb/LeySopJ), KikGR reporter mice (Tg(CAG-KikGR)33Hadj) and Ai14 reporter mice (B6.Cg-Gt(ROSA)26Sortm14(CAG-tdTomato)Hze/J) were purchased from the Jackson Laboratory (US), and bred and housed at

the animal core facility of the Center for Stroke and Dementia Research (Munich, Germany). The Mx1-Cre mice (B6.Cg-Tg(Mx1-cre)1Cgn/J) and the Myb^{fl/fl} floxed mutant mice (B6.129P2-Myb^{tm1}Cgn/TbndJ) were purchased from Jackson Laboratory (US). Ccr2^{CreERT2}-TdT (Ccr2^{tm1}(cre/ERT2,mKate2)Arte) mice were kindly provided by the Becher lab at University of Zurich (Switzerland), and were housed at the animal core facility of the Walter-Brendel-Center for Experimental Medicine (Munich, Germany) and crossbred to Rosa26tdTomato reporter mice. Ms4a3^{creERT2} mice (B6J-Ms4a3em1(CreERT2)-Gt(ROSA)26Sortm14(CAG-tdTomato)) were generated at the animal core facility of the Center for Stroke and Dementia Research (Munich, Germany), by CRISPR-Cas9-mediated insertion of an IRES-CreERT2 cassette into the 3' un-translated region (3'UTR) of the *Ms4a3* gene in C57BL/6 zygotes. Genotyping was done by PCR using the following primers: Ms4a3 forward primer 5'- GACATTGCAGACGGGATGTAT-3'; Ms4a3 reverse primer 5'- ATCCATGGAGGTGTCATAGACCA-3'; CreERT2 forward primer 5'- AACACCCCGTGAAACTGCTC-3'.

Wild-type male mice and transgenic mice of both sexes (aged 8-12 weeks) were used for the experiments. All mice had free access to food and water at a 12 h dark-light cycle. Data were excluded from all mice that died during surgery. Animals were randomly assigned to treatment groups and all analyses were performed by investigators blinded to group allocation. All animal experiments were performed and reported in accordance with the ARRIVE guidelines.¹¹

METHOD DETAILS

Transient proximal cerebral artery occlusion model

Transient intraluminal occlusion of the middle cerebral artery (MCA) was performed as previously described.¹² Briefly, mice were anaesthetized with isoflurane delivered in 100% O₂. A midline neck incision was made and the common carotid artery and left external carotid artery were isolated and ligated; a 2-mm silicon-coated filament was introduced via a small incision in the external carotid artery and advanced towards the internal carotid artery, therefore occluding the MCA. MCA was occluded for 5 min for a transient ischemic attack (TIA) model or for 60 min for the transient MCAo stroke model. After occlusion, the animals were re-anesthetized, and the filament was removed. MCA occlusion and reperfusion were

confirmed by the corresponding decrease or increase in the blood flow, respectively, measured by a laser Doppler probe affixed to the skull above the MCA territory (decrease in the laser Doppler flow signal >80% of baseline value and increase in the laser Doppler flow signal >80% of baseline value before reperfusion). After recovery, the mice were kept in their home cage with facilitated access to water and food. Body temperature was maintained at 37°C throughout surgery using a feedback-controlled heating pad. The overall mortality rate of stroke mice was approximately 30 %. Exclusion criteria: 1. Insufficient MCA occlusion (a reduction in blood flow to >20% of the baseline value); 2. Insufficient MCA reperfusion (an increase in blood flow of >80% of the baseline value before removing the filament); 3. Death during the surgery.

Permanent distal cerebral artery occlusion model

Permanent occlusion of the distal MCA was performed as previously described.⁸³ Briefly, mice were anaesthetized with isoflurane delivered in 100% O₂ and placed in lateral position. After a skin incision between eye and ear, the temporal muscle was removed and the MCA identified. Then, a burr hole was drilled over the MCA and the dura mater was removed. The MCA was permanently occluded using bipolar electrocoagulation forceps. Permanent occlusion of the MCA was visually verified before suturing the wound. After recovery, the mice were kept in their home cage with facilitated access to water and food. Body temperature was maintained at 37°C throughout surgery using a feedback-controlled heating pad. Exclusion criteria: Artery broken during surgery and/or major bleeding artery and remaining blood between the brain and skull.

Drug administrations

5-ethynyl-2'-deoxyuridine (EdU)

Mice received one i.p. injection of EdU dissolved in 0.9% Sodium Chloride 4 h prior to euthanasia, at a dose of 5 mg kg⁻¹ body weight, in a final volume of 250 µl. For continuous and controlled EdU delivery, osmotic pumps (ALZET) containing 100 µl of EdU at a concentration of 10 mg/ml were implanted i.p. into mice for 1 week.

Anti-IL-1β

Mice received two i.p. injections of antagonizing anti-IL-1β or vehicle (0.9% NaCl) 1 h prior to and 1 h after surgery, at a dose of 4 mg kg⁻¹ body weight, in a final volume of 200 µl.

Recombinant IL-1 β

Mice received one i.p. injection of recombinant IL-1 β or vehicle (0.9% NaCl), at a dose of 40 μ g kg⁻¹ body weight, in a final volume of 100 μ l.

Lipopolysaccharides (LPS)

Mice received one i.p. injection of LPS or vehicle (0.9% NaCl), at a dose of 300 μ g kg⁻¹ body weight, in a final volume of 100 μ l.

CCR2/CCR5 antagonist Cenicriviroc (CVC)

Mice received daily i.p. injections of CVC or vehicle (30% Kolliphor and 70% 0.9% NaCl) at a dose of 20 mg kg⁻¹ body weight, in a final volume of 250 μ l.¹³ First dose was given after stroke induction and then daily for 28 days.

Tamoxifen

Tamoxifen was prepared by dissolving in Miglyol 812 for a final concentration of 20 mg/mL and stored at 4 °C. Mice received daily i.p. injections of Tamoxifen solution at a dose of 120 mg kg⁻¹ body weight, in a final volume of 150 μ l, for 7 consecutive days.

Echocardiography

All mice underwent transthoracic echocardiography using a high-frequency ultrasound system with a 40-MHz linear transducer (Vevo 3100LT, Visual Sonics, Canada). In brief, mice were anaesthetized with isoflurane (in 100% O₂ at 4% induction for 1 min and 1.5% for maintenance) and placed in supine position on a heated platform (37°C). Heart rate was monitored along the recording period. After applying ultrasonic gel, the heart was visualized and a 2D M-mode video (4.5 seconds) was recorded from the parasternal short-axis view. To estimate the mitral valve inflow pattern, the transmitral LV outflow was also recorded from the apical four chamber view using the pulse wave (PW)-doppler imaging mode. All data was analyzed in Vevo 3100 Software, as previously described and according to the American Society of Echocardiography recommendations.¹⁴ The investigators performing and reading the echocardiograms were blinded to the treatment allocation.

ECG telemetry

Continuous electrocardiogram (ECG) acquisition was done over a period of 3 weeks by implanting telemetry transmitters (PhysiolTel ETA-F10, Data Science International, DSI) in male C57Bl/6J wildtype mice (n=4/group) as previously described.^{84,85} Briefly, anesthetized mice were placed in a supine position on a heated platform (37°C). A 1.5-2 cm ventral midline abdominal incision was performed, and a subcutaneous pocket in the upper right chest and left abdomen below the heart was prepared for placing the electrode leads. The transmitter body was gently placed in the peritoneum above the intestine. Using a 14-gauge needle, the electrical leads were tunneled through the peritoneum and subcutaneously positioned in the prepared pockets leading to an Einthoven II configuration. The tips of the leads were fixed to the pectoral muscle using a 7-0 suture, and the abdominal fascia and skin were closed.

Data analysis was done using Ponemah's ECG Pro module (Ponemah software 6.42 version).^{85,86} 24-hour ECG traces on day 3, 7, 14 and 21 post transmitter implantations were subdivided into 12-hour traces to allow a separate analysis of the ECG during day and night time. P, Q, R, S, T marks were automatically annotated by the software. Undetected marks were manually added. 20 consecutive ECG beats were averaged in each 12-hour day and night window to obtain the heart rate (BPM), P wave duration (ms), PR interval (ms), QRS duration (ms), QT interval (ms). QTc was calculated using Bazett's formula.

Cardiac electrophysiology (EP) studies

EP studies were performed 4w post-stroke or naive male C57Bl/6J mice (n=5-7/group) to assess the atrial, av nodal, and ventricular conduction properties, as well as arrhythmia inducibility. An amplifier (AD Instruments), Powerlab (AD Instruments), stimulator (ISO-Stim-01D, npi), and LabChart Pro software (version 8.0, AD Instruments) was used for signal recording and processing as well as intracardiac stimulation. Mice were anesthetized with isoflurane (2.5-4% in 100% oxygen at 1L/min. flow rate) and subsequently maintained at 1.5-2% during EP studies. Mice were positioned in a supine position on a heated platform (37°C) monitored with a rectal temperature probe (Kent Scientific). For surface ECG recording, needle electrodes were placed subcutaneously with the negative lead in the right forelimb, the positive electrode in the left hindlimb, and the ground lead in the right hindlimb allowing an Einthoven I configuration. A midline incision was made along the sternocleidomastoid muscle to visualize and expose the right jugular vein. Two 4-0 sutures were placed at the proximal and distal end of the vein. The suture at the proximal end was tightened and clamped

to straighten the vein. The distal suture was used to hold the catheter in place upon insertion into the heart. A small cut was made in the longitudinal direction of the vein using precision scissors before a 1.1 F octapolar catheter (Millar Instruments) was placed in the vein, followed by gradual advancement into the heart until the tip was located in the RV apex. The correct position of the catheter was confirmed by the local electrograms.

Programmed electrical stimulation was performed following a standard protocol with 120 ms and 100 ms pacing cycle lengths as previously described. In brief, the Wenckebach cycle length was determined by progressively faster atrial pacing rates and the retrograde (VA) conduction cycle length was measured by progressively slower ventricular pacing rates to assess conduction properties of the AV node. Refractory periods in the atrium, the AV node and the ventricle were determined using the standardized S1/S2 protocol. Inducibility of arrhythmias was assessed by applying the standardized S1S2S3 protocol with basic cycle lengths of 120ms and 100 ms and S2/S3 stimulation at cycle lengths of 40-10 ms in 5 ms decrements. Furthermore, burst pacing with application of two 3 second and 6 second bursts at rates of 40–10 ms in 5 ms decrements was performed. An atrial arrhythmia was defined as high frequent atrial signal with regular/irregular AV conduction or a clear change in atrial basic cycle length post stimulation with morphologic change of the atrial signal indicating ectopic origin, either of them lasting for ≥ 1 second.

Non-invasive blood pressure measurements

Mouse blood pressure was evaluated by tail-cuff transmission photoplethysmography using BP-2000 Blood Pressure Analysis System (Visitech Systems, USA). In brief, mice were placed in a holder device with its tail passing through a cuff with an optical sensor. The standard test session was run for 20 times and systolic, diastolic blood pressure and heart rate were acquired.

BM transplantation

Donor animals (actin-eGFP⁺ or KikGR⁺) were euthanized and femurs were collected in cold PBS. Bone marrows were isolated from femurs and filtered through 40 μ m cell strainers to obtain single cell suspensions. Depletion of mature hematopoietic cells, including T cells, B cells, monocytes/macrophages, granulocytes, erythrocytes and their committed precursors was achieved using a negative selection kit for Lineage Cell Depletion (Miltenyi). After washing, cell number and viability was assessed using an automated cell counter (Countess

3, ThermoFisher Scientific) and Trypan Blue solution (Merck, Germany). Cells were injected i.v. into Mx1^{Cre}:c-Myb^{fl/fl} recipient mice ($3-8 \times 10^6$ cells per mouse) in a total volume of 100 μ l saline. At the time of transplantation, recipient mice had previously been treated with poly(I:C) solution (Invivogen) at a dose of 10 μ g g⁻¹ body weight every other day for five times to induce BM depletion.¹⁵ Mice were maintained for 4 weeks after transplantation to establish efficient BM repopulation.

Organ and tissue collection

Mice were terminally anesthetized with ketamine (120mg/kg) and xylazine (16mg/kg). In a subset of experiments, mice were injected i.v. with 3 μ g CD45-eFluor450 or CD45-APC-Cy7, 3 min before transcardiac perfusion, to exclude blood contamination in peripheral organs. Blood was drawn via cardiac puncture and collected in 50mM EDTA tubes (Sigma-Aldrich). Plasma was isolated by centrifugation at 3000g for 10 min and stored at -80°C until further use. Immediately after cardiac puncture, mice were transcardially perfused with 0.9% NaCl and the heart, both lungs, the right liver lobe, the spleen and both femurs and tibias were carefully excised and processed according to the specific endpoint.

Cell isolation

Spleen and bone marrow (from femur) were homogenized and filtered through 40 μ m cell strainers to obtain single cell suspensions. Heart, lung and liver tissues were thoroughly minced in a digestive solution containing 60U/ml DNase, 450U/ml Collagenase I, 125 U/ml Collagenase XI and 60 U/ml Hyaluronidase I-S in PBS and incubated for 30 min at 37°C on a shaker at 250 rpm. Afterwards, samples were filtered through a 40 μ m cell strainer to obtain final single cell suspensions.

Cell sorting

Cell suspensions were obtained as described above and further purified by a density gradient centrifugation with Histopaque-107 at 300g, 4°C for 20 min. The mononuclear layer was isolated and cells were washed twice with PBS. Cell suspensions were stained with surface markers diluted in Brilliant Stain Buffer and sorted using a FACS Aria II cell sorter (BD Biosciences, Inc.) or a SH800S Cell Sorter (Sony Biotechnology). Propidium iodide (PI) or 4',6-diamidino-2-phenylindole (DAPI) were used as a cell viability marker.

Flow cytometry

The primary conjugated anti-mouse antibodies listed above were used for surface marker staining of different leukocytes subpopulations (see Key Resources Table). For high-dimensional flow cytometry of the heart, mice were injected i.v. with 3 μ g CD45-e450 (see antibody list) 3 min before transcardiac perfusion, to exclude blood contamination. All samples were stained with Zombie NIR Fixable Viability Kit (1:1000) for 10 min at 4°C and then with the specific surface markers diluted in Brilliant Stain Buffer, according to the manufacturer's protocols, for 30 min at 4°C. For the Click-iT EdU flow cytometry cell proliferation assay, prior to surface antibody staining, cell suspensions were fixed, permeabilized and the intracellular EdU was labelled by means of a click chemical reaction, following manufacturer's instructions. All flow cytometric data was acquired using a Cytex Northern lightsTM flow cytometer (Cytex Biosciences, US) and analyzed using FlowJo software.

Single cell RNA sequencing

Six mouse single-cell RNA experiments were performed in this study: two on myeloid cells isolated from peripheral organs, including the heart, lung, liver, spleen and/or blood; one on cardiac interstitial cells, and the other three on bone marrow myeloid cells, either from stroke and control mice, or from naïve recipients after BM transplantation. For the first experiments, mononuclear cell suspensions from peripheral organs were incubated with anti-CD16/CD32 antibody to block nonspecific binding and stained for CD45⁺CD11b⁺ myeloid cells (see antibodies list). Unique cell hashtags antibodies were also used to label cells from each organ individually. All surface antibodies and hashtag antibodies were incubated for 30 min at 4°C. Immediately prior to cell sorting, PI was added to all samples to label dead cells. Cells were sorted according to their surface markers (SH800S Cell Sorter, Sony Biotechnology or FACS Aria II Fusion cell sorter, BD Biosciences, Inc.). Sorted and organ-specific labeled cells from the same animal were pooled together in the same collecting tube (for peripheral organs, a cell ratio of 1:4:4:4:4 for the heart, lung, liver, spleen and blood was maintained; for heart and blood from BMT mice, the cell ratio was 2:1, respectively). After sorting, all cells were centrifuged and cautiously resuspended to a final concentration of 1000-1200 cells/ μ l. Cells were then transferred to the Next GEM chip according to manufacturer's instructions. ScRNA-seq and cell hashing libraries were prepared using the 10x Chromium Single Cell 3' Solution combined with feature barcoding technology for Cell surface protein (cell hashing), as per established protocols.¹⁶

For analysis of cardiac interstitial cells, cell suspensions from the heart were obtained by means of an enzymatic digestion as previously described. Cell suspensions were then passed through a 40mm cell strainer to remove cardiomyocytes and incubated with pre-warmed red cell lysis buffer for 2 min to remove blood cells. Dead cell debris was removed with the Dead Cell Removal kit (Miltenyi) and single nucleated cells were incubated with DAPI for 5 min prior to sorting CD45(i.v. injected)-negative live cells on a FACS Aria II Fusion cell sorter (BD Biosciences, Inc.). After sorting, all cells were centrifuged and cautiously resuspended to a final concentration of 1000 cells/ μ l. Cells were then transferred to the Next GEM chip according to manufacturer's instructions. ScRNA-seq libraries were prepared using the 10x Chromium Single Cell 3' Solution, as per established protocols.¹⁶

For the experiments on bone marrow samples, bone marrow cells suspensions were stained with a cocktail of antibodies against markers of the lymphoid lineage (CD3, CD4, CD8a, CD19 and Ter119) and mature neutrophils (Ly6G, see antibodies list). Immediately prior to cell sorting, PI or 7-AAD were also added to label dead cells. Cells were sorted according to the surface markers (SH800S Cell Sorter, Sony Biotechnology, or FACS Aria II Fusion cell sorter, BD Biosciences, Inc.) and the negative fraction of BM myeloid cells (depleted of lymphoid lineage cells and neutrophils) was collected. After sorting, cells were centrifuged and cautiously resuspended to a final concentration of 1000-1400 cells/ μ l. Cells were then further processed according to manufacturer's (10X) instructions. The scRNA-seq libraries were prepared using the 10x Chromium Single Cell 3' Solution.

In all six experiments, quality control of all cDNA samples was performed with a Bioanalyzer 2100 (Agilent Technologies) and libraries were quantified with the Qubit dsDNA HS kit. Gene expression libraries were sequenced on an Illumina NextSeq 1000 or 2000 using 20,000 reads per cell. Cell-surface protein expression libraries were sequenced on an Illumina NextSeq 1000 or 2000 aiming for 5,000 reads per cell.

Single cell RNA-seq data analysis

Cell Ranger software was used to demultiplex samples, process raw data, align reads to the mouse mm10 reference genome (or a custom mouse mm10 reference genome with the eGFP, kikGR or tdTomato marker genes incorporated) and summarize unique molecular identifier (UMI) counts. Filtered gene-barcode and hashing-barcode matrices that contained only barcodes with UMI counts that passed the threshold for cell detection were used for further

analysis. Filtered UMI count matrices were processed using R and the R package Seurat. As quality control steps, the following cells were filtered out for further analysis: (1) doublets originating from two cells from different samples (one cell positive for two HTO); (2) cells with no HTO detected; (3) cells with a number of detected genes <500 or >6000; (4) cells with >7% of counts that belonged to mitochondrial genes. Hereafter, raw gene counts in high-quality singlets were log normalized and submitted to the identification of high variable genes by MeanVarPlot method. Data was scaled and regressed against the number of UMIs and mitochondrial RNA content per cell. Data was subjected to principal component analysis and unsupervised clustering by the Louvain clustering method. Cell clusters were visualized using Uniform Manifold Approximation and Projection (UMAP) representations. Clusters were manually annotated using the top upregulated genes for each cluster and through the UMAP visual inspection of the expression of key previously described markers. After initial cluster annotation, clusters of T and B cells (between 5-20% of total cells, depending on the experiment) were removed and all remaining myeloid cells were reanalyzed. Differentially expressed genes between conditions were calculated using the FindMarkers function. Volcano plots were generated using EnhancedVolcano in R (Bioconductor EnhancedVolcano v.1.6.0).¹⁷ Pathway enrichment analysis was performed using Ingenuity Pathway Analysis (Qiagen) and ShinyGO⁸⁰. Trajectory and pseudotime analysis were computed on the corresponding UMAP projections using Monocle 3.¹⁸ The CellRank framework (v2.0.2) was used to identify potential genes and GO terms associated with the monocyte-macrophage differentiation trajectory.⁷¹ In brief, for every single cell fate probabilities of reaching tissue-resident macrophages, as a differentiated terminal state, were calculated. These fate probabilities were correlated with gene expression to uncover putative trajectory driver genes. Gene expression was modelled by generalized additive models (n_knots=6). Cell-to-cell communication network analysis was performed using R toolkit CellChat.⁷²

Single Nuclei ATAC-seq

Single nuclei suspensions were prepared as previously reported.¹⁹ In brief, BM cell suspensions were obtained as described for the single-cell sequencing experiments. Live, lymphoid lineage (CD3, CD4, CD8a, CD19 and Ter119) and neutrophil (Ly6G) negative BM cells were sorted using a FACS Aria II Fusion cell sorter (BD Biosciences, Inc.). Cells were centrifuged and incubated twice with Nuclei EZ Lysis Buffer on ice for 5 min each time. Lysed cells were washed and nuclei were incubated with 7AAD at 1µg/ml for microscopic

inspection of integrity before sorting on a FACS Aria II Fusion (BD Biosciences). Then, nuclei were further processed according to manufacturer's (10X) protocols at a concentration of 1000-5000 nuclei/ μ l. Single nuclei ATAC libraries were prepared using the 10x Chromium Next GEM Single Cell ATAC kit. Quality control of all cDNA samples was performed with a Bioanalyzer 2100 (Agilent Technologies). Libraries were sequenced on an Illumina NextSeq 1000, aiming for 25,000 reads per nuclei.

Single nuclei ATAC-seq data analysis

Cell Ranger ATAC software (10x Genomics) was used to process raw single nuclei ATAC-seq data, align reads to the *Mus musculus* mm10 reference genome, generate the peak matrix with single-cell accessibility counts and the fragments file with unique fragments across all single cells. Filtered peak-barcode matrices that contained only barcodes with UMI counts that passed the threshold for cell detection were used for further analysis. Filtered matrices and fragment files were processed using R and the R packages Signac and Seurat. In brief, a chromatin accessibility matrix was created and as quality control steps, the following nuclei were filtered out for further analysis: (1) nuclei with a total detected fragments $> 30,000$ or $< 5,000$; (2) nuclei with the fraction of all fragments that fall within ATAC-seq peaks $< 40\%$; (3) nuclei with a transcriptional start site (TSS) enrichment score lower than 2; and (4) nuclei with a ratio of mononucleosomal to nucleosome-free fragments higher than 4. Peaks were called using MACS2.²⁰ Hereafter, UMAP based on latent semantic indexing (LSI) was generated to visualize data in the two-dimensional space and a gene activity matrix was created to quantify the activity of each gene in the genome by assessing its chromatin accessibility associated with each gene. Next, to help interpret data, the integration pipeline (canonical correlation analysis) from the Seurat package was used to perform cross-modality integration and label transfer on the single-cell ATAC dataset and single-cell mRNA sequencing dataset also generated from BM myeloid cells. Shared correlation patterns in the gene activity matrix and the single-cell mRNA sequencing were used to identify matched biological states and annotate predicted cluster labels for all nuclei from the ATAC object. Only those nuclei with a predicted score above the 0.5 cutoff were retained and considered for further analyses. Volcano plots showing differential accessible peaks between conditions were generated using EnhancedVolcano in R (Bioconductor EnhancedVolcano v.1.6.0).¹⁷ To identify differentially-active motifs between experimental conditions within specific cell types, we computed a per-cell motif activity score using chromVAR (adj p-value < 0.05).²¹

Motif position frequency matrices were obtained from the JASPAR database. For each gene, we used the ArchR package to identify set of peaks that regulate the gene by computing the correlation between gene expression and accessibility at nearby peaks. Peak-to-gene links were identified using default parameters, with $k=100$ and empirical p-value estimation. Positively correlated peak-to-gene links were defined with cutoffs $r > 0.45$ and $FDR < 0.1$. The corresponding peak-to-gene matrix was obtained by returning matrices from `plotPeak2GeneHeatmap()` function with $k = 25$, grouped by cluster identities. To further characterize these peak-to-gene links, the presence of putative transcription factor motifs was identified using the R package `motifmatchr`. Peaks were converted to GRanges and position weight matrices were obtained from JASPAR 2022 database.²²

Bulk ATAC sequencing

Bone marrow (BM) cells were isolated from naïve mice as previously described above. Depletion of mature hematopoietic cells, including T cells, B cells, monocytes/macrophages, granulocytes, erythrocytes and their committed precursors was achieved using a negative selection kit for Lineage Cell Depletion (Miltenyi). Cells were then cultured for 24h at 37°C and 5% CO₂ at a density of $2.5 \cdot 10^5/\text{mL}$ in StemSpan™ SFEM medium supplemented with Priomicin (1:500), thrombopoietin (TPO) (100 ng/ml), and stem cell factor (SCF) (20 ng/ml) to maintain the stemness of the progenitors and prevent extensive differentiation. Then, cells were exposed to either Isotype or recombinant IL-1 β at a concentration of 10 ng/ml overnight at 37°C. The next morning, cells were harvested, and ATAC-Seq kit libraries were prepared using the ATAC-Seq Kit from Active Motif, following the manufacturer's instructions. Libraries were pooled and sequenced on an Illumina NextSeq 1000. Bulk ATAC-seq data was aligned to the mouse genome and read filtering, peak calling and IDR based peak filtering was performed by implementing the ENCODE ATAC-seq pipeline.⁸⁷ The bigwig coverage track was generated using Deeptools (v3.1.3).⁸⁷ Differentially accessible peaks (3 groups: control, shared, IL-1 β -treated) were identified using `csaw`.⁷⁴ Motif enrichment analysis was performed using `monaLisa`.⁷³

CUT&tag sequencing

BM cell suspensions were obtained as described for the single-cell sequencing experiments. BM monocytes (CD11b+Ly6C+Ly6G-) and the lineage- (CD3, CD4, CD8a, CD19, Ter119) and Ly6G) negative myeloid fraction of BM (HSPC-enriched population) were sorted using

a FACS Aria II cell sorter (BD Biosciences, Inc.). Cleavage Under Targets Tagmentation (CUT&Tag) assays for H3K27Ac, H3K4me1 and H3K4me3 were performed on these two cell populations as previously reported^{88,89}, using the EpiCypher protocol with specific modifications. Briefly, nuclei were extracted from $1 \cdot 10^5$ cells, washed twice and incubated with 10 μ L of activated concanavalin A beads (ThermoFisher) for 10 min at RT. The beads were then resuspended in cold antibody buffer containing primary antibodies (against H3K27ac, H3K4me1 or H3K4me3) and the mixture was incubated overnight at 4°C on a nutator. Then, the beads were washed twice and resuspended in secondary H+L antibody (NovusBio) diluted in 50 μ L digitonin buffer, followed by incubation for 30 min at RT on a rotator. Samples were then incubated with 2.5 μ L CUTANA pAG-Tn5 (EpiCypher) for 1 h at RT on a nutator. DNA was tagmented for 1 h at 37°C using tagmentation buffer and tagmented chromatin fragments were released for 1 h at 58°C. 13 μ L of tagged DNA was used to prepare the library using NEBNext® High-Fidelity 2X PCR Master Mix (NEB) with CUT&Tag specific PCR cycling parameters. DNA was purified using AMPureXP Beads (Beckman Coulter). The quality of the CUT&Tag libraries was assessed using the Agilent 2100 Bioanalyzer System (Agilent). Libraries were pooled together and sequenced on an Novaseq 6000 SP 300 flowcell using paired-end sequencing (2*150). CUT&Tag-seq data was mapped using CUT&RUNTools 2.0.⁹⁰ Differentially accessible peaks (3 groups - control, shared, stroke) were identified using csaw.⁷⁴ Motif enrichment analysis was performed using monaLisa.⁷³ The plotting of the Cut&tag signal at genomic features was performed using SeqPlots.⁹¹

Second harmonic generation microscopy imaging

Mice were deeply anesthetized and euthanized as described above. Hearts were immediately extracted and immersed in 4% paraformaldehyde overnight. Afterwards, hearts were embedded in 4% agarose, coronally sectioned to 100 μ m thick sections and kept at 4°C as free-floating sections in PBS. Sections were then imaged using Zeiss LSM 7 MP microscopy (Zeiss, Germany), acquiring second harmonic generation signals (445 nm) after excitation at a wavelength of 895 nm. SHG images were quantitatively analyzed with ImageJ software as previously described.^{23,24} In brief, the images underwent Fast Fourier Transformation (FFT) and then were submitted to an elliptic fit to obtain Aspect Ratio values as a measure of the anisotropy of the collagen fiber distribution.

Mouse heart histological sections

Mice were deeply anaesthetized and euthanized as described above. For conventional and immunofluorescence staining procedures, hearts were immediately extracted, submerged in 4% paraformaldehyde overnight at 4°C, embedded in paraffin and coronally sectioned to 5 µm thick sections. For RNA-fluorescence in situ hybridization (RNA-FISH), hearts were excised, directly flash-frozen on dry ice and coronally cryosectioned to 5µm thick sections.

Human heart histological sections

Cardiac tissue specimens were obtained from adult subjects with ischemic stroke and controls. Specimens were immersed in 10% formalin upon collection to preserve tissue integrity, embedded in paraffin and sectioned at 3 µm thick sections.

Picrosirius red staining

Mouse and human heart paraffin sections were deparaffinized, stepwise in xylene, 100% ethanol, 70% ethanol and 50% ethanol, and then stained with Fast Green solution for 20 min. The sections were washed with 30% acetic acid, rinsed in tap water and submerged to Picrosirius red Solution for 60 min. Hereafter, sections were washed with 30% acetic acid and absolute alcohol, dried at room temperature (RT) and mounted with Eukitt® Quick-hardening mounting medium. Images were acquired at 20x magnification using Axio Imager 2 (Zeiss, Germany).

Hematoxylin and eosin staining

Mouse and human heart paraffin sections were processed and deparaffinized as previously described. Sections were incubated with Mayer's hematoxylin solution at RT for 5 min and washed under running tap water for 10 min. Afterwards, sections were incubated with 1% Eosin Y solution at RT for 3 min and rinsed with distilled water. Finally, sections were dehydrated stepwise with 70% ethanol, 80% ethanol, 90% ethanol and 100% ethanol, dried at RT and mounted with Eukitt® Quick-hardening mounting medium. Images were acquired at 100x magnification using Axio Imager 2 (Zeiss, Germany).

Immunofluorescence staining

Mouse heart paraffin sections were processed and deparaffinized as previously described. After deparaffinization, sections were incubated with blocking solution containing 2% goat serum, 1% BSA and 0.1% cold fish skin gelatin in PBS for 1h at RT. Afterwards, sections

were incubated with the primary antibodies against Collagen I (1:50), Collagen III (1:100), Fibronectin (1:50) or Tyrosine Hydroxylase (TH) (1:100) overnight at 4°C. Then, sections were washed in PBS and incubated with Alexa Fluor 647 goat anti-rabbit secondary antibody (1:100) in the dark for 1 h at RT. After washing, sections were stained with DAPI and mounted with Fluoromount™ Aqueous Mounting medium. Images were acquired in a confocal microscope at 20x or 40x magnification (LSM 880, LSM 980; Carl Zeiss, Germany)).

Immunohistochemical staining

Human heart paraffin sections were deparaffinized and submitted to antigen retrieval in sodium citrate buffer (pH 6) for 20 min at 90°C. Then, sections were washed and immersed in 3% hydrogen peroxide in methanol for 15 min. Sections were then incubated with blocking solution containing 5% goat serum, 1% BSA and 0.1% cold fish skin gelatin in PBS for 1 h at RT, and afterwards with the primary antibodies against CD14 (1:100) or CCR2 (1:100) overnight at 4°C. After washing, sections were incubated with HRP-conjugated goat anti-rabbit secondary antibody (1:1000) in the dark for 1 h at RT. Finally, sections were washed, stained with Mayer's hematoxylin for 5 min, dried and mounted with Fluoromount™ Aqueous Mounting medium. Images were acquired at 20x and 40x magnifications using Axio Imager 2 (Zeiss, Germany).

RNA-fluorescence in situ hybridization (RNA-FISH)

The RNAscope Multiplex Fluorescent v2 was used on mouse flash-frozen and human paraffin sections, according to the manufacturer's instructions. Mouse flash-frozen sections were first fixed with 4% PFA at 4°C for 30 min and dehydrated stepwise in 50% ethanol, 70% ethanol and 100% ethanol. Then, sections were incubated with protease IV at RT for 30 min and hybridized with probes specific to *Mmp9*, *Collagen I*, *Vimentin* or *Cx3cr1* at 40°C for 2 h. Human paraffin sections were deparaffinized by incubating with Xylene for 10 min and then 100% ethanol for 5 min. Then, sections were incubated with Hydrogen peroxide for 10 min at RT and antigen retrieval was done by incubating sections with RNAscope® Retrieval Reagents at 95°C for 15 min. Sections were then incubated with protease III at RT for 30 min and hybridized with probes specific to MMP9 and CD14 at 40°C for 2 h. After hybridization, all sections (mouse and humans) were washed and incubated with a series of pre-amplifier and amplifier reagents, fluorophores and the HRP blocker at 40°C for 15–30 min each, according to manufacturers' protocols. To detect the eGFP+ signal, specific mouse sections were further incubated with 0.5% Triton X-100 for 5 min, blocked with 4% BSA for 10 min

at RT and incubated with 1:200 anti-GFP Nanobody conjugated to a fluorescent dye (GFP-booster) at 4°C overnight. Finally, all sections were then stained with DAPI and mounted with Fluoromount™ Aqueous Mounting medium. Images were acquired at 20x and 63x magnifications (Leica, Dmi8, Germany).

MMP9 gelatin zymography

Mice were deeply anaesthetized and euthanized as described above. Hearts were immediately extracted and flash-frozen on powdered dry ice. Frozen hearts were placed in microcentrifuge tubes containing RIPA lysis/extraction buffer already supplemented with protease/phosphatase inhibitor and 5mm steel beads, and placed on a tissue lyser (Qiagen, Germany) at 50HZ for 10 min. The total protein content of each sample was measured using the Pierce BCA protein assay kit. Same amounts of protein were loaded and fractioned on 10% Zymogram Plus (Gelatin) gels, according to the manufacturer's instructions. Gels were then incubated in Zymogram Renaturing Buffer and in Zymogram Developing Buffer for 30 min each, both at RT with gentle agitation. Then, gels were incubated in Zymogram Developing Buffer overnight at 37°C and stained with the colloidal blue staining kit for 3 hours at RT. Gels were washed in water overnight and imaged with a gel scanner (Epson, Germany). Images were analyzed with ImageJ.

Blood urea measurement

Plasma was collected from stroke and control mice one month post-stroke and frozen at -80°C until further use. Frozen plasma was thawed on ice and a commercial urea assay kit (Abcam, USA) was used for evaluating the concentration of the blood urea, according to manufacturer's instructions. All samples were run in duplicates and all duplicates showed a coefficient of variation <15%.

Enzyme linked immunosorbent assay (ELISA)

Total pro-MMP9 concentrations were measured in heart protein lysates using the pro-MMP9 Mouse ELISA kit, according to manufacturer's (ThermoFisher) instructions. Pro-MMP9 concentrations are expressed per microgram of total protein content in the heart, measured using the Pierce BCA protein assay kit and following manufacturer's instructions. Blood IL-1 β and IL-6 concentrations were assessed respectively with Mouse IL-1 beta SimpleStep Elisa kit (Abcam) and Mouse IL-6 ELISA Kit (Abcam), according to manufacturer's instructions. Briefly, mouse blood was extracted using EDTA tubes at different timepoints after stroke then

centrifuged at 3000 x g for 15 min. The plasma was collected and stored in -80 °C until running the assay. All samples were run in duplicates and all duplicates showed a coefficient of variation <15%.

qPCR

Total RNA from FACS-sorted cells was extracted using Arcturus® PicoPure® RNA Isolation Kit, according to the manufacturer's instructions. Reverse transcription to cDNA was performed using High-Capacity Reverse Transcription Kit. qRT-PCR was performed with a standard SYBR-Green PCR kit protocol as previously described.²⁵ Relative changes on *Mmp9* gene expression levels were normalized to *Ppia* gene expression levels by using the $2^{-\Delta\Delta Ct}$ method.²⁶

Splenocytes isolation and incubation with CVC

Mice were deeply anaesthetized and euthanized as described above. Spleens were immediately removed and cell suspensions were prepared as previously described. Splenocytes were incubated for 2h at 37°C with CVC at different concentrations (0 µM, 5µM, 10 µM and 100 µM). Afterwards, cells were washed and stained with surface markers for flow cytometry as described above.

BMDM and primary monocyte isolation

Bone marrow derived macrophage (BMDM) cells are generated from mouse tibia and femur. After flushed out from both femurs and tibias, bone marrow cells were filtered through 40µm cell strainers to obtain single cell suspensions. Subsequently, cells were resuspended in DMEM (Gibco), supplemented with 10% fetal bovine serum (FBS) (Gibco), 1% Gentamycin (ThermoFisher Scientific) and 20 % L929 cell-conditioned medium (LCM) to promote differentiation into macrophages. A total of 5×10^5 cells were seeded per well and cultured for 7 days at 37 °C with 5% CO₂.

Primary monocytes were obtained from isolated cell suspensions using the negative selection kit EasySep monocyte isolation kit (StemCell). Sorted monocytes were then plated in 12-well plates at 5×10^5 cells per well in DMEM (Gibco), supplemented with 10% FBS (Gibco) and 1% Gentamycin (Thermo Scientific) and cultured for 24h at 37 °C with 5% CO₂.

BMDM and primary monocyte phagocytosis assay

Fully differentiated BMDMs or cultured primary monocytes were primed with 100 ng/ml LPS for 4h. Then, cells were treated with 1 μ g/ml (BMDMs) or 5 μ g/ml (monocytes) pHrodo Zymosan (Thermo Fisher, US) for 30 min. Zymosan uptake by cells was analyzed via flow cytometry, as previously described.

BMDM stimulation with IL-1 β

Fully differentiated BMDM were treated with 5ng/ml or 50ng/ml of recombinant IL-1 β or vehicle for 6h at 37°C with 5% CO₂. Cells were then washed and harvested and analyzed by western blot.

Western blotting analysis

BMDM were lysed with RIPA lysis/extraction buffer with added protease/phosphatase inhibitor (Thermo Fisher Scientific). Total protein was quantified using the Pierce BCA protein assay kit (Thermo Fisher Scientific). Whole cell lysates were fractionated by SDS-PAGE and transferred onto a polyvinylidene difluoride membrane (BioRad). After blocking for 1 hour in TBS-T (TBS with 0.1 % Tween 20, pH 8.0) containing 4 % skin mile powder (Sigma), the membrane was incubated with the primary antibodies against following antibodies: rabbit anti-cJun/phospho-cJun (1:1000; Cell signalling), rabbit anti-actin (1:2000; Sigma), rabbit APOE (1: 5000, Invitrogen), mouse anti- β -Tubulin (1:2000, Sigma Aldrich) and rabbit anti-LPL (1:1000, Invitrogen, US). Membranes were washed three times with TBS-T and incubated for 1 hour with HRP-conjugated anti-rabbit or anti-mouse secondary antibodies (1:5000, Dako) at RT. Membranes were developed using ECL substrate (Millipore, US) and acquired via the Vilber Fusion Fx7 imaging system.

Bulk mRNA sequencing of human heart samples

Human heart paraffin sections were used to retrieve the PFA-cross-linked mRNA as previously described.²⁷ In brief, PFA-fixed paraffin-embedded hearth tissue sections were scratched from each slide using a stereomicroscope (Olympus SZ51, Model# 1111260100), collected in cold PKD buffer supplemented with proteinase K solution and snap-frozen in liquid nitrogen until further use. To prepare the Smartseq2 libraries, samples were thawed at RT for 3 min and incubated at 56°C in a thermal cycler (lid temperature 66°C), for 4 h or until tissue was completely dissolved. Samples were then placed on ice and incubated at 56°C for 1 min with dT25 magnetic beads to reverse crosslinked samples. Samples were incubated at

RT to allow mRNA hybridization and washed with 1x hybridization buffer (HB), containing 2x SSPE, 0.05% Tween-20 and 0.05% RNase Inhibitor. Samples were then washed with PBS with 0.1% RNase Inhibitor and incubated with RNase-free water for 2 min at 80°C to elute mRNA. Smartseq2 libraries were prepared from 1 ng mRNA, as previously described. Libraries were sequenced 2x60 reads base pairs paired-end on an Illumina NextSeq 1000 to a depth of 300,000-600,000 reads/sample.

Bulk mRNA sequencing data analysis

FastQC was used to check the quality of fastq files. Low-quality reads and adapters were trimmed using Cutadapt using the following parameters: (1) reads <20 bp, and (2) quality cutoff of 20. The trimmed FASTQ files were mapped to the mm10 reference genome using STAR. The mapped reads (of lesion tissue sections) belonging to the same slide were merged using the merge BAM files tool in Galaxy version 4. To quantify the number of reads mapping to the exons of each gene, featureCounts program was used. Data was further analyzed in R. As quality control steps, the following samples were filtered out for further analysis: (1) Samples with a high percentage of mitochondrial genes (>20%); samples with a high percentage of ribosomal genes (>8%); (3) very highly-expressed genes with more than 20,000 counts; and (4) genes that are expressed in less than 5 samples with more than 1 count. Hereafter, raw gene counts were normalized to stabilize variance (regularized logarithm method) and differentially expressed genes were identified using the DESeq2 package in R.

QUANTIFICATION AND STATISTICAL ANALYSIS

Data were analyzed using GraphPad Prism version 9.0. All summary data are expressed as the mean \pm standard deviation (s.d.), unless indicated otherwise. Normality was assessed in all datasets using the Shapiro-Wilk normality test. Normally-distributed data were analyzed using a two-way Student's t test (for 2 groups) or ANOVA (for > 2 groups). Data with a no normal distribution were analyzed using the Mann-Whitney U test (for 2 groups) or Kruskal-Wallis test (H test, for > 2 groups). Multiple comparison adjusted p values were computed using Bonferroni correction or Dunn's multiple comparison tests. A p value < 0.05 was considered statistically significant.

Supplemental information

Table S1. Echocardiogram measurements, related to Figure 2.

Table S2. Cardiac conduction properties, related to Figure 2.

Table S3. Demographical and clinical characteristics of stroke patients from whom the myocardial autopsy samples were collected, related to Figure 3.

Table S4. Peak-to-gene annotations, related to Figure 6.

REFERENCES

1. Simats, A., and Liesz, A. (2022). Systemic inflammation after stroke: implications for post-stroke comorbidities. *EMBO Mol Med* 14. 10.15252/emmm.202216269.
2. Roth, S., Cao, J., Singh, V., Tiedt, S., Hundeshagen, G., Li, T., Boehme, J.D., Chauhan, D., Zhu, J., Ricci, A., et al. (2021). Post-injury immunosuppression and secondary infections are caused by an AIM2 inflammasome-driven signaling cascade. *Immunity* 54, 648-659.e8. 10.1016/j.immuni.2021.02.004.
3. Iadecola, C., Buckwalter, M.S., and Anrather, J. (2020). Immune responses to stroke: Mechanisms, modulation, and therapeutic potential. *Journal of Clinical Investigation* 130, 2777–2788. 10.1172/JCI135530.
4. Liesz, A., Rüger, H., Purucker, J., Zorn, M., Dalpke, A., Möhlenbruch, M., Englert, S., Nawroth, P.P., and Veltkamp, R. (2013). Stress Mediators and Immune Dysfunction in Patients with Acute Cerebrovascular Diseases. *PLoS ONE* 8, 1–10. 10.1371/journal.pone.0074839.
5. Stanne, T.M., Angerfors, A., Andersson, B., Brännmark, C., Holmegaard, L., and Jern, C. (2022). Longitudinal Study Reveals Long-Term Proinflammatory Proteomic Signature After Ischemic Stroke Across Subtypes. *Stroke*, 1–12. 10.1161/STROKEAHA.121.038349.
6. Roth, S., Singh, V., Tiedt, S., Schindler, L., Huber, G., Geerlof, A., Antoine, D.J., Anfray, A., Orset, C., Gauberti, M., et al. (2018). Brain-released alarmins and stress response synergize in accelerating atherosclerosis progression after stroke. *Science Translational Medicine* 10, 1–12. 10.1126/scitranslmed.aao1313.
7. Holmegaard, L., Stanne, T.M., Andreasson, U., Zetterberg, H., Blennow, K., Blomstrand, C., Jood, K., and Jern, C. (2021). Proinflammatory protein signatures in cryptogenic and large artery atherosclerosis stroke. *Acta Neurologica Scandinavica* 143, 303–312. 10.1111/ane.13366.
8. Tatemichi, T.K., Paik, M., Bagiella, E., Desmond, D.W., Pirro, M., and Hanzawa, L.K. (1994). Dementia after stroke is a predictor of long-term survival. *Stroke* 25, 1915–1919. 10.1161/01.STR.25.10.1915.
9. Braga, G.P., Gonçalves, R.S., Minicucci, M.F., Bazan, R., and Zornoff, L.A.M. (2020). Strain pattern and T-wave alterations are predictors of mortality and poor neurologic outcome following stroke. *Clinical Cardiology* 43, 568–573. 10.1002/clc.23348.
10. Prosser, J., MacGregor, L., Lees, K.R., Diener, H.C., Hacke, W., and Davis, S. (2007). Predictors of early cardiac morbidity and mortality after ischemic stroke. *Stroke* 38, 2295–2302. 10.1161/STROKEAHA.106.471813.
11. Suissa, L., Panicucci, E., Perot, C., Romero, G., Gazzola, S., Laksiri, N., Rey, C., Doche, E., Mahagne, M.-H., Pelletier, J., et al. (2020). Effect of hyperglycemia on stroke outcome is not homogeneous to all patients treated with mechanical thrombectomy. *Clinical Neurology and Neurosurgery* 194, 105750. 10.1016/j.clineuro.2020.105750.
12. Hackett, M.L., and Pickles, K. (2014). Part I: frequency of depression after stroke: an updated systematic review and meta-analysis of observational studies. *Int J Stroke* 9, 1017–1025. 10.1111/ijss.12357.
13. Netea, M.G., Joosten, L.A.B., Latz, E., Mills, K.H.G., Natoli, G., Stunnenberg, H.G., O'Neill, L.A.J., and Xavier, R.J. (2016). Trained immunity: A program of innate immune memory in health and disease. *Science (New York, N.Y.)* 352, aaf1098. 10.1126/science.aaf1098.
14. Netea, M.G., Domínguez-Andrés, J., Barreiro, L.B., Chavakis, T., Divangahi, M., Fuchs, E., Joosten, L.A.B., van der Meer, J.W.M., Mhlanga, M.M., Mulder, W.J.M., et al. (2020). Defining trained immunity and its role in health and disease. *Nature Reviews Immunology* 20, 375–388. 10.1038/s41577-020-0285-6.

15. Ochando, J., Fayad, Z.A., Madsen, J.C., Netea, M.G., and Mulder, W.J.M. (2020). Trained immunity in organ transplantation. *Am J Transplant* 20, 10–18. 10.1111/ajt.15620.
16. Leung, Y.T., Shi, L., Maurer, K., Song, L., Zhang, Z., Petri, M., and Sullivan, K.E. (2015). Interferon regulatory factor 1 and histone H4 acetylation in systemic lupus erythematosus. *Epigenetics* 10, 191–199. 10.1080/15592294.2015.1009764.
17. Li, X., Wang, H., Yu, X., Saha, G., Kalafati, L., Ioannidis, C., Mitroulis, I., Netea, M.G., Chavakis, T., and Hajishengallis, G. (2022). Maladaptive innate immune training of myelopoiesis links inflammatory comorbidities. *Cell* 185, 1709–1727.e18. 10.1016/j.cell.2022.03.043.
18. Murphy, A.J., and Tall, A.R. (2016). Disordered haematopoiesis and athero-thrombosis. *Eur Heart J* 37, 1113–1121. 10.1093/eurheartj/ehv718.
19. Winklewski, P.J., Radkowski, M., and Demkow, U. (2014). Cross-talk between the inflammatory response, sympathetic activation and pulmonary infection in the ischemic stroke. *Journal of Neuroinflammation* 11, 4–11. 10.1186/s12974-014-0213-4.
20. Seifert, H.A., and Offner, H. (2018). The splenic response to stroke: From rodents to stroke subjects. *Journal of Neuroinflammation* 15, 1–7. 10.1186/s12974-018-1239-9.
21. Austin, V., Ku, J.M., Miller, A.A., and Vlahos, R. (2019). Ischaemic stroke in mice induces lung inflammation but not acute lung injury. *Scientific Reports* 9, 1–10. 10.1038/s41598-019-40392-1.
22. Llovera, G., Hofmann, K., Roth, S., Salas-Pédomo, A., Ferrer-Ferrer, M., Perego, C., Zanier, E.R., Mamrak, U., Rex, A., Party, H., et al. (2015). Results of a preclinical randomized controlled multicenter trial (pRCT): Anti-CD49d treatment for acute brain ischemia. *Science translational medicine* 7, 299ra121. 10.1126/scitranslmed.aaa9853.
23. Ginhoux, F., Schultze, J.L., Murray, P.J., Ochando, J., and Biswas, S.K. (2016). New insights into the multidimensional concept of macrophage ontogeny, activation and function. *Nature Immunology* 17, 34–40. 10.1038/ni.3324.
24. Hoyer, F.F., Naxerova, K., Schloss, M.J., Hulsmans, M., Nair, A.V., Dutta, P., Calcagno, D.M., Herisson, F., Anzai, A., Sun, Y., et al. (2019). Tissue-Specific Macrophage Responses to Remote Injury Impact the Outcome of Subsequent Local Immune Challenge. *Immunity* 51, 899–914.e7. 10.1016/j.immuni.2019.10.010.
25. Paulus, W.J., and Tschöpe, C. (2013). A Novel Paradigm for Heart Failure With Preserved Ejection Fraction. *Journal of the American College of Cardiology* 62, 263–271. 10.1016/j.jacc.2013.02.092.
26. Sharma, K., and Kass, D.A. (2014). Heart Failure With Preserved Ejection Fraction: Mechanisms, Clinical Features, and Therapies. *Circ Res* 115, 79–96. 10.1161/CIRCRESAHA.115.302922.
27. Hulsmans, M., Schloss, M.J., Lee, I.-H., Bapat, A., Iwamoto, Y., Vinegoni, C., Paccalet, A., Yamazoe, M., Grune, J., Pabel, S., et al. (2023). Recruited macrophages elicit atrial fibrillation. *Science* 381, 231–239. 10.1126/science.abq3061.
28. Epelman, S., Lavine, K.J., Beaudin, A.E., Sojka, D.K., Carrero, J.A., Calderon, B., Brija, T., Gautier, E.L., Ivanov, S., Satpathy, A.T., et al. (2014). Embryonic and adult-derived resident cardiac macrophages are maintained through distinct mechanisms at steady state and during inflammation. *Immunity* 40, 91–104. 10.1016/j.immuni.2013.11.019.
29. Park, M.D., Silvin, A., Ginhoux, F., and Merad, M. (2022). Macrophages in health and disease. *Cell* 185, 4259–4279. 10.1016/j.cell.2022.10.007.
30. Stik, G., Vidal, E., Barrero, M., Cuartero, S., Vila-Casadesús, M., Mendieta-Esteban, J., Tian, T.V., Choi, J., Berenguer, C., Abad, A., et al. (2020). CTCF is dispensable for immune cell transdifferentiation but facilitates an acute inflammatory response. *Nat Genet* 52, 655–661. 10.1038/s41588-020-0643-0.

31. Jaitin, D.A., Weiner, A., Yofe, I., Lara-Astiaso, D., Keren-Shaul, H., David, E., Salame, T.M., Tanay, A., Van Oudenaarden, A., and Amit, I. (2016). Dissecting Immune Circuits by Linking CRISPR-Pooled Screens with Single-Cell RNA-Seq. *Cell* *167*, 1883–1896.e15. 10.1016/j.cell.2016.11.039.
32. Yuan, Y., Fan, G., Liu, Y., Liu, L., Zhang, T., Liu, P., Tu, Q., Zhang, X., Luo, S., Yao, L., et al. (2022). The transcription factor KLF14 regulates macrophage glycolysis and immune function by inhibiting HK2 in sepsis. *Cell Mol Immunol* *19*, 504–515. 10.1038/s41423-021-00806-5.
33. Yang, Z.-F., Drumea, K., Cormier, J., Wang, J., Zhu, X., and Rosmarin, A.G. (2011). GABP transcription factor is required for myeloid differentiation, in part, through its control of Gfi-1 expression. *Blood* *118*, 2243–2253. 10.1182/blood-2010-07-298802.
34. Chen, S., Yang, J., Wei, Y., and Wei, X. (2020). Epigenetic regulation of macrophages: from homeostasis maintenance to host defense. *Cellular and Molecular Immunology* *17*, 36–49. 10.1038/s41423-019-0315-0.
35. Yoshida, K., and Ishii, S. (2016). Innate immune memory via ATF7-dependent epigenetic changes. *Cell Cycle* *15*, 3–4. 10.1080/15384101.2015.1112687.
36. Li, W., Moorlag, S.J.C.F.M., Koeken, V.A.C.M., Röring, R.J., De Bree, L.C.J., Mourits, V.P., Gupta, M.K., Zhang, B., Fu, J., Zhang, Z., et al. (2023). A single-cell view on host immune transcriptional response to in vivo BCG-induced trained immunity. *Cell Reports* *42*, 112487. 10.1016/j.celrep.2023.112487.
37. Schep, A.N., Wu, B., Buenrostro, J.D., and Greenleaf, W.J. (2017). chromVAR: inferring transcription-factor-associated accessibility from single-cell epigenomic data. *Nat Methods* *14*, 975–978. 10.1038/nmeth.4401.
38. Omatsu, Y., Aiba, S., Maeta, T., Higaki, K., Aoki, K., Watanabe, H., Kondoh, G., Nishimura, R., Takeda, S., Chung, U., et al. (2022). Runx1 and Runx2 inhibit fibrotic conversion of cellular niches for hematopoietic stem cells. *Nat Commun* *13*, 2654. 10.1038/s41467-022-30266-y.
39. Ciau-Uitz, A., Wang, L., Patient, R., and Liu, F. (2013). ETS transcription factors in hematopoietic stem cell development. *Blood Cells Mol Dis* *51*, 248–255. 10.1016/j.bcmd.2013.07.010.
40. Ohlsson, R., Renkawitz, R., and Lobanenkov, V. (2001). CTCF is a uniquely versatile transcription regulator linked to epigenetics and disease. *Trends Genet* *17*, 520–527. 10.1016/s0168-9525(01)02366-6.
41. Baillie, J.K., Arner, E., Daub, C., De Hoon, M., Itoh, M., Kawaji, H., Lassmann, T., Carninci, P., Forrest, A.R.R., Hayashizaki, Y., et al. (2017). Analysis of the human monocyte-derived macrophage transcriptome and response to lipopolysaccharide provides new insights into genetic aetiology of inflammatory bowel disease. *PLoS Genet* *13*, e1006641. 10.1371/journal.pgen.1006641.
42. An, Y., Ni, Y., Xu, Z., Shi, S., He, J., Liu, Y., Deng, K.-Y., Fu, M., Jiang, M., and Xin, H.-B. (2020). TRIM59 expression is regulated by Sp1 and Nrf1 in LPS-activated macrophages through JNK signaling pathway. *Cellular Signalling* *67*, 109522. 10.1016/j.cellsig.2019.109522.
43. Nikolic, T., Movita, D., Lambers, M.E., De Almeida, C.R., Biesta, P., Kreefft, K., De Bruijn, M.J., Bergen, I., Galjart, N., Boonstra, A., et al. (2014). The DNA-binding factor Ctf critically controls gene expression in macrophages. *Cell Mol Immunol* *11*, 58–70. 10.1038/cmi.2013.41.
44. Dekkers, K.F., Neele, A.E., Jukema, J.W., Heijmans, B.T., and De Winther, M.P.J. (2019). Human monocyte-to-macrophage differentiation involves highly localized gain and loss of DNA methylation at transcription factor binding sites. *Epigenetics & Chromatin* *12*, 34. 10.1186/s13072-019-0279-4.
45. Liao, J., Humphrey, S.E., Poston, S., and Taparowsky, E.J. (2011). Batf Promotes Growth Arrest and Terminal Differentiation of Mouse Myeloid Leukemia Cells. *Molecular Cancer Research* *9*, 350–363. 10.1158/1541-7786.MCR-10-0375.

46. Behmoaras, J., Bhargal, G., Smith, J., McDonald, K., Mutch, B., Lai, P.C., Domin, J., Game, L., Salama, A., Foxwell, B.M., et al. (2008). Jund is a determinant of macrophage activation and is associated with glomerulonephritis susceptibility. *Nat Genet* 40, 553–559. 10.1038/ng.137.
47. Ridker, P.M., MacFadyen, J.G., Thuren, T., Everett, B., Libby, P., Glynn, R., Ridker, P., Lorenzatti, A., Krum, H., Varigos, J., et al. (2017). Effect of interleukin-1 β inhibition with canakinumab on incident lung cancer in patients with atherosclerosis: exploratory results from a randomised, double-blind, placebo-controlled trial. *The Lancet* 390, 1833–1842. 10.1016/S0140-6736(17)32247-X.
48. Thompson, M., Saag, M., DeJesus, E., Gathe, J., Lalezari, J., Landay, A.L., Cade, J., Enejosa, J., Lefebvre, E., and Feinberg, J. (2016). A 48-week randomized phase 2b study evaluating cenicriviroc versus efavirenz in treatment-naïve HIV-infected adults with C-C chemokine receptor type 5-tropic virus. *AIDS* 30, 869–878. 10.1097/QAD.0000000000000988.
49. Sherman, K.E., Abdel-Hameed, E., Rouster, S.D., Shata, M.T.M., Blackard, J.T., Safaie, P., Kroner, B., Preiss, L., Horn, P.S., and Kottlil, S. (2019). Improvement in Hepatic Fibrosis Biomarkers Associated With Chemokine Receptor Inactivation Through Mutation or Therapeutic Blockade. *Clin Infect Dis* 68, 1911–1918. 10.1093/cid/ciy807.
50. Friedman, S.L., Ratziu, V., Harrison, S.A., Abdelmalek, M.F., Aithal, G.P., Caballeria, J., Francque, S., Farrell, G., Kowdley, K.V., Craxi, A., et al. (2018). A randomized, placebo-controlled trial of cenicriviroc for treatment of nonalcoholic steatohepatitis with fibrosis. *Hepatology* 67, 1754–1767. 10.1002/hep.29477.
51. Dziedzic, T. (2015). Systemic inflammation as a therapeutic target in acute ischemic stroke. *Expert review of neurotherapeutics* 15, 523–531. 10.1586/14737175.2015.1035712.
52. Anrather, J., and Iadecola, C. (2016). Inflammation and Stroke: An Overview. *Neurotherapeutics* 13, 661–670. 10.1007/s13311-016-0483-x.
53. Chugh, S.S., Roth, G.A., Gillum, R.F., and Mensah, G.A. (2014). Global burden of atrial fibrillation in developed and developing nations. *Glob Heart* 9, 113–119. 10.1016/j.ghart.2014.01.004.
54. Kim, W., and Kim, E.J. (2018). Heart failure as a risk factor for stroke. *Journal of Stroke* 20, 33–45. 10.5853/jos.2017.02810.
55. Kallmünzer, B., Breuer, L., Kahl, N., Bobinger, T., Raaz-Schrauder, D., Huttner, H.B., Schwab, S., and Köhrmann, M. (2012). Serious cardiac arrhythmias after stroke: Incidence, time course, and predictors—a systematic, prospective analysis. *Stroke* 43, 2892–2897. 10.1161/STROKEAHA.112.664318.
56. Buckley, B.J.R., Harrison, S.L., Hill, A., Underhill, P., Lane, D.A., and Lip, G.Y.H. (2022). Stroke-Heart Syndrome: Incidence and Clinical Outcomes of Cardiac Complications Following Stroke. *Stroke* 53, 1759–1763. 10.1161/STROKEAHA.121.037316.
57. Ruthirago, D., Julayanont, P., Tantrachoti, P., Kim, J., and Nugent, K. (2016). Cardiac Arrhythmias and Abnormal Electrocardiograms after Acute Stroke. *American Journal of the Medical Sciences* 351, 112–118. 10.1016/j.amjms.2015.10.020.
58. Bieber, M., Werner, R.A., Tanai, E., Hofmann, U., Higuchi, T., Schuh, K., Heuschmann, P.U., Frantz, S., Ritter, O., Kraft, P., et al. (2017). Stroke-induced chronic systolic dysfunction driven by sympathetic overactivity. *Annals of Neurology* 82, 729–743. 10.1002/ana.25073.
59. Veltkamp, R., Uhlmann, S., Marinescu, M., Sticht, C., Finke, D., Gretz, N., Gröne, H.J., Katus, H.A., Backs, J., and Lehmann, L.H. (2019). Experimental ischaemic stroke induces transient cardiac atrophy and dysfunction. *Journal of Cachexia, Sarcopenia and Muscle* 10, 54–62. 10.1002/jcsm.12335.
60. Heuschmann, P.U., Montellano, F.A., Ungethüm, K., Rücker, V., Wiedmann, S., Mackenrodt, D., Quilitzsch, A., Ludwig, T., Kraft, P., Albert, J., et al. (2021). Prevalence and determinants of systolic and diastolic cardiac dysfunction and heart failure in acute ischemic stroke patients: The SICFAIL study. *ESC Heart Fail* 8, 1117–1129. 10.1002/ehf2.13145.

61. Jeong, E.-M., and Dudley Jr, S.C. (2015). Diastolic Dysfunction: – Potential New Diagnostics and Therapies –. *Circ J* 79, 470–477. 10.1253/circj.CJ-15-0064.
62. Thomas, L., Marwick, T.H., Popescu, B.A., Donal, E., and Badano, L.P. (2019). Left Atrial Structure and Function, and Left Ventricular Diastolic Dysfunction: JACC State-of-the-Art Review. *J Am Coll Cardiol* 73, 1961–1977. 10.1016/j.jacc.2019.01.059.
63. Kirchgesner, J., Beaugerie, L., Carrat, F., Andersen, N.N., Jess, T., Schwarzingner, M., Bouvier, A.M., Buisson, A., Carbonnel, F., Cosnes, J., et al. (2018). Increased risk of acute arterial events in young patients and severely active IBD: A nationwide French cohort study. *Gut* 67, 1261–1268. 10.1136/gutjnl-2017-314015.
64. Moorlag, S.J.C.F.M., Khan, N., Novakovic, B., Kaufmann, E., Jansen, T., Van Crevel, R., Divangahi, M., and Netea, M.G. (2020). β -Glucan Induces Protective Trained Immunity against Mycobacterium tuberculosis Infection: A Key Role for IL-1. *Cell Reports* 31, 107634. 10.1016/j.celrep.2020.107634.
65. Mitroulis, I., Ruppova, K., Wang, B., Chen, L.S., Grzybek, M., Grinenko, T., Eugster, A., Troullinaki, M., Palladini, A., Kourtzelis, I., et al. (2018). Modulation of Myelopoiesis Progenitors Is an Integral Component of Trained Immunity. *Cell* 172, 147–161.e12. 10.1016/j.cell.2017.11.034.
66. Georgakis, M.K., Bernhagen, J., Heitman, L.H., Weber, C., and Dichgans, M. (2022). Targeting the CCL2–CCR2 axis for atheroprotection. *European Heart Journal* 43, 1799–1808. 10.1093/eurheartj/ehac094.
67. Stuart, T., Butler, A., Hoffman, P., Hafemeister, C., Papalexi, E., Mauck, W.M., Hao, Y., Stoeckius, M., Smibert, P., and Satija, R. (2019). Comprehensive Integration of Single-Cell Data. *Cell* 177, 1888–1902.e21. 10.1016/j.cell.2019.05.031.
68. Stuart, T., Srivastava, A., Madad, S., Lareau, C.A., and Satija, R. (2021). Single-cell chromatin state analysis with Signac. *Nat Methods* 18, 1333–1341. 10.1038/s41592-021-01282-5.
69. Cao, J., Spielmann, M., Qiu, X., Huang, X., Ibrahim, D.M., Hill, A.J., Zhang, F., Mundlos, S., Christiansen, L., Steemers, F.J., et al. (2019). The single-cell transcriptional landscape of mammalian organogenesis. *Nature* 566, 496–502. 10.1038/s41586-019-0969-x.
70. Granja, J.M., Corces, M.R., Pierce, S.E., Bagdatli, S.T., Choudhry, H., Chang, H.Y., and Greenleaf, W.J. (2021). ArchR is a scalable software package for integrative single-cell chromatin accessibility analysis. *Nat Genet* 53, 403–411. 10.1038/s41588-021-00790-6.
71. Lange, M., Bergen, V., Klein, M., Setty, M., Reuter, B., Bakhti, M., Lickert, H., Ansari, M., Schniering, J., Schiller, H.B., et al. (2022). CellRank for directed single-cell fate mapping. *Nat Methods* 19, 159–170. 10.1038/s41592-021-01346-6.
72. Jin, S., Guerrero-Juarez, C.F., Zhang, L., Chang, I., Ramos, R., Kuan, C.-H., Myung, P., Plikus, M.V., and Nie, Q. (2021). Inference and analysis of cell-cell communication using CellChat. *Nat Commun* 12, 1088. 10.1038/s41467-021-21246-9.
73. Machlab, D., Burger, L., Soneson, C., Rijli, F.M., Schübeler, D., and Stadler, M.B. (2022). monaLisa: an R/Bioconductor package for identifying regulatory motifs. *Bioinformatics* 38, 2624–2625. 10.1093/bioinformatics/btac102.
74. Lun, A.T.L., and Smyth, G.K. (2016). csaw: a Bioconductor package for differential binding analysis of ChIP-seq data using sliding windows. *Nucleic Acids Research* 44, e45–e45. 10.1093/nar/gkv1191.
75. Simon Andrews (2010). FastQC: a quality control tool for high throughput sequence data.
76. Dobin, A., Davis, C.A., Schlesinger, F., Drenkow, J., Zaleski, C., Jha, S., Batut, P., Chaisson, M., and Gingeras, T.R. (2013). STAR: ultrafast universal RNA-seq aligner. *Bioinformatics* 29, 15–21. 10.1093/bioinformatics/bts635.

77. Marcel Martin (2011). Cutadapt Removes Adapter Sequences From High-Throughput Sequencing Reads.
78. Liao, Y., Smyth, G.K., and Shi, W. (2014). featureCounts: an efficient general purpose program for assigning sequence reads to genomic features. *Bioinformatics* 30, 923–930. 10.1093/bioinformatics/btt656.
79. Love, M.I., Huber, W., and Anders, S. (2014). Moderated estimation of fold change and dispersion for RNA-seq data with DESeq2. *Genome Biol* 15, 550. 10.1186/s13059-014-0550-8.
80. Ge, S.X., Jung, D., and Yao, R. (2020). ShinyGO: a graphical gene-set enrichment tool for animals and plants. *Bioinformatics* 36, 2628–2629. 10.1093/bioinformatics/btz931.
81. Raudvere, U., Kolberg, L., Kuzmin, I., Arak, T., Adler, P., Peterson, H., and Vilo, J. (2019). g:Profiler: a web server for functional enrichment analysis and conversions of gene lists (2019 update). *Nucleic Acids Res* 47, W191–W198. 10.1093/nar/gkz369.
82. Nagueh, S.F., Smiseth, O.A., Appleton, C.P., Byrd, B.F., Dokainish, H., Edvardsen, T., Flachskampf, F.A., Gillebert, T.C., Klein, A.L., Lancellotti, P., et al. (2016). Recommendations for the Evaluation of Left Ventricular Diastolic Function by Echocardiography: An Update from the American Society of Echocardiography and the European Association of Cardiovascular Imaging. *Eur Heart J Cardiovasc Imaging* 17, 1321–1360. 10.1093/ehjci/jew082.
83. Llovera, G., Roth, S., Plesnila, N., Veltkamp, R., and Liesz, A. (2014). Modeling Stroke in Mice: Permanent Coagulation of the Distal Middle Cerebral Artery Video Link. *J. Vis. Exp.* 517293791–51729. 10.3791/51729.
84. Tomsits, P., Volz, L., Xia, R., Chivukula, A., Schüttler, D., and Clauß, S. (2023). Medetomidine/midazolam/fentanyl narcosis alters cardiac autonomic tone leading to conduction disorders and arrhythmias in mice. *Lab Anim (NY)* 52, 85–92. 10.1038/s41684-023-01141-0.
85. Tomsits, P., Sharma Chivukula, A., Raj Chataut, K., Simahendra, A., Weckbach, L.T., Brunner, S., and Clauss, S. (2022). Real-Time Electrocardiogram Monitoring during Treadmill Training in Mice. *J Vis Exp.* 10.3791/63873.
86. Tomsits, P., Chataut, K.R., Chivukula, A.S., Mo, L., Xia, R., Schüttler, D., and Clauss, S. (2021). Analyzing Long-Term Electrocardiography Recordings to Detect Arrhythmias in Mice. *J Vis Exp.* 10.3791/62386.
87. Ramírez, F., Ryan, D.P., Grüning, B., Bhardwaj, V., Kilpert, F., Richter, A.S., Heyne, S., Dündar, F., and Manke, T. (2016). deepTools2: a next generation web server for deep-sequencing data analysis. *Nucleic Acids Res* 44, W160–W165. 10.1093/nar/gkw257.
88. Skene, P.J., Henikoff, J.G., and Henikoff, S. (2018). Targeted in situ genome-wide profiling with high efficiency for low cell numbers. *Nat Protoc* 13, 1006–1019. 10.1038/nprot.2018.015.
89. Kaya-Okur, H.S., Janssens, D.H., Henikoff, J.G., Ahmad, K., and Henikoff, S. (2020). Efficient low-cost chromatin profiling with CUT&Tag. *Nat Protoc* 15, 3264–3283. 10.1038/s41596-020-0373-x.
90. Yu, F., Sankaran, V.G., and Yuan, G.-C. (2021). CUT&RUNTools 2.0: a pipeline for single-cell and bulk-level CUT&RUN and CUT&Tag data analysis. *Bioinformatics* 38, 252–254. 10.1093/bioinformatics/btab507.
91. Stempor, P., and Ahringer, J. (2016). SeqPlots - Interactive software for exploratory data analyses, pattern discovery and visualization in genomics. *Wellcome Open Res* 1, 14. 10.12688/wellcomeopenres.10004.1.

5. References

- [1] Feigin VL, Brainin M, Norrving B, et al. World Stroke Organization (WSO): Global Stroke Fact Sheet 2022. *Int J Stroke*. 2022 Jan;17(1):18-29.
- [2] Collaborators GBDSRF. Global, regional, and national burden of stroke and its risk factors, 1990-2021: a systematic analysis for the Global Burden of Disease Study 2021. *Lancet Neurol*. 2024 Oct;23(10):973-1003.
- [3] Feigin VL, Brainin M, Norrving B, et al. World Stroke Organization: Global Stroke Fact Sheet 2025. *Int J Stroke*. 2025 Feb;20(2):132-144.
- [4] Salaudeen MA, Bello N, Danraka RN, et al. Understanding the Pathophysiology of Ischemic Stroke: The Basis of Current Therapies and Opportunity for New Ones. *Biomolecules*. 2024 Mar 4;14(3).
- [5] Gelderblom M, Leypoldt F, Steinbach K, et al. Temporal and spatial dynamics of cerebral immune cell accumulation in stroke. *Stroke*. 2009 May;40(5):1849-57.
- [6] Broughton BR, Reutens DC, Sobey CG. Apoptotic mechanisms after cerebral ischemia. *Stroke*. 2009 May;40(5):e331-9.
- [7] Powers WJ, Rabinstein AA, Ackerson T, et al. Guidelines for the Early Management of Patients With Acute Ischemic Stroke: 2019 Update to the 2018 Guidelines for the Early Management of Acute Ischemic Stroke: A Guideline for Healthcare Professionals From the American Heart Association/American Stroke Association. *Stroke*. 2019 Dec;50(12):e344-e418.
- [8] Powers WJ, Rabinstein AA, Ackerson T, et al. 2018 Guidelines for the Early Management of Patients With Acute Ischemic Stroke: A Guideline for Healthcare Professionals From the American Heart Association/American Stroke Association. *Stroke*. 2018 Mar;49(3):e46-e110.
- [9] Herpich F, Rincon F. Management of Acute Ischemic Stroke. *Crit Care Med*. 2020 Nov;48(11):1654-1663.
- [10] Bansal S, Sangha KS, Khatri P. Drug treatment of acute ischemic stroke. *Am J Cardiovasc Drugs*. 2013 Feb;13(1):57-69.
- [11] Shafi N, Kasner SE. Treatment of acute ischemic stroke: beyond thrombolysis and supportive care. *Neurotherapeutics*. 2011 Jul;8(3):425-33.
- [12] Diener HC, Hankey GJ. Primary and Secondary Prevention of Ischemic Stroke and Cerebral Hemorrhage: JACC Focus Seminar. *J Am Coll Cardiol*. 2020 Apr

- 21;75(15):1804-1818.
- [13] Mohan KM, Wolfe CD, Rudd AG, et al. Risk and cumulative risk of stroke recurrence: a systematic review and meta-analysis. *Stroke*. 2011 May;42(5):1489-94.
- [14] Touze E, Varenne O, Chatellier G, et al. Risk of myocardial infarction and vascular death after transient ischemic attack and ischemic stroke: a systematic review and meta-analysis. *Stroke*. 2005 Dec;36(12):2748-55.
- [15] Lovett JK, Coull AJ, Rothwell PM. Early risk of recurrence by subtype of ischemic stroke in population-based incidence studies. *Neurology*. 2004 Feb 24;62(4):569-73.
- [16] Shin S, Lee Y, Chang WH, et al. Multifaceted Assessment of Functional Outcomes in Survivors of First-time Stroke. *JAMA Netw Open*. 2022 Sep 1;5(9):e2233094.
- [17] Sposato LA, Hilz MJ, Aspberg S, et al. Post-Stroke Cardiovascular Complications and Neurogenic Cardiac Injury: JACC State-of-the-Art Review. *J Am Coll Cardiol*. 2020 Dec 8;76(23):2768-2785.
- [18] Billinger SA, Coughenour E, Mackay-Lyons MJ, et al. Reduced cardiorespiratory fitness after stroke: biological consequences and exercise-induced adaptations. *Stroke Res Treat*. 2012;2012:959120.
- [19] Rohweder G, Ellekjaer H, Salvesen O, et al. Functional outcome after common poststroke complications occurring in the first 90 days. *Stroke*. 2015 Jan;46(1):65-70.
- [20] Lavalley PC, Charles H, Albers GW, et al. Effect of atherosclerosis on 5-year risk of major vascular events in patients with transient ischaemic attack or minor ischaemic stroke: an international prospective cohort study. *Lancet Neurol*. 2023 Apr;22(4):320-329.
- [21] Jebari-Benslaiman S, Galicia-Garcia U, Larrea-Sebal A, et al. Pathophysiology of Atherosclerosis. *Int J Mol Sci*. 2022 Mar 20;23(6).
- [22] Libby P. Inflammation in atherosclerosis. *Nature*. 2002 Dec 19-26;420(6917):868-74.
- [23] Galkina E, Ley K. Immune and inflammatory mechanisms of atherosclerosis (*). *Annu Rev Immunol*. 2009;27:165-97.
- [24] Gleissner CA, Leitinger N, Ley K. Effects of native and modified low-density lipoproteins on monocyte recruitment in atherosclerosis. *Hypertension*. 2007 Aug;50(2):276-83.
- [25] Bennett MR, Sinha S, Owens GK. Vascular Smooth Muscle Cells in Atherosclerosis. *Circ Res*. 2016 Feb 19;118(4):692-702.
- [26] Sprague AH, Khalil RA. Inflammatory cytokines in vascular dysfunction and vascular disease. *Biochem Pharmacol*. 2009 Sep 15;78(6):539-52.

- [27] Badimon L, Padro T, Vilahur G. Atherosclerosis, platelets and thrombosis in acute ischaemic heart disease. *Eur Heart J Acute Cardiovasc Care*. 2012 Apr;1(1):60-74.
- [28] Bentzon JF, Otsuka F, Virmani R, et al. Mechanisms of plaque formation and rupture. *Circ Res*. 2014 Jun 6;114(12):1852-66.
- [29] Swirski FK, Nahrendorf M. Leukocyte behavior in atherosclerosis, myocardial infarction, and heart failure. *Science*. 2013 Jan 11;339(6116):161-6.
- [30] Iadecola C, Buckwalter MS, Anrather J. Immune responses to stroke: mechanisms, modulation, and therapeutic potential. *J Clin Invest*. 2020 Jun 1;130(6):2777-2788.
- [31] Elkind MS. Inflammatory mechanisms of stroke. *Stroke*. 2010 Oct;41(10 Suppl):S3-8.
- [32] Buckley BJR, Harrison SL, Hill A, et al. Stroke-Heart Syndrome: Incidence and Clinical Outcomes of Cardiac Complications Following Stroke. *Stroke*. 2022 May;53(5):1759-1763.
- [33] Chen Z, Venkat P, Seyfried D, et al. Brain-Heart Interaction: Cardiac Complications After Stroke. *Circ Res*. 2017 Aug 4;121(4):451-468.
- [34] Scheitz JF, Sposato LA, Schulz-Menger J, et al. Stroke-Heart Syndrome: Recent Advances and Challenges. *J Am Heart Assoc*. 2022 Sep 6;11(17):e026528.
- [35] Prosser J, MacGregor L, Lees KR, et al. Predictors of early cardiac morbidity and mortality after ischemic stroke. *Stroke*. 2007 Aug;38(8):2295-302.
- [36] Millionis H, Faouzi M, Cordier M, et al. Characteristics and early and long-term outcome in patients with acute ischemic stroke and low ejection fraction. *Int J Cardiol*. 2013 Sep 30;168(2):1082-7.
- [37] Sposato LA, Lam M, Allen B, et al. First-Ever Ischemic Stroke and Incident Major Adverse Cardiovascular Events in 93 627 Older Women and Men. *Stroke*. 2020 Feb;51(2):387-394.
- [38] Veltkamp R, Uhlmann S, Marinescu M, et al. Experimental ischaemic stroke induces transient cardiac atrophy and dysfunction. *J Cachexia Sarcopenia Muscle*. 2019 Feb;10(1):54-62.
- [39] Westendorp WF, Nederkoorn PJ, Vermeij JD, et al. Post-stroke infection: a systematic review and meta-analysis. *BMC Neurol*. 2011 Sep 20;11:110.
- [40] Rochester CL, Mohsenin V. Respiratory complications of stroke. *Semin Respir Crit Care Med*. 2002 Jun;23(3):248-60.
- [41] Johnson KG, Johnson DC. Frequency of sleep apnea in stroke and TIA patients: a meta-analysis. *J Clin Sleep Med*. 2010 Apr 15;6(2):131-7.

- [42] Patrizz A, El Hamamy A, Maniskas M, et al. Stroke-Induced Respiratory Dysfunction Is Associated With Cognitive Decline. *Stroke*. 2023 Jul;54(7):1863-1874.
- [43] Kim JB, Sig Choi J, Yu YM, et al. HMGB1, a novel cytokine-like mediator linking acute neuronal death and delayed neuroinflammation in the postischemic brain. *J Neurosci*. 2006 Jun 14;26(24):6413-21.
- [44] Kim ID, Lee H, Kim SW, et al. Alarmin HMGB1 induces systemic and brain inflammatory exacerbation in post-stroke infection rat model. *Cell Death Dis*. 2018 Apr 1;9(4):426.
- [45] Gruden G, Barutta F, Catto I, et al. Serum levels of heat shock protein 27 in patients with acute ischemic stroke. *Cell Stress Chaperones*. 2013 Jul;18(4):531-3.
- [46] Nash DL, Bellolio MF, Stead LG. S100 as a marker of acute brain ischemia: a systematic review. *Neurocrit Care*. 2008;8(2):301-7.
- [47] Roth S, Cao J, Singh V, et al. Post-injury immunosuppression and secondary infections are caused by an AIM2 inflammasome-driven signaling cascade. *Immunity*. 2021 Apr 13;54(4):648-659 e8.
- [48] Liesz A, Dalpke A, Mracsko E, et al. DAMP signaling is a key pathway inducing immune modulation after brain injury. *J Neurosci*. 2015 Jan 14;35(2):583-98.
- [49] Roth S, Singh V, Tiedt S, et al. Brain-released alarmins and stress response synergize in accelerating atherosclerosis progression after stroke. *Sci Transl Med*. 2018 Mar 14;10(432).
- [50] Sobowale OA, Parry-Jones AR, Smith CJ, et al. Interleukin-1 in Stroke: From Bench to Bedside. *Stroke*. 2016 Aug;47(8):2160-7.
- [51] Papadopoulos A, Palaiopoulos K, Bjorkbacka H, et al. Circulating Interleukin-6 Levels and Incident Ischemic Stroke: A Systematic Review and Meta-analysis of Prospective Studies. *Neurology*. 2022 Mar 8;98(10):e1002-e1012.
- [52] den Hertog HM, van Rossum JA, van der Worp HB, et al. C-reactive protein in the very early phase of acute ischemic stroke: association with poor outcome and death. *J Neurol*. 2009 Dec;256(12):2003-8.
- [53] Offner H, Subramanian S, Parker SM, et al. Experimental stroke induces massive, rapid activation of the peripheral immune system. *J Cereb Blood Flow Metab*. 2006 May;26(5):654-65.
- [54] Roth S, Yang J, Cramer JV, et al. Detection of cytokine-induced sickness behavior after ischemic stroke by an optimized behavioral assessment battery. *Brain Behav Immun*. 2021 Jan;91:668-672.

- [55] Basic Kes V, Simundic AM, Nikolac N, et al. Pro-inflammatory and anti-inflammatory cytokines in acute ischemic stroke and their relation to early neurological deficit and stroke outcome. *Clin Biochem*. 2008 Nov;41(16-17):1330-4.
- [56] Schulze J, Zierath D, Tanzi P, et al. Severe stroke induces long-lasting alterations of high-mobility group box 1. *Stroke*. 2013 Jan;44(1):246-8.
- [57] Garlich CD, Kozina S, Fateh-Moghadam S, et al. Upregulation of CD40-CD40 ligand (CD154) in patients with acute cerebral ischemia. *Stroke*. 2003 Jun;34(6):1412-8.
- [58] Ladenvall C, Jood K, Blomstrand C, et al. Serum C-reactive protein concentration and genotype in relation to ischemic stroke subtype. *Stroke*. 2006 Aug;37(8):2018-23.
- [59] Baldridge MT, King KY, Boles NC, et al. Quiescent haematopoietic stem cells are activated by IFN-gamma in response to chronic infection. *Nature*. 2010 Jun 10;465(7299):793-7.
- [60] Boettcher S, Manz MG. Regulation of Inflammation- and Infection-Driven Hematopoiesis. *Trends Immunol*. 2017 May;38(5):345-357.
- [61] Heo HR, Chen L, An B, et al. Hormonal regulation of hematopoietic stem cells and their niche: a focus on estrogen. *Int J Stem Cells*. 2015 May;8(1):18-23.
- [62] King KY, Goodell MA. Inflammatory modulation of HSCs: viewing the HSC as a foundation for the immune response. *Nat Rev Immunol*. 2011 Sep 9;11(10):685-92.
- [63] Swann JW, Olson OC, Passegue E. Made to order: emergency myelopoiesis and demand-adapted innate immune cell production. *Nat Rev Immunol*. 2024 Aug;24(8):596-613.
- [64] Herault A, Binnewies M, Leong S, et al. Myeloid progenitor cluster formation drives emergency and leukaemic myelopoiesis. *Nature*. 2017 Apr 6;544(7648):53-58.
- [65] Manz MG, Boettcher S. Emergency granulopoiesis. *Nat Rev Immunol*. 2014 May;14(5):302-14.
- [66] Essers MA, Offner S, Blanco-Bose WE, et al. IFNalpha activates dormant haematopoietic stem cells in vivo. *Nature*. 2009 Apr 16;458(7240):904-8.
- [67] Courties G, Herisson F, Sager HB, et al. Ischemic stroke activates hematopoietic bone marrow stem cells. *Circ Res*. 2015 Jan 30;116(3):407-17.
- [68] Kolaczowska E, Kubes P. Neutrophil recruitment and function in health and inflammation. *Nature Reviews Immunology*. 2013 2013/03/01;13(3):159-175.
- [69] Malengier-Devlies B, Metzemaekers M, Wouters C, et al. Neutrophil Homeostasis and Emergency Granulopoiesis: The Example of Systemic Juvenile Idiopathic Arthritis.

- Front Immunol. 2021;12:766620.
- [70] Xie X, Shi Q, Wu P, et al. Single-cell transcriptome profiling reveals neutrophil heterogeneity in homeostasis and infection. *Nat Immunol*. 2020 Sep;21(9):1119-1133.
- [71] Honda T, Uehara T, Matsumoto G, et al. Neutrophil left shift and white blood cell count as markers of bacterial infection. *Clin Chim Acta*. 2016 Jun 1;457:46-53.
- [72] Kirchner T, Moller S, Klinger M, et al. The impact of various reactive oxygen species on the formation of neutrophil extracellular traps. *Mediators Inflamm*. 2012;2012:849136.
- [73] Townsend L, Dyer AH, Naughton A, et al. Severe COVID-19 is characterised by inflammation and immature myeloid cells early in disease progression. *Heliyon*. 2022 Apr;8(4):e09230.
- [74] Mann ER, Menon M, Knight SB, et al. Longitudinal immune profiling reveals key myeloid signatures associated with COVID-19. *Sci Immunol*. 2020 Sep 17;5(51).
- [75] van Grinsven E, Textor J, Hustin LSP, et al. Immature Neutrophils Released in Acute Inflammation Exhibit Efficient Migration despite Incomplete Segmentation of the Nucleus. *J Immunol*. 2019 Jan 1;202(1):207-217.
- [76] Seifert HA, Offner H. The splenic response to stroke: from rodents to stroke subjects. *J Neuroinflammation*. 2018 Jul 3;15(1):195.
- [77] Bao Y, Kim E, Bhosle S, et al. A role for spleen monocytes in post-ischemic brain inflammation and injury. *J Neuroinflammation*. 2010 Dec 15;7:92.
- [78] Park J, Chang JY, Kim JY, et al. Monocyte Transmodulation: The Next Novel Therapeutic Approach in Overcoming Ischemic Stroke? *Front Neurol*. 2020;11:578003.
- [79] Guernonprez P, Helft J. Inflammasome activation: a monocyte lineage privilege. *Nat Immunol*. 2019 Apr;20(4):383-385.
- [80] Schroder K, Tschopp J. The inflammasomes. *Cell*. 2010 Mar 19;140(6):821-32.
- [81] Bryant C, Fitzgerald KA. Molecular mechanisms involved in inflammasome activation. *Trends Cell Biol*. 2009 Sep;19(9):455-64.
- [82] Downs KP, Nguyen H, Dorfleutner A, et al. An overview of the non-canonical inflammasome. *Mol Aspects Med*. 2020 Dec;76:100924.
- [83] Murphy AJ, Tall AR. Disordered haematopoiesis and athero-thrombosis. *Eur Heart J*. 2016 Apr 7;37(14):1113-21.
- [84] Dragoljevic D, Kraakman MJ, Nagareddy PR, et al. Defective cholesterol metabolism in haematopoietic stem cells promotes monocyte-driven atherosclerosis in rheumatoid

- arthritis. *Eur Heart J*. 2018 Jun 14;39(23):2158-2167.
- [85] Chistiakov DA, Grechko AV, Myasoedova VA, et al. The role of monocytosis and neutrophilia in atherosclerosis. *J Cell Mol Med*. 2018 Mar;22(3):1366-1382.
- [86] Netea MG, Joosten LA, Latz E, et al. Trained immunity: A program of innate immune memory in health and disease. *Science*. 2016 Apr 22;352(6284):aaf1098.
- [87] Netea MG, Dominguez-Andres J, Barreiro LB, et al. Defining trained immunity and its role in health and disease. *Nat Rev Immunol*. 2020 Jun;20(6):375-388.
- [88] Verma D, Parasa VR, Raffetseder J, et al. Anti-mycobacterial activity correlates with altered DNA methylation pattern in immune cells from BCG-vaccinated subjects. *Sci Rep*. 2017 Sep 26;7(1):12305.
- [89] Das J, Verma D, Gustafsson M, et al. Identification of DNA methylation patterns predisposing for an efficient response to BCG vaccination in healthy BCG-naive subjects. *Epigenetics*. 2019 Jun;14(6):589-601.
- [90] Arts RJW, Moorlag S, Novakovic B, et al. BCG Vaccination Protects against Experimental Viral Infection in Humans through the Induction of Cytokines Associated with Trained Immunity. *Cell Host Microbe*. 2018 Jan 10;23(1):89-100 e5.
- [91] Walk J, de Bree LCJ, Graumans W, et al. Outcomes of controlled human malaria infection after BCG vaccination. *Nat Commun*. 2019 Feb 20;10(1):874.
- [92] Schrum JE, Crabtree JN, Dobbs KR, et al. Cutting Edge: Plasmodium falciparum Induces Trained Innate Immunity. *J Immunol*. 2018 Feb 15;200(4):1243-1248.
- [93] Christ A, Gunther P, Lauterbach MAR, et al. Western Diet Triggers NLRP3-Dependent Innate Immune Reprogramming. *Cell*. 2018 Jan 11;172(1-2):162-175 e14.
- [94] Braza MS, van Leent MMT, Lameijer M, et al. Inhibiting Inflammation with Myeloid Cell-Specific Nanobiologics Promotes Organ Transplant Acceptance. *Immunity*. 2018 Nov 20;49(5):819-828 e6.
- [95] Ochando J, Fayad ZA, Madsen JC, et al. Trained immunity in organ transplantation. *Am J Transplant*. 2020 Jan;20(1):10-18.
- [96] Bekkering S, Quintin J, Joosten LA, et al. Oxidized low-density lipoprotein induces long-term proinflammatory cytokine production and foam cell formation via epigenetic reprogramming of monocytes. *Arterioscler Thromb Vasc Biol*. 2014 Aug;34(8):1731-8.
- [97] Jenthoe E, Ruiz-Moreno C, Novakovic B, et al. Trained innate immunity, long-lasting epigenetic modulation, and skewed myelopoiesis by heme. *Proc Natl Acad Sci U S A*. 2021 Oct 19;118(42).

- [98] Kaneko N, Kurata M, Yamamoto T, et al. The role of interleukin-1 in general pathology. *Inflamm Regen*. 2019;39:12.
- [99] Leong JW, Chase JM, Romee R, et al. Preactivation with IL-12, IL-15, and IL-18 induces CD25 and a functional high-affinity IL-2 receptor on human cytokine-induced memory-like natural killer cells. *Biol Blood Marrow Transplant*. 2014 Apr;20(4):463-73.
- [100] Mitroulis I, Ruppova K, Wang B, et al. Modulation of Myelopoiesis Progenitors Is an Integral Component of Trained Immunity. *Cell*. 2018 Jan 11;172(1-2):147-161 e12.
- [101] Moorlag S, Khan N, Novakovic B, et al. beta-Glucan Induces Protective Trained Immunity against Mycobacterium tuberculosis Infection: A Key Role for IL-1. *Cell Rep*. 2020 May 19;31(7):107634.
- [102] Ciarlo E, Heinonen T, Theroude C, et al. Trained Immunity Confers Broad-Spectrum Protection Against Bacterial Infections. *J Infect Dis*. 2020 Nov 9;222(11):1869-1881.
- [103] Teufel LU, Arts RJW, Netea MG, et al. IL-1 family cytokines as drivers and inhibitors of trained immunity. *Cytokine*. 2022 Feb;150:155773.
- [104] Cao J, Roth S, Zhang S, et al. DNA-sensing inflammasomes cause recurrent atherosclerotic stroke. *Nature*. 2024 Sep;633(8029):433-441.
- [105] Simats A, Zhang S, Messerer D, et al. Innate immune memory after brain injury drives inflammatory cardiac dysfunction. *Cell*. 2024 Aug 22;187(17):4637-4655 e26.
- [106] Ridker PM, MacFadyen JG, Thuren T, et al. Effect of interleukin-1beta inhibition with canakinumab on incident lung cancer in patients with atherosclerosis: exploratory results from a randomised, double-blind, placebo-controlled trial. *Lancet*. 2017 Oct 21;390(10105):1833-1842.

6. Acknowledgements

First, I want to thank my supervisor, Professor Arthur Liesz, for giving me the opportunity to join ISD and work in his lab. Thank you for being such an outstanding role model and your constant guidance and support throughout my PhD. This experience has reshaped my understanding of scientific research, allowing me to truly engage with and enjoy the process—something that will be invaluable to me wherever life takes me, and whatever I choose to pursue in the future.

Thank you to my co-supervisor, Dr. Alba Simats, for not only teaching me experimental techniques and theoretical knowledge, but also for your understanding, encouragement, and warm support, which helped me settle into the lab, regain direction during times of uncertainty, and stand back up after setbacks. I feel incredibly lucky to have such an inspiring supervisor, colleague, and friend during my time abroad.




I would like to sincerely thank Professor Christian Schulz and Professor Jürgen Bernhagen for being members of my thesis advisory committee. Your invaluable guidance and suggestions have helped me greatly in moving my project forward. I am also grateful to all my collaborators for their support, assistance, and willingness to share. Working with you has always brought me new inspiration, and I have learned so much from our collaborations.

I would like to sincerely thank Dr. Jiayu Cao for helping me integrate into the lab when I first joined and for teaching me so many skills. Thank you, Kelsey—we started this journey at the similar time, and now we are about to graduate together. We've shared so many experiences, and I truly cherish this special bond. Thank you to my dear desk mate, Rashween—your presence has always brought warmth and joy to my days. Thank you, Jiali. I feel so lucky to have met you in my final year. Your companionship and friendship have often made me forget the hardships and feel deeply comforted. My heartfelt thanks to Dr. Stefan Roth, Dr. Gemma Llovera, Dr. Daniel Varga, Dr. Steffanie Heindl and Dr. Alessio Ricci, you have always provided the best support whenever I needed help. Thank you to Christina Bauer for your help and companionship in both experiments and life. Thank you to every member of AG Liesz. Without your generous help and support, I could not have completed this journey.

Finally, I would like to thank my family and friends for their unwavering support and understanding. Thank you to my dad, who has always supported me unconditionally in

everything I do. Thank you to my mom, even from afar, your love has always been with me. Thank you to God for not giving me challenge too great to overcome. And thank you, my dear self.

7. Confirmation of Congruency

	LUDWIG- MAXIMILIANS- UNIVERSITÄT MÜNCHEN	Promotionsbüro Medizinische Fakultät		
Confirmation of congruency between printed and electronic version of the doctoral thesis				

Sijia Zhang

Surname, first name

Street

Zip code, town, country

I hereby declare, that the submitted thesis entitled:

**Systemic Inflammation Post Stroke Leads to Secondary Organ
Dysfunction**.....
.....

is congruent with the printed version both in content and format.

Munich, 09.06.2025

place, date

Sijia Zhang

Signature doctoral candidate